学位論文

# Carbon Nanotubes in Magnetic Fields

# 磁場中のカーボンナノチューブ

平成８年12月博士（理学）申請

東京大学大学院理学系研究科
物理学専攻

安食　博志

学位論文

# Carbon Nanotubes in Magnetic Fields

## 磁場中のカーボンナノチューブ

平成８年12月博士（理学）申請

東京大学大学院理学系研究科
物理学専攻

安食　博志

# Contents

# Chapter 1
# Introduction

Carbon nanotubes (CN's) discovered by Iijima[1] are a new class of quantum wire having the structure of two-dimensional (2D) graphite sheet rolled up in a cylindrical form. The CN's are grown on the negative end of the carbon electrode used in the dc arc-discharge evaporation of carbon. A CN consists of concentric tubes, each of which has carbon-atom hexagons arranged in a helical fashion about the axis. The distance of adjacent tubes is about 0.34 nm, *i.e.*, roughly the same as the distance of adjacent honeycomb lattice planes of graphite. The diameter of each tube is usually between about 20 and 300 Å and the maximum length of a CN exceeds 1$\mu$m in general. The purpose of this thesis is to study the effects of magnetic fields on electronic states, optical absorption, lattice instability, and magnetic properties of carbon nanotubes.

Usually, CN samples contain many other carbon particles (nanoparticles) which sometimes cause undesirable effects in the study of the properties of CN's. It was found recently that CN's can be purified through the removal of nanoparticles by oxidation.[2–4] A single-shell nanotube with diameter ranging from 7 to 16 Å was also produced.[5,6]

In this thesis we shall study effects of magnetic fields on various electronic properties of a single-shell carbon nanotubes. In a magnetic field passing through the tube axis, the band gap changes with the period of the magnetic flux quantum due to the Aharonov-Bohm (AB) effect. The AB effect manifests itself in optical absorption spectra and magnetic properties. In a magnetic field perpendicular to the tube axis, well-defined Landau levels are formed at the Fermi energy originated from that of a 2D graphite. This leads to intriguing properties of CN's including a considerable enhancement of lattice distortion.

It was first shown in tight-binding models[7–17] that a single-shell CN's can be either a metal or semiconductor depending on the diameter and the helical arrangement. A condition for such a characteristic change has been derived based on the band structure of a 2D graphite sheet. Since the distance between adjacent layers is larger than that of nearest-neighbor atoms, interlayer interactions can be neglected. In fact, a calculation based on a model Hamiltonian for double layer nanotubes showed that electronic states are not affected by the interlayer interaction appreciably.[18]

In all calculations mentioned above, effects of the curvature of the cylindrical surface

have been ignored. Although the approximation is valid for CN's having a large diameter, the hybridization of $\sigma$ and $\pi$ states may play some roles in CN's with a small diameter. In fact, *ab initio* pseudopotential calculations showed that the gap is lowered by more than 50 % due to the hybridization for CN's with diameter ranging from 4.7 Å to 7.0 Å.[19]

In this thesis, we shall confine ourselves to CN's with a large diameter for which such curvature effects can be neglected. We shall use a **k**·**p** method throughout this thesis and compare the results with those in a tight-binding model whenever necessary. This thesis is organized as follows: In Chapter 2, a brief review is given of experimental investigations on electronic properties of CN's. Electronic states in magnetic fields are calculated in Chapter 3, optical absorption spectra are studied in Chapter 4, and a lattice instability is discussed in Chapter 5. Magnetic properties of a single CN and realistic ensembles of CN's are studied in Chapter 6. Summary and conclusion are given in Chapter 7.

# Chapter 2
# Carbon Nanotubes

In this Chapter, a brief review is given of experimental investigations on electronic properties of CN's.

## 2.1 Discovery and Synthesis

Carbon nanotubes (CN's) were first produced by Iijima[1] using a dc arc-discharge evaporation of carbon in an argon-filled vessel (100 torr). The apparatus is very similar to that used for the production of $C_{60}$. The macroscopic quantities of CN's were synthesized in a helium atmosphere at $\sim$ 500 Torr, [20] where a large quantity ($\sim$ 75%) of the consumed graphite rod was converted to CN's. There have been two different proposals on the mechanism of the growth of CN's, the open end growth[1,21,22] and closed end growth.[23]

A high-resolution electron micrograph of CN's is shown in Fig. 1, which suggests that CN's consist of several concentric tubes. The distance between adjacent tubes is about 0.34 nm, *i.e.*, roughly the same as the distance of adjacent honeycomb lattice planes of graphite. The diameter of each tube is usually between about 20 and 300 Å and the maximum length of a CN exceeds 1$\mu$m. From electron diffraction patterns it is found that each tube has carbon-atom hexagons arranged in a helical fashion about the axis. Such a characteristic structure is directly confirmed by using a scanning tunneling microscope (STM) as is shown in Fig. 2.[24,25]

CN's are also synthesized by thermal decomposition of Benzene vapor.[26] Benzene vapor was introduced, together with hydrogen, into a ceramic reaction tube in which the substrate consisted of a centrally-placed carbon block. CN's can also be generated by vapor condensation of carbon on an atomically flat graphite surface.[24]

Single-shell nanotubes can be synthesized by arc-discharge evaporation of carbon with catalyst.[5,6] In ref. 5 the cathode has a shallow dimple used to hold a small piece of iron during evaporation. The evaporation chamber is filled with a gas mixture typically consisting of 10 torr methane and 40 torr argon. Figure 3 shows an electron transmission micrograph image of the obtained single-shell CN's and a histogram of the diameters of 50 tubles having a diameter ranging between 0.7 nm and 1.6 nm. A CN as long as 700 nm having a diameter of 0.9nm was found.

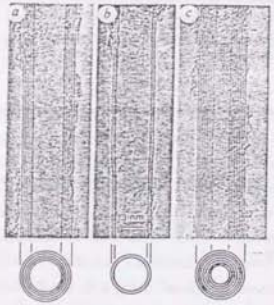


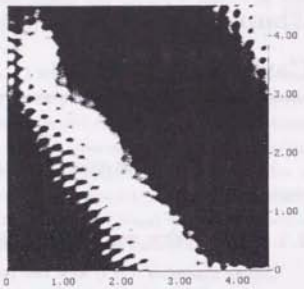


**Fig. 1** (Left) Electron micrographs of CN's.

**Fig. 2** (Right) Atomic resolution STM image of a CN.

In ref. 6 holes of anodes are filled with mixtures of pure powdered metals (Fe, Ni, or Co) and graphite. These filled anodes were vaporized in 100–500 torr of helium. Some examples of obtained single-shell CN's are shown in Fig. 4. The diameter of these CN's turned out to be almost the same and lie in the range $1.2 \pm 0.1$ nm.

In general the tips of CN's are closed and have many variations in shape.[27] One of the typical tips is given in Fig. 5, which shows that small and large cylinders are connected topologically to a cone shaped end without destroying the continuity of the graphite sheets. In this structure pentagons and heptagons play a key role. An apex indicated by arrow A in Fig. 5 must incorporate a single pentagon into a hexagon sheet. A pentagon in a hexagon sheet is a kind of defect in a topological surface, described as a $+60°$ wedge disclination and a surface is curved positively. The opposite situation occurs at the point indicated by arrow B in which a heptagon exists. A heptagon in a hexagon sheet gives defect described as a $-60°$ wedge disclination and a surface is curved negatively. The presence of both a $+60°$ disclination and $-60°$ disclination on a closed hexagon surface restores the original shape.

Figure 6 shows nearly regular cone-like terminations, which are quite common in thicker tubes. Five pentagons are required for the apex to be closed. There is no preferred distribution of such five pentagons at the tips. The arrangement of pentagons shows signatures of the helicity in the hexagonal network of CN's.[28]

## 2.2 Purification



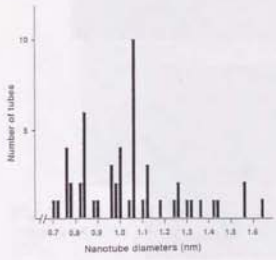


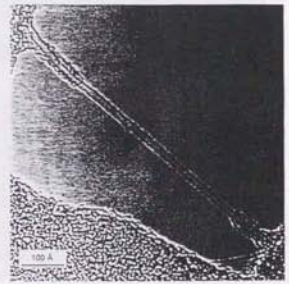


**Fig. 3** (Left) An electron micrograph showing individual single-shell CN's (upper panel) and a histogram showing the number of single-shell CN's of different diameters (lower panel).

**Fig. 4** (Right) A transmission electron micrograph image of a single-shell CN.

The oxidation reactivity rates of the caps are larger than the cylinder surfaces, because of the strong local curvature and imperfect geometry caused by the presence of five pentagons. Thus, CN's having open tips are produced through oxidation.[29,30] The geometry of nanoparticles, which are often yielded with CN's, much resemble that of the tube caps, although they are comparatively larger.[28] Therefore, nanoparticles are similarly consumed by oxidation although at a slower rate than the highly curved tips of CN's and CN samples can be purified if the oxidation is allowed to proceed for long durations.[2] Figure 7 shows the dramatic improvement in the CN's-to-nanoparticle ratio after the oxidation. To remove all the nanoparticles from the samples, one has to oxidize more than 99 % of the material. Similar purification methods through oxidation are reported also by other groups.[3,4]

## 2.3 Electronic Properties

It was first shown in tight-binding models[7–17] that a single-shell CN's can be either a metal or a semiconductor depending on the diameter and the helical arrangement. A condition for such a characteristic change has been derived based on the band structure of

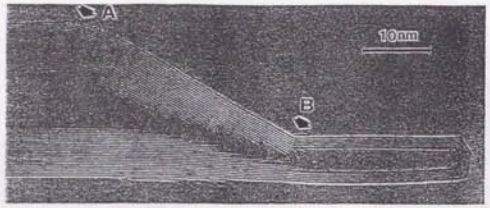


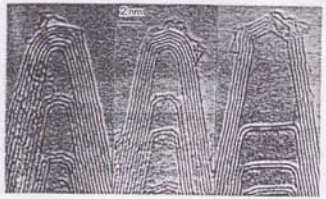


**Fig. 5** (Up) Electron micrograph showing recurrent terminations of CN's.

**Fig. 6** (Down) Terminations with identical conical caps at the tips of CN's.

a two-dimensional (2D) graphite sheet. A part of metallic CN's is classified into narrow-gap semiconductor by including the effect of finite curvature.[7] Some typical examples of calculated energy bands are shown in Figs. 8 and 9.[7] Figure 8 (b) corresponds to a CN classified as a narrow-gap semiconductor, Fig. 8 (c) as a semiconductor, and Fig. 9 (b) a metal. It has been noted that the gap of semiconducting CN's is roughly inversely proportional to the diameter.[17,18]

| Tube | Tight binding Ref. [2] | Present calculations TB | LDA |
|---|---|---|---|
| (6,0) | ~0.2 | 0.05 | Metal (−0.83) |
| (7,0) | ~1 | 1.04 | 0.09 |
| (8,0) | 1.22 | 1.19 | 0.62 |
| (9,0) | 0.04 | 0.07 | 0.17 |

**Table 1** Band gap (in eV) of selected CN's. For the metallic case, the overlap of the bands is given as a negative gap.

Electronic properties calculated by a tight-binding model are significantly altered by detailed plane wave *ab initio* pseudopotential calculations for CN's with small diameter.[19]



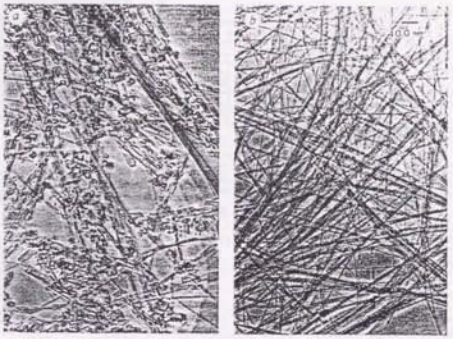

**Fig. 7** Low-magnification transmission electron microscope images of (a) typical samples of CN's produced by the carbon-arc method, and (b) purified sample of CN's.

Some comparisons with the tight-binding calculation in ref. 7 are shown in Table 1 in which CN's denoted by $(n,0)$ have the structure shown in Fig. 8 (a). In the pseudopotential calculation a CN with (6,0) becomes a metal in contrast to the narrow-gap semiconductor predicted in a tight-binding model. In addition, CN's with (7,0) and (8,0) become semiconductors, consistent with the tight-binding calculation, but give a much smaller gap. This discrepancy comes from a strong $\sigma^*$-$\pi^*$ hybridization due to the large curvature of cylinder surface of narrow CN's.

The above studies are all on single-shell CN's. A calculation based on a model tight-binding Hamiltonian for a double-layer nanotube shows that electronic states are not affected by the interlayer interaction appreciably.[18] This is because of the fact that the distance between adjacent interlayers (3.4 Å) is larger than that between nearest-neighbor atoms (1.42 Å). The electronic states of disclinations and caps have been studied also.[31,32]

Some experiments support the theoretical prediction on electronic states. Current-voltage characteristics were measured by a scanning tunneling spectroscopy (STS).[33–35] Figure 10 (b) shows the result at the points shown in Fig. 10 (a).[34] The top inset shows the conductance ($dI/dV$) curve and the bottom inset shows the $I$-$V$ curve taken on the gold substrate for comparison. The trace (1), taken on a tube with 8.7 nm diameter, has an ohmic behavior, providing evidence for the metallic CN's. Two tubles (trace (2) for a CN with 4.0 nm diameter and trace (3) for a CN with 1.7 nm diameter) show plateaus in

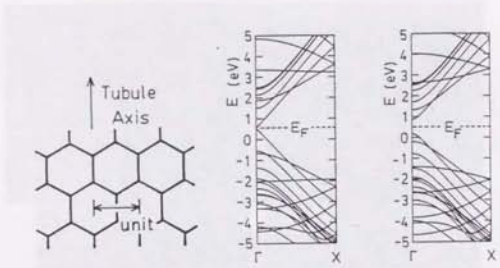


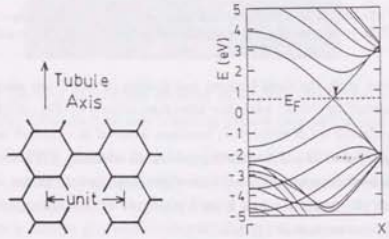


**Fig. 8** (Up) (a) The geometric configuration for CN's with $(n, 0)$. (b) The band structure of CN with $(12, 0)$ (narrow-gap semiconductor). (c) The band structure of CN with $(13, 0)$ (semiconductor).

**Fig. 9** (Down) (a) The geometric configuration for CN' with $(2n, n)$. (b) The band structure of CN with $(12, 6)$ (metal).

the $I$-$V$ characteristics at zero current, showing that these CN's are semiconducting.The conductance (top insert) corresponds to the density of states and exhibits $1/\sqrt{E_0 - E}$ type singularities in the 1D density of states at peaks. The energy gap of the semiconducting CN's was estimated around $V = 0$ V and found to vary in inverse proportion to the diameter as is predicted in tight-binding calculations.[17,18]

Another experiment carried out to study the electronic properties was the electron spin resonance (ESR) for purified CN's.[36,37] In ref. 36 conduction electron spin resonance



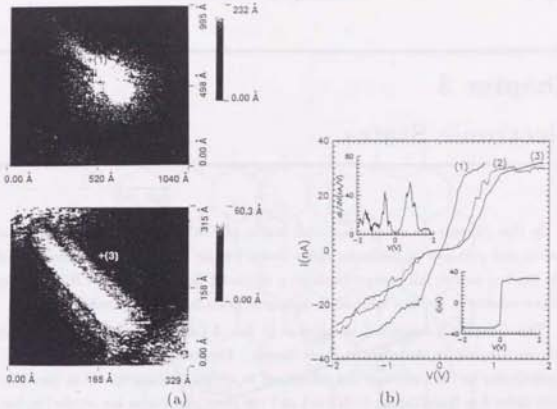


**Fig. 10** (a) STM micrograph of CN's. (b) Current-voltage characteristics taken at (1), (2), and (3) in Fig. 10 (a). The top inset shows the conductance versus voltage. The bottom inset shows a characteristic $I$-$V$ taken on gold substrate.

(CESR) were not observed and therefore it was concluded that CN's are semiconducting. However in ref. 37 CESR was clearly observed. Since the intensity of CESR showed no temperature dependence, leading to the conclusion that there exist metallic and/or narrow-gap semiconducting CN's.

The direct electrical resistance measurements were performed first on a single CN's bundle.[38,39] At higher temperatures a typical semimetallic behavior was observed. A magnetic field applied perpendicular to the sample axis reduces the resistivity. In ref. 39 the resistance in the low temperature region exhibits a logarithmic dependence on temperature consistent with a 2D weak localization. A theoretical calculation for CN's also shows the characteristic temperature dependence.[40] Recently the electrical resistance was measured for an individual CN.[41] A magnetoconductance exhibits universal conductance fluctuations similar to those observed in quasi-1D mesoscopic systems.

# Chapter 3

# Electronic States

In this chapter we study electronic states of CN's near the Fermi energy in the absence and presence of magnetic fields based on the effective-mass theory.[42] Using a tight-binding model, full energy bands in a magnetic field of metallic CN's are obtained and the validity of the **k**·**p** method in magnetic fields is demonstrated.[43]

This Chapter is organized as follows: In Sec. 3.1 the electronic states in magnetic fields are studied in the effective-mass theory. The energy bands in a magnetic field perpendicular to the tube axis are calculated in a tight-binding model in Sec. 3.2. The higher order **k**·**p** Hamiltonian is derived and the electronic states are studied in Sec. 3.3. A summary is given in Sec. 3.4.

## 3.1 Effective-Mass Approximation

### 3.1.1 Hamiltonian

Although CN's take a multi-shell structure in general, we consider a CN consisting of a single tube. Since the distance between adjacent layers is much larger than the bond length between nearest-neighbor sites within a layer, characteristic features of CN's are expected to be obtained by those of a single nanotube. In fact, it was demonstrated by a model calculation that the effect of the interlayer interaction on electronic states is small.[10] Further, we assume an infinitely long tube for simplicity.

Every structure of single tube CN's can be constructed from a monatomic layer of graphite as shown in Fig. 11 (a). Each hexagon is denoted by the chiral vector

$$\mathbf{L} = n_a\mathbf{a} + n_b\mathbf{b} \equiv (n_a, n_b), \tag{3.1}$$

with basis vectors **a** and **b**, defined by

$$\mathbf{a} = a\mathbf{e}'_x \quad \text{and} \quad \mathbf{b} = a\Big(-\frac{1}{2}\mathbf{e}'_x + \frac{\sqrt{3}}{2}\mathbf{e}'_y\Big), \tag{3.2}$$

with $|\mathbf{a}|=|\mathbf{b}|=a=2.46$ Å, where the unit vectors $(\mathbf{e}'_x, \mathbf{e}'_y)$ are fixed onto a graphite sheet as shown in Fig. 11 (a). We shall construct a nanotube in such a way that the hexagon at **L** is rolled onto the origin. For convenience, we introduce another unit basis vectors





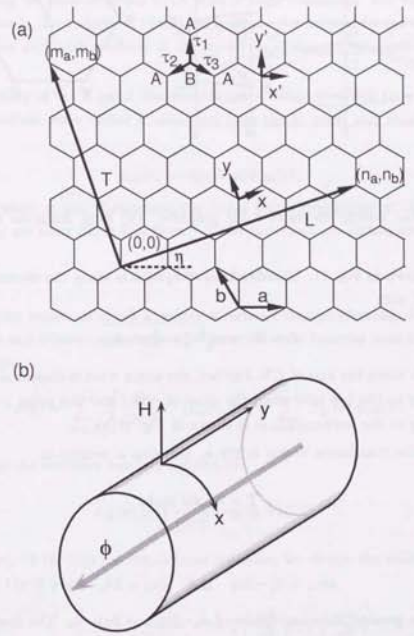


**Fig. 11** (a) A single layer of graphite. The structure of a nanotube is specified by the chiral vector $\mathbf{L}=n_a\mathbf{a}+n_b\mathbf{b}$ with **a** and **b** being primitive translation vector. The primitive translation vector along the axis of CN's is **T**. The unit vectors $\mathbf{e}_x$ and $\mathbf{e}_y$ denoted by $x$ and $y$ are along the circumference and the axis of a CN, respectively. Another unit vectors $\mathbf{e}'_x$ and $\mathbf{e}'_y$ denoted by $x'$ and $y'$ are fixed on the graphite sheet. The angle $\eta$ between $\mathbf{e}'_x$ and **L** is a chiral angle. The vectors $\vec{\tau}_1$, $\vec{\tau}_2$, and $\vec{\tau}_3$ connect nearest-neighbor A and B sites. (b) A carbon nanotube in the presence of magnetic field $H$ perpendicular to the tube axis and magnetic flux $\phi$ passing through its cross section.

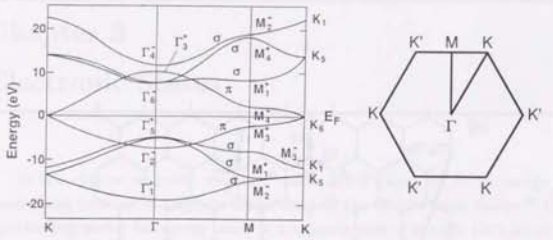


(a) (b)

**Fig. 12** (a) Energy bands of a 2D graphite. (b) First Brillouin zone of a 2D graphite.

$(\mathbf{e}_x, \mathbf{e}_y)$ as shown in Fig. 11. The direction of $\mathbf{e}_x$ or $x$ is along the circumference of CN, *i.e.*, $\mathbf{e}_x = \mathbf{L}/L$ with

$$L = |\mathbf{L}| = a\sqrt{n_a^2 + n_b^2 - n_a n_b}. \tag{3.3}$$

and $\mathbf{e}_y$ or $y$ is along the axis of CN. Further, the origin $x = 0$ is chosen always at a point corresponding to the top side when the sheet is rolled and the point $x = L/2$ at point corresponding to the bottom side as is shown in Fig. 11(b).

A primitive translation vector in the $\mathbf{e}_y$ direction is written as

$$\mathbf{T} = m_a \mathbf{a} + m_b \mathbf{b}, \tag{3.4}$$

with

$$p m_a = n_a - 2n_b \quad \text{and} \quad p m_b = 2n_a - n_b, \tag{3.5}$$

where $p$ is the greatest common divisor of $n_a - 2n_b$ and $2n_a - n_b$. The first Brillouin zone of the nanotube is given by the region $-\pi/T \le k_y < \pi/T$ with

$$T = a\sqrt{m_a^2 + m_b^2 - m_a m_b}. \tag{3.6}$$

The unit cell is formed by the rectangular region determined by $\mathbf{L}$ and $\mathbf{T}$.

Figures 12 (a)[44] and (b) show the electronic states and the first Brillouin zone of 2D graphite sheet, respectively. A graphite sheet is a zero-gap semiconductor in the



sense that the conduction and valence bands consisting of $\pi$ states touch at the K and K' points, whose wave vectors are given by

$$\mathbf{K} = \frac{2\pi}{a}\left(\frac{1}{3}\mathbf{e}'_x + \frac{1}{\sqrt{3}}\mathbf{e}'_y\right) \quad \text{and} \quad \mathbf{K}' = \frac{2\pi}{a}\frac{2}{3}\mathbf{e}'_x. \tag{3.7}$$

In the following we shall consider CN's with a large diameter. For such nanotubes, electronic states in the vicinity of the Fermi level are determined by the states near the K and K' points and further effects of the curvature of the graphite sheet can safely be neglected.

In the vicinity of the K point electronic states are described well by a **k**·**p** Hamiltonian.[45] We introduce wave vector $\mathbf{k}$ measured from the K point and consider the set of functions

$$\phi_{i\mathbf{k}}(\mathbf{r}) = \exp(\mathrm{i}\mathbf{k}\cdot\mathbf{r})\Psi_{i\mathbf{K}}(\mathbf{r}), \tag{3.8}$$

with $i = \mathrm{A}, \mathrm{B}$ where A and B represent the two $\pi$ bands degenerate at the K point and $\Psi_{\mathrm{AK}}$ and $\Psi_{\mathrm{BK}}$ are their Bloch functions.* These functions are orthonormal:[46]

$$(\phi_{i\mathbf{k}}, \phi_{i'\mathbf{k}'}) = \delta_{ii'}\delta_{\mathbf{k}\mathbf{k}'}. \tag{3.9}$$

We consider the region of small $\mathbf{k}$ where interband matrix elements between the $\pi$-electron states and others can be ignored. Then, the wave function near the K point can be expanded as

$$\psi(\mathbf{r}) = \sum_{i=\mathrm{A,B}} \int \frac{\mathrm{d}\mathbf{k}}{(2\pi)^2} C^i(\mathbf{k})\,\phi_{i\mathbf{k}}(\mathbf{r}) = \sum_{i=\mathrm{A,B}} F^i_{\mathbf{K}}(\mathbf{r})\,\Psi_{i\mathbf{K}}(\mathbf{r}), \tag{3.10}$$

where $F^i_{\mathbf{K}}(\mathbf{r})$ is the envelope function defined by

$$F^i_{\mathbf{K}}(\mathbf{r}) = \int \frac{\mathrm{d}\mathbf{k}}{(2\pi)^2} \exp(\mathrm{i}\mathbf{k}\cdot\mathbf{r})\, C^i(\mathbf{k}). \tag{3.11}$$

Substituting eq. (3.10) into the Schrödinger equation, we obtain the following $2 \times 2$ **k**·**p** equation near the K point:

$$\begin{pmatrix} 0 & \gamma(\hat{k}_x - \mathrm{i}\hat{k}_y) \\ \gamma(\hat{k}_x + \mathrm{i}\hat{k}_y) & 0 \end{pmatrix} \begin{pmatrix} F^{\mathrm{A}}_{\mathbf{K}} \\ F^{\mathrm{B}}_{\mathbf{K}} \end{pmatrix} = \varepsilon \begin{pmatrix} F^{\mathrm{A}}_{\mathbf{K}} \\ F^{\mathrm{B}}_{\mathbf{K}} \end{pmatrix}, \tag{3.12}$$

where $\gamma$ is a band parameter and $\hat{\mathbf{k}}$ is a wave vector operator defined by

$$\hat{\mathbf{k}} = -\mathrm{i}\vec{\nabla} + \frac{e}{c\hbar}\mathbf{A}. \tag{3.13}$$

* The **k**·**p** Hamiltonian is also obtained from a tight-binding model and the envelope functions correspond to orbitals at A and B site as will be shown later. Thus, we choose the notation (A and B) for two $\pi$ bands.

Effects of a magnetic field are included by the vector potential $\mathbf{A}$ appearing in the above operator. The energy origin has been chosen at the Fermi level of a graphite sheet.

Similarly, the $\mathbf{k}\cdot\mathbf{p}$ Hamiltonian near the K' point is given by

$$\begin{pmatrix} 0 & \gamma(\hat{k}_x+\mathrm{i}\hat{k}_y) \\ \gamma(\hat{k}_x-\mathrm{i}\hat{k}_y) & 0 \end{pmatrix} \begin{pmatrix} F^{\mathrm{A}}_{\mathbf{K}'} \\ F^{\mathrm{B}}_{\mathbf{K}'} \end{pmatrix} = \varepsilon \begin{pmatrix} F^{\mathrm{A}}_{\mathbf{K}'} \\ F^{\mathrm{B}}_{\mathbf{K}'} \end{pmatrix}. \tag{3.14}$$

It is noted that eqs. (3.12) and (3.14) are rewritten in terms of Pauli matrix $\vec{\sigma}=(\sigma_x,\sigma_y)$ as

$$\begin{aligned} \gamma(\sigma_x\hat{k}_x+\sigma_y\hat{k}_y)\mathbf{F}_{\mathbf{K}}(\mathbf{r}) &= \varepsilon\mathbf{F}_{\mathbf{K}}, \\ \gamma(\sigma_x\hat{k}_x-\sigma_y\hat{k}_y)\mathbf{F}_{\mathbf{K}'}(\mathbf{r}) &= \varepsilon\mathbf{F}_{\mathbf{K}'}. \end{aligned} \tag{3.15}$$

These equations have the same form as Weyl's equation for neutrinos.

The electronic states of CN's are obtained from eq. (3.15) by imposing the generalized boundary condition in the circumference or $x$ direction such as

$$\psi(\mathbf{r}+\mathbf{L}) = \psi(\mathbf{r})\exp(2\pi\mathrm{i}\varphi), \tag{3.16}$$

with $\varphi=\phi/\phi_0$, where $\phi$ is the total magnetic flux passing through the cross section of CN and $\phi_0=ch/e$ is the magnetic flux quantum. A Bloch function at the K point changes its phase according as

$$\Psi_{i\mathbf{K}}(\mathbf{r}+\mathbf{L}) = \Psi_{i\mathbf{K}}(\mathbf{r})\exp(\mathrm{i}\mathbf{K}\cdot\mathbf{L}) = \Psi_{i\mathbf{K}}(\mathbf{r})\exp\left(\mathrm{i}\frac{2\pi\nu}{3}\right), \tag{3.17}$$

where

$$n_a+n_b = 3N+\nu, \tag{3.18}$$

with integer $N$ and $\nu$ ($=0,\pm1$). Since the phase change should be canceled by that of the envelope functions, the boundary conditions for the envelope functions are given by

$$\mathbf{F}_{\mathbf{K}}(\mathbf{r}+\mathbf{L}) = \mathbf{F}_{\mathbf{K}}(\mathbf{r})\exp\left[2\pi\mathrm{i}\left(\varphi-\frac{\nu}{3}\right)\right]. \tag{3.19}$$

The corresponding conditions for the K' point are given by

$$\mathbf{F}_{\mathbf{K}'}(\mathbf{r}+\mathbf{L}) = \mathbf{F}_{\mathbf{K}'}(\mathbf{r})\exp\left[2\pi\mathrm{i}\left(\varphi+\frac{\nu}{3}\right)\right]. \tag{3.20}$$

Note that this can be obtained from eq. (3.19) though the replacement $\nu$ by $-\nu$.

For translation $\mathbf{r}\to\mathbf{r}+\mathbf{T}$, the Bloch function acquires the phase:

$$\exp(\mathrm{i}\mathbf{K}\cdot\mathbf{T}) = \exp\left(\mathrm{i}\frac{2\pi\mu}{3}\right), \tag{3.21}$$



where

$$m_a+m_b = 3M+\mu, \tag{3.22}$$

with integer $M$ and $\mu$ ($=0,\pm1$). Thus, the K point in the graphite sheet is mapped onto $k_0=+2\pi\mu/3T$ of the one-dimensional Brillouin zone. Similarly, we can show that the K' point is mapped to $k_0'=-2\pi\mu/3T$.

### 3.1.2 Band gap

In the absence of a magnetic field perpendicular to the axis, the envelope functions in the $x$ direction are plane waves $\propto\exp(\mathrm{i}\kappa x)$. Thus, discrete wave vectors in the circumference direction are obtained as

$$\kappa_{\nu\varphi}(n) = \frac{2\pi}{L}\left(n+\varphi-\frac{\nu}{3}\right), \tag{3.23}$$

where $n$ is an integer. Noting that the wave function in the axial or $y$ direction is proportional to $\exp(\mathrm{i}ky)$, we get energy levels around K and K' points

$$\varepsilon^{(\pm)}_{\nu\varphi}(n) = \pm\gamma\sqrt{\kappa_{\nu\varphi}(n)^2+k^2}, \tag{3.24}$$

where the upper (+) and lower (−) signs represent the conduction and valence bands, respectively. The corresponding wave functions are written as

$$\begin{aligned} \mathbf{F}_{\mathbf{K}}(\mathbf{r}) &= \frac{1}{\sqrt{2}}\begin{pmatrix} b_{\nu\varphi}(n,k) \\ \mp1 \end{pmatrix}\exp\left[\mathrm{i}\kappa_{\nu\varphi}(n)x+\mathrm{i}ky\right], \\ \mathbf{F}_{\mathbf{K}'}(\mathbf{r}) &= \frac{1}{\sqrt{2}}\begin{pmatrix} b_{-\nu\varphi}(n,k)^* \\ \mp1 \end{pmatrix}\exp\left[\mathrm{i}\kappa_{-\nu\varphi}(n)x+\mathrm{i}ky\right], \end{aligned} \tag{3.25}$$

with

$$b_{\nu\varphi}(n,k) = \frac{\kappa_{\nu\varphi}(n)-\mathrm{i}k}{\sqrt{\kappa_{\nu\varphi}(n)^2+k^2}}, \tag{3.26}$$

where upper and lower signs in eq. (3.25) correspond to valence and conduction bands, respectively.

Because of the one-dimensional energy band, the density of states remains nonzero even for $\varepsilon=0$ and the system is metallic for $\nu=0$. This is quite in contrast to the graphite sheet for which the density of states vanishes at $\varepsilon=0$ even if the band gap vanishes. Each energy band of metallic CN's is two-fold degenerate except those for $n=0$.

When $\nu=\pm1$, on the other hand, there exists no integer leading to $\kappa=0$ and the spectra have a minimum gap given by $E_g=4\pi\gamma/3L$ inversely proportional to the tube diameter. The band parameter $\gamma$ is related to the transfer integral $\gamma_0$ for nearest-neighbor atoms in a tight-binding model through $\gamma=\sqrt{3}a\gamma_0/2$. If we use $\gamma_0\approx-3.03$ eV ($\gamma=6.46$eVÅ),[9] we have $E_g=0.45\sim0.034$ eV for circumference 60∼800 Å (corresponding

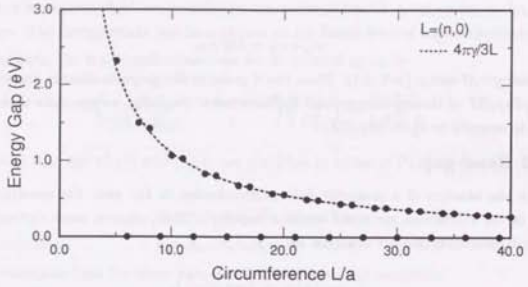


**Fig. 13** Band gap of CN's with $\mathbf{L}=(n,0)$ as a function of the circumference. The dots represent tight-binding results and the dotted line represents $4\pi\gamma/3L$ for semiconducting CN's given in the $\mathbf{k}\cdot\mathbf{p}$ theory.

to diameter 19.1~255 Å). Figure 13 shows the band gap of CN's with $\mathbf{L}=(n,0)$ as a function of the circumference calculated in a tight-binding model and the $\mathbf{k}\cdot\mathbf{p}$ theory. Gaps obtained in the $\mathbf{k}\cdot\mathbf{p}$ approximation is in good agreement with those obtained in the tight-binding model. For a CN with $(n_a,n_b)=(13,0)$ corresponding to $L=13a=31.98$ Å, we have $E_g=0.85$ eV, which is slightly larger than $E_g=0.70$ eV obtained by Hamada *et al.*[7] in a tight-binding model using different parameters.

In the presence of a magnetic flux $\phi$ through the cross section of CN's, the band gap oscillates ranging from 0 to $2\pi\gamma/L$ in the period of $\phi_0$ due to the Aharonov-Bohm effect. Figure 14 exhibits the energy gap as a function of magnetic flux. If we use $\gamma=6.46$ eV·Å, $2\pi\gamma/L$ varies as $1.85\sim0.044$ eV for diameter $7\sim300$ Å. Since energy levels around K' point are obtained by changing the sign of $\nu$, the oscillation at the K' point is different.

There are three cases: (i) $\nu=\mu=0$, (ii) $\nu=0$ and $\mu=\pm1$, and (iii) $\nu=\pm1$ and $\mu=0$. The case that $\nu=\pm1$ and $\mu=\pm1$ is forbidden as shown below. From Eqs. (3.5), (3.18), and (3.22) we have

$$pm_a=3(N-n_b)+\nu \quad \text{and} \quad \frac{3(n_a-n_b)}{p}=3M+\mu. \tag{3.27}$$

The first equation shows that $p$ cannot be a multiple of 3 for $\nu\neq0$, which means that $3M+\mu$ is a multiple of 3 according to the second equation and consequently $\mu=0$. On the other hand, the second equation shows that $p$ must be a multiple of 3 for $\mu\neq0$, which leads to $\nu=0$ according to the first equation.

By combining the results obtained above and those described in the last paragraph of the previous section, we can conclude that the conduction-band bottom and the valence band top exist at the $\Gamma$ point of the one-dimensional Brillouin zone whenever the



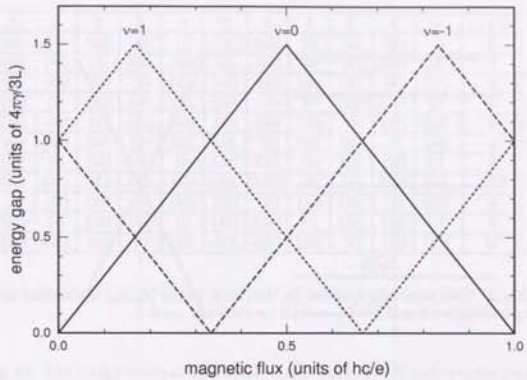


**Fig. 14** Energy gap versus magnetic flux passing through the cross section for $\nu=0$ and $\pm1$.

| Type | $\nu$ | $\mu$ | $E_g$ | $k_0$ |
|---|---|---|---|---|
| (i) | 0 | 0 | 0 | 0 |
| (ii) | 0 | $\pm1$ | 0 | $\pm2\pi/3T$ |
| (iii) | $\pm1$ | 0 | $4\pi\gamma/3L$ | 0 |

**Table 2** Nanotubes can be characterized into three types by two integers $\nu$ and $\mu$ determined by the chiral vector. $E_g$ is the band gap (0 for metallic CN's) and $k_0$ represents the wave vector corresponding to the bottom of the conduction band in the one-dimensional Brillouin zone.

nanotube has a band gap and is a semiconductor. For a metallic nanotube, on the other hand, the conduction and valence band touch either at the $\Gamma$ point or at $\pm2\pi/3T$. Table **2** summarizes three different types of CN's and Table **3** gives a table showing the type for some values of $n_a$ and $n_b$.

In general, CN's have some helical structure as is shown in Fig. 11 (a) except for two cases having chiral vectors $\mathbf{L}=m\mathbf{a}$ and $\mathbf{L}=m(2\mathbf{a}+\mathbf{b})$. The former is called zigzag nanotubes and the latter is called armchair nanotube. Their structures are illustrated in Fig. 15.

A zigzag CN has the circumference length $L=ma$ and the first Brillouin zone is $-\pi/\sqrt{3}a\leq k<\pi/\sqrt{3}a$. It is metallic for $m$ being multiple of 3 and semiconducting for all other $m$'s as is seen in eq. (3.18). From eq. (3.5) we get $(m_a,m_b)=(1,2)$ and it leads

| $n_b \backslash n_a$ | 0 | 1 | 2 | 3 | 4 | 5 | 6 | 7 | 8 | 9 | 10 |
|---|---|---|---|---|---|---|---|---|---|---|---|
| 0 | | (iii) | (iii) | (i) | (iii) | (iii) | (i) | (iii) | (iii) | (i) | (iii) |
| 1 | (iii) | (iii) | (ii) | (iii) | (iii) | (ii) | (iii) | (iii) | (ii) | (iii) | (iii) |
| 2 | (iii) | (ii) | (iii) | (iii) | (ii) | (iii) | (iii) | (ii) | (iii) | (iii) | (ii) |
| 3 | (i) | (iii) | (iii) | (i) | (iii) | (iii) | (ii) | (iii) | (iii) | (i) | (iii) |
| 4 | (iii) | (iii) | (ii) | (iii) | (iii) | (ii) | (iii) | (iii) | (ii) | (iii) | (iii) |
| 5 | (iii) | (ii) | (iii) | (iii) | (ii) | (iii) | (iii) | (ii) | (iii) | (iii) | (ii) |
| 6 | (i) | (iii) | (iii) | (ii) | (iii) | (iii) | (i) | (iii) | (iii) | (i) | (iii) |
| 7 | (iii) | (iii) | (ii) | (iii) | (iii) | (ii) | (iii) | (iii) | (ii) | (iii) | (iii) |
| 8 | (iii) | (ii) | (iii) | (iii) | (ii) | (iii) | (iii) | (ii) | (iii) | (iii) | (ii) |
| 9 | (i) | (iii) | (iii) | (i) | (iii) | (iii) | (i) | (iii) | (iii) | (i) | (iii) |
| 10 | (iii) | (iii) | (ii) | (iii) | (iii) | (ii) | (iii) | (iii) | (ii) | (iii) | (iii) |

**Table 3** Each nanotube specified by the chiral vector $(n_a, n_b)$ is classified into (i) $\nu=\mu=0$, (ii) $\nu=0$ and $\mu=\pm1$, and (iii) $\nu=\pm1$ and $\mu=0$.

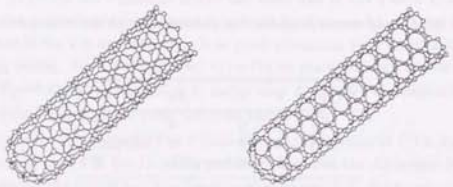

(a) (b)

**Fig. 15** The structure of (a) zigzag and (b) armchair nanotubes.

$\mu=0$ from eq. (3.22) for any integer $m$. Thus, the band structure near the Fermi energy corresponds to the case (i) for $m$ being multiple of 3 and the case (iii) for all other $m$.

For an armchair CN the circumference length is $L=\sqrt{3}ma$ and the first Brillouin zone is $-\pi/a \le k < \pi/a$. Armchair CN's are all metallic and $\mu=1$ because $(m_a, m_b) = (0,1)$. Consequently the band structure always corresponds to that of the case (ii).

### 3.1.3 States in magnetic fields

Before discussing electronic states of CN's in a magnetic field perpendicular to the axis, the states of 2D graphite sheet will be reviewed. We introduce the ladder operators $\hat{L}_\pm = (l/\sqrt{2})(\hat{k}_x \pm i\hat{k}_y)$ with $l=\sqrt{ch/eH}$ being magnetic length. Then, the $\mathbf{k}\cdot\mathbf{p}$ Hamiltonian



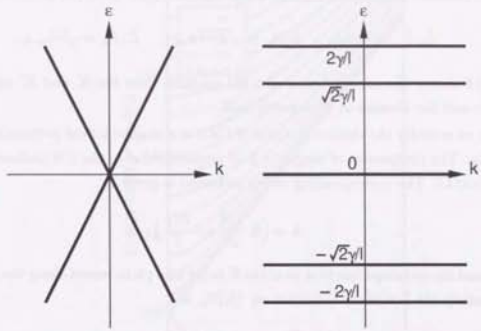


**Fig. 16** The energy bands of a 2D graphite near the K and K' points in the presence (a) and the absence (b) of a magnetic field.

is rewritten as

$$\mathcal{H} = \begin{pmatrix} 0 & \sqrt{2}\gamma \hat{L}_\mp / l \\ \sqrt{2}\gamma \hat{L}_\pm / l & 0 \end{pmatrix}, \tag{3.28}$$

where upper and lower signs correspond to K and K' points, respectively. This Hamiltonian leads to the presence of a Landau level with a vanishing energy eigenvalue. For the Landau gauge $(0, Hx)$, we have

$$\begin{aligned} &\varepsilon_{2D}=0, \quad \mathbf{F}_\mathbf{K} = \frac{1}{\sqrt{L_y}} \exp(ik_y y) \begin{pmatrix} 0 \\ h_0 \end{pmatrix} \quad \text{K point}, \\ &\varepsilon_{2D}=0, \quad \mathbf{F}_{\mathbf{K}'} = \frac{1}{\sqrt{L_y}} \exp(ik_y y) \begin{pmatrix} h_0 \\ 0 \end{pmatrix} \quad \text{K' point}, \end{aligned} \tag{3.29}$$

with $L_y$ and $k_y$ being the system size and the wave vector, respectively, in the $y$ direction. Other Landau levels are given by

$$\begin{aligned} &\varepsilon_{2D} = \pm\sqrt{2}\gamma\frac{\sqrt{n+1}}{l}, \quad \mathbf{F}_\mathbf{K} = \frac{1}{\sqrt{2L_y}} \exp(ik_y y) \begin{pmatrix} \pm h_n \\ h_{n+1} \end{pmatrix}, \quad n=0,1,\cdots \quad \text{K point}, \\ &\varepsilon_{2D} = \pm\sqrt{2}\gamma\frac{\sqrt{n+1}}{l}, \quad \mathbf{F}_{\mathbf{K}'} = \frac{1}{\sqrt{2L_y}} \exp(ik_y y) \begin{pmatrix} \pm h_{n+1} \\ h_n \end{pmatrix}, \quad n=0,1\cdots \quad \text{K' point}, \end{aligned} \tag{3.30}$$

where upper and lower signs correspond to conduction and valence bands, respectively, and $h_n$ is the harmonic oscillator eigenfunctions written as

$$h_n = \frac{i^n}{\sqrt{2^n n! \sqrt{\pi} l}} \exp\left[-\frac{1}{2}\left(\frac{x+l^2k_y}{l}\right)^2\right] H_n\left(\frac{x+l^2k_y}{l}\right), \tag{3.31}$$

with the Hermite polynomial $H_n(x)$. These eigenfunctions have the properties:

$$\hat{L}_+\hat{L}_-h_n = nh_n, \quad \hat{L}_+h_n = \sqrt{n+1}h_{n+1}, \quad \hat{L}_-h_n = \sqrt{n}h_{n-1}. \tag{3.32}$$

Figure 16 shows the energy levels of a 2D graphite near the K and K' points in the presence and the absence of a magnetic field.

Let us consider the electronic states of CN's in a magnetic field perpendicular to the tube axis. The component of magnetic field perpendicular to the CN surface is given by $H\cos(2\pi x/L)$. The corresponding vector potential is given by

$$\mathbf{A} = \left(0, \frac{LH}{2\pi}\sin\frac{2\pi x}{L}\right). \tag{3.33}$$

We expand the envelope function near the K point into plane waves along the $x$ direction, which satisfy the boundary condition eq. (3.19), as

$$F_{\mathbf{K}}^{\mathrm{A,B}}(\mathbf{r}) = \frac{1}{\sqrt{L}}\sum_{n=-\infty}^{\infty} G_{\mathbf{K}n}^{\mathrm{A,B}} \exp\left[\frac{2\pi ix}{L}\left(n+\varphi-\frac{\nu}{3}\right)+iky\right], \tag{3.34}$$

with $G_{\mathbf{K}n}^{\mathrm{A,B}}$ being expansion coefficients. The equation for $G_{\mathbf{K}n}^{\mathrm{A,B}}$ is written as

$$\begin{aligned}
&\frac{2\pi\gamma}{L}\left\{\left(\hat{\kappa}_{\nu\varphi}(n)+i\frac{Lk}{2\pi}\right)G_{\mathbf{K}n}^{\mathrm{A}} - \frac{1}{2}\left(\frac{L}{2\pi l}\right)^2\left(G_{\mathbf{K}n+1}^{\mathrm{A}} - G_{\mathbf{K}n-1}^{\mathrm{A}}\right)\right\} = \varepsilon G_{\mathbf{K}n}^{\mathrm{B}},\\
&\frac{2\pi\gamma}{L}\left\{\left(\hat{\kappa}_{\nu\varphi}(n)-i\frac{Lk}{2\pi}\right)G_{\mathbf{K}n}^{\mathrm{B}} - \frac{1}{2}\left(\frac{L}{2\pi l}\right)^2\left(G_{\mathbf{K}n-1}^{\mathrm{B}} - G_{\mathbf{K}n+1}^{\mathrm{B}}\right)\right\} = \varepsilon G_{\mathbf{K}n}^{\mathrm{A}}.
\end{aligned} \tag{3.35}$$

with

$$\hat{\kappa}_{\nu\varphi}(n) = n+\varphi-\frac{\nu}{3}. \tag{3.36}$$

The strength of the magnetic field is characterized by $L/2\pi l$, which is the ratio of the radius of a CN and the magnetic length. The equation for $G_{\mathbf{K}'n}^{\mathrm{A,B}}$ at the K' point is given by the replacement of $\nu$ by $-\nu$, $k$ by $-k$, and $(L/2\pi l)^2$ by $-(L/2\pi l)^2$.

Figure 17 shows calculated energy levels for a metallic ($\nu=0$) and semiconducting ($\nu=\pm1$) CN. With increasing magnetic field the energy levels for small $k$ approach those of Landau levels of a graphite sheet denoted by the dashed lines. Because there always exists a Landau level at $\varepsilon=0$ in the graphite sheet, the band gap of semiconducting CN's tends to zero with increasing magnetic field. In strong magnetic fields $L/2\pi l=2.5$, for example, both energy bands and wave functions become independent of $\nu$ in contrast to the case in the absence of a field where the band gap depends on $\nu$ quite sensitively.

Figure 18 shows the band gap for various values of the zero-field band-gap as a function of $L/2\pi l$. The band gap becomes negligible when $L/2\pi l$ is much larger than unity as has been mentioned above.



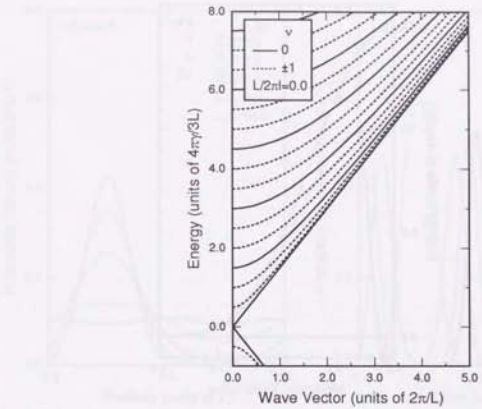


(a)

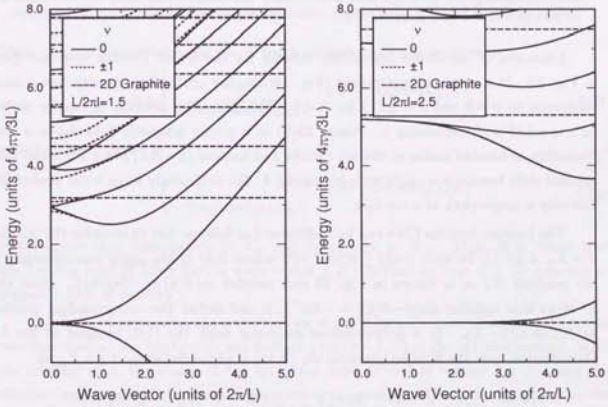


(b) (c)

**Fig. 17** The energy bands of metallic (solid lines) and semiconducting (dotted lines) CN in the absence and presence of a magnetic field perpendicular to the tube axis. (a) $L/2\pi l=0$, (b) $L/2\pi l=1.5$, and (c) $L/2\pi l=2.5$. The dashed lines represent the Landau levels of a graphite sheet.

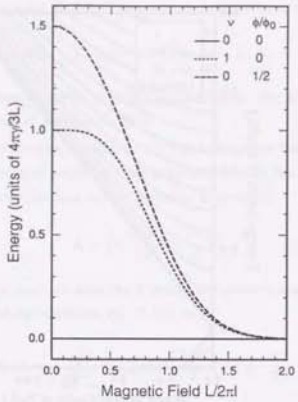


**Fig. 18** Calculated band gap as a function of a magnetic field. The solid line represents the gap for metallic CN ($\nu = 0$ and $\phi = 0$), the dotted line that for semiconducting CN ($\nu = \pm 1$ and $\phi = 0$), and the dashed line that for CN with a largest gap ($\nu = 0$ and $\phi/\phi_0 = 1/2$).

Examples of calculated probability density for the lowest Landau level are given in Fig. 19. In a weak magnetic field (Fig. 19(a)), the probability density has a small maximum at $x = 0$ and $x = \pm L/2$ for $k = 0$. The maximum position is rapidly shifted to $x = -L/4$ with increasing $k$. Figure 19(b) in a strong magnetic field shows a clear formation of Landau states at the top ($x = 0$) and bottom ($x = \pm L/2$) for $k = 0$ and their gradual shift toward $x = -L/4$ with increasing $k$. For sufficiently large $k$ the probability has only a single peak at $x = -L/4$.

The Landau level for CN's can be understood as follows: Let us consider the position $x = X_+ \equiv L\theta(k)/2\pi$ with $-\pi/2 \le \theta(k) < \pi/2$ where $\theta(k)$ is the angle corresponding to the position $X_+$ as is shown in Fig. 20 and satisfies $\sin\theta(k) = -2\pi l^2 k/L$. Note that $\pi - \theta(k)$ also satisfies $\sin[\pi - \theta(k)] = -2\pi l^2 k/L$ and define the corresponding position as $X_- \equiv L/2 - X_+$. In a perpendicular magnetic field, the (1,2) element of the **k·p** Hamiltonian near the K point given by eq. (3.15) is expanded around $x = X_\pm$ as

$$\gamma\left[\frac{1}{\mathrm{i}}\frac{\partial}{\partial x} - \mathrm{i}\left(k + \frac{e}{c\hbar}\frac{LH}{2\pi}\sin\frac{2\pi x}{L}\right)\right] \approx -\mathrm{i}\gamma\left[\frac{\partial}{\partial x} + \frac{x - X_\pm}{l^2}\cos\frac{2\pi X_\pm}{L}\right] = \begin{cases} \sqrt{2}\gamma L_-\sqrt{\cos\theta(k)}/l & \text{for } X_+ \\ \sqrt{2}\gamma L_+\sqrt{\cos\theta(k)}/l & \text{for } X_- \end{cases} \tag{3.37}$$



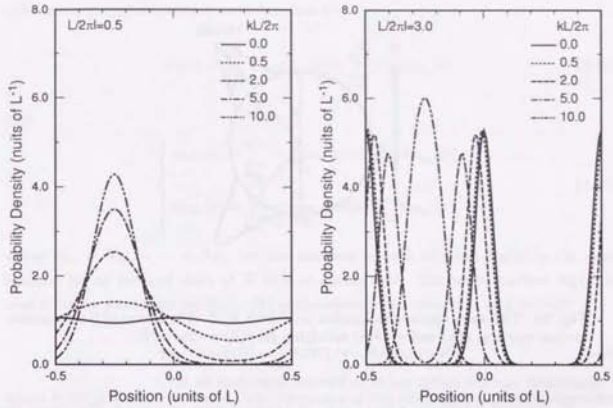


(a) (b)

**Fig. 19** Some examples of calculated probability density of the lowest conduction subband of a metallic CN in magnetic fields. (a) $L/2\pi l = 0.5$ and (b) $L/2\pi l = 3$.

Then, the **k·p** Hamiltonian for the K point around $x = X_\pm$ is written as

$$\mathcal{H} = \begin{pmatrix} 0 & \sqrt{2}\gamma\sqrt{\cos\theta(k)}L_\mp/l \\ \sqrt{2}\gamma\sqrt{\cos\theta(k)}L_\pm/l & 0 \end{pmatrix}, \tag{3.38}$$

and that for K' point as

$$\mathcal{H} = \begin{pmatrix} 0 & \sqrt{2}\gamma\sqrt{\cos\theta(k)}L_\pm/l \\ \sqrt{2}\gamma\sqrt{\cos\theta(k)}L_\mp/l & 0 \end{pmatrix}, \tag{3.39}$$

where upper sign corresponds to $X_+$ and lower sign to $X_-$. Thus, it is found that the Landau level of CN's having wave vector $k$ is regarded as that of a 2D graphite in magnetic field $H\cos\theta(k)$.

For $k = 0$, in particular, the wavefunction is given by a linear combination of Landau wavefunctions at the top ($x = 0$) and bottom part ($x = L/2$) of the cylinder surface. With the increase of $k$, the center of the cyclotron orbit is shifted toward $x = L/4$ and the effective magnetic field decreases in proportion to $\cos\theta(k)$. Those states stay just at the Fermi energy independent of $k$, since they correspond to a Landau level in 2D graphite sheet, existing at the Fermi energy independent of the field. With further increase of $k > k_H$, two Landau wavefunctions with center $X_+$ and $X_-$ start to overlap each other

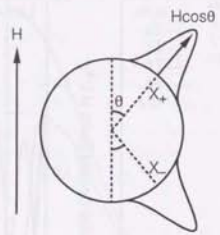


**Fig. 20** The wave function in Landau level with $k>0$. The center of the cyclotron motion exists at $\theta(k)$ and $\pi-\theta(k)$ satisfying $\sin\theta(k)=-2\pi l^2 k/L$.

appreciably and the energy starts to become dependent on $k$.

In the high-field limit $L/2\pi l \to \infty$ the critical wave vector $Lk_H/2\pi$ approaches $(L/2\pi l)^2$ and the corresponding angle $\theta_H$ becomes $\pi/2$. Actual numerical results show that $k_H$ is approximately given by

$$\frac{Lk_H}{2\pi} \sim 0.873\times\left(\frac{L}{2\pi l}\right)^2 - 2.118, \tag{3.40}$$

which is valid within a few percent for $(L/2\pi l)^2 \lesssim 20$.

## 3.2 Tight-Binding Model

### 3.2.1 Hamiltonian

Let us calculate full energy bands in a magnetic field using a tight-binding model. We choose the $y$ axis along the tube axis and the $z$ axis in the direction of a magnetic field. Note that the $x$ axis is perpendicular to the $y$ and $z$ axes, different from the coordinate system of Fig. 11. In a magnetic field a unit cell should usually be extended such that the total flux is an integer multiple of the flux quantum $\phi_0$. In the case of CN's, however, the total flux passing through the unit cell in the absence of a magnetic field always vanishes because of the cancellation between the field passing into and out of CN. Therefore the unit cell or the first Brillouin zone of CN's does not change even in a magnetic field.

Let us denote carbon atoms in the unit cell as $\mathrm{A}_i$ and $\mathrm{B}_i$ with $i=1,2,\cdots,N$. In the



tight-binding approximation a wave function is

$$\psi_k(\mathbf{r}) = \sum_{i=1}^{N} C_{\mathrm{A}_i}\varphi_{k\mathrm{A}_i}(\mathbf{r}) + \sum_{i=1}^{N} C_{\mathrm{B}_i}\varphi_{k\mathrm{B}_i}(\mathbf{r}), \tag{3.41}$$

with

$$\begin{cases} \varphi_{k\mathrm{A}_i}(\mathbf{r}) = \displaystyle\sum_{\mathbf{R}_{\mathrm{A}_i}} \frac{1}{\sqrt{N_{\mathrm{A}_i}}}\exp(ikR^y_{\mathrm{A}_i})\Phi_{\mathbf{R}_{\mathrm{A}_i}}(\mathbf{r}), \\ \varphi_{k\mathrm{B}_i}(\mathbf{r}) = \displaystyle\sum_{\mathbf{R}_{\mathrm{B}_i}} \frac{1}{\sqrt{N_{\mathrm{B}_i}}}\exp(ikR^y_{\mathrm{B}_i})\Phi_{\mathbf{R}_{\mathrm{B}_i}}(\mathbf{r}), \end{cases} \tag{3.42}$$

where $N_{\mathrm{A}_1} = N_{\mathrm{B}_1} = \cdots = N_{\mathrm{B}_N}$ are the numbers of each site and $\Phi_{\mathbf{R}}(\mathbf{r})$ is the wave function for an isolated atom at $\mathbf{R}$ in a magnetic field. The wave function $\Phi_{\mathbf{R}}(\mathbf{r})$ is related to the wave function $\Phi_0(\mathbf{r}-\mathbf{R})$ in the absence of a magnetic field through

$$\Phi_{\mathbf{R}}(\mathbf{r}) = \exp\Big[-\frac{ie}{\hbar c}\mathbf{A}(\mathbf{R})\cdot(\mathbf{r}-\mathbf{R})\Big]\Phi_0(\mathbf{r}-\mathbf{R}), \tag{3.43}$$

where $\mathbf{A}(\mathbf{R})$ is a vector potential. The derivation of this expression is given in Appendix A.

For simplicity we assume that transfer integrals do not vanish only between nearest neighbors and the overlapping of the wave functions at different atoms is neglected. Let $\mathbf{R}$ and $\mathbf{R}'$ be positions of nearest neighbor atoms. Then, the matrix element is written as

$$\begin{aligned} H_{\mathbf{R}\mathbf{R}'} &\simeq \int d\mathbf{r}\,\Phi_{\mathbf{R}}(\mathbf{r})^*\Big[\frac{\hat{\mathbf{p}}^2}{2m}+V(\mathbf{r}-\mathbf{R})+V(\mathbf{r}-\mathbf{R}')\Big]\Phi_{\mathbf{R}'}(\mathbf{r}) \\ &= \frac{1}{2}\int d\mathbf{r}\,\Phi_{\mathbf{R}}(\mathbf{r})^*\Big[\frac{\hat{\mathbf{p}}^2}{2m}+V(\mathbf{r}-\mathbf{R})+\frac{\hat{\mathbf{p}}^2}{2m}+V(\mathbf{r}-\mathbf{R}')\Big]\Phi_{\mathbf{R}'}(\mathbf{r}) \\ &\quad+\frac{1}{2}\int d\mathbf{r}\,\Phi_{\mathbf{R}}(\mathbf{r})^*\Big[V(\mathbf{r}-\mathbf{R})+V(\mathbf{r}-\mathbf{R}')\Big]\Phi_{\mathbf{R}'}(\mathbf{r}), \end{aligned} \tag{3.44}$$

where $\hat{\mathbf{p}} = \mathbf{p}+(e/ch)\mathbf{A}$ and $V(\mathbf{r})$ is the potential of an atom located at the origin. The first term vanishes because it is proportional to the overlapping integral. We then have

$$H_{\mathbf{R}\mathbf{R}'} = \int d\mathbf{r}\,\Phi_0(\mathbf{r}-\mathbf{R})^*\mathcal{H}'\Phi_0(\mathbf{r}-\mathbf{R}')\exp\Big\{\frac{ie}{\hbar c}[\mathbf{A}(\mathbf{R})\cdot(\mathbf{r}-\mathbf{R})-\mathbf{A}(\mathbf{R}')\cdot(\mathbf{r}-\mathbf{R}')]\Big\}, \tag{3.45}$$

with

$$\mathcal{H}' = \frac{1}{2}[V(\mathbf{r}-\mathbf{R})+V(\mathbf{r}-\mathbf{R}')]. \tag{3.46}$$

In the case $l \gg a$ we can safely replace $\mathbf{r}$ in the phase factor appearing in eq. (3.45) by $(\mathbf{R}+\mathbf{R}')/2$ because the expansion in terms of the exponent rapidly converges. We shall use the same approximate expression even for $l \sim a$ in the following, assuming that

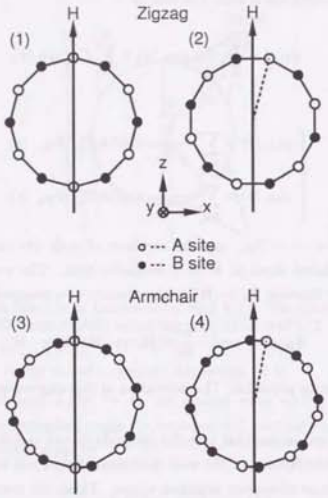


**Fig. 21** Cross section of zigzag and armchair CN's and the coordinate system used in tight-binding calculations. (1) and (2) correspond to the microscopic orientation used for zigzag nanotubes and (3) and (4) correspond to that for armchair nanotubes. Open circles and closed circles represent A and B carbon atoms, respectively.

electrons are strongly localized at each atom. In this case the transfer integral comes from the region in the vicinity of the middle point of two atoms.

The matrix element of the Hamiltonian in the basis of $\varphi_{\mathrm{A}_i}$ and $\varphi_{\mathrm{B}_j}$ is given by

$$H_{\mathrm{A}_i\mathrm{B}_j} \simeq -\gamma_0 \exp[\mathrm{i}k(R^y_{\mathrm{B}_j}-R^y_{\mathrm{A}_i})] \exp\left\{-\frac{1}{2}\frac{\mathrm{i}e}{\hbar c}[\mathbf{A}(\mathbf{R}_{\mathrm{B}_j})+\mathbf{A}(\mathbf{R}_{\mathrm{A}_i})]\cdot(\mathbf{R}_{\mathrm{A}_i}-\mathbf{R}_{\mathrm{B}_j})\right\}. \quad (3.47)$$

In a Landau gauge, the vector potential is given by $(0, Hx, 0)$ and the matrix elements are written explicitly as

$$H_{\mathrm{A}_i\mathrm{B}_j} = -\gamma_0 \exp\left\{\mathrm{i}\left[k+\frac{1}{2l^2}(R^x_{\mathrm{A}_i}+R^x_{\mathrm{B}_j})\right](R^y_{\mathrm{B}_j}-R^y_{\mathrm{A}_i})\right\}. \quad (3.48)$$

The energy bands can be calculated by diagonalizing $2N\times 2N$ matrix with off-diagonal elements given above and diagonal elements $H_{\mathrm{A}_i\mathrm{A}_i}$ and $H_{\mathrm{B}_i\mathrm{B}_i}$, which are the energy of



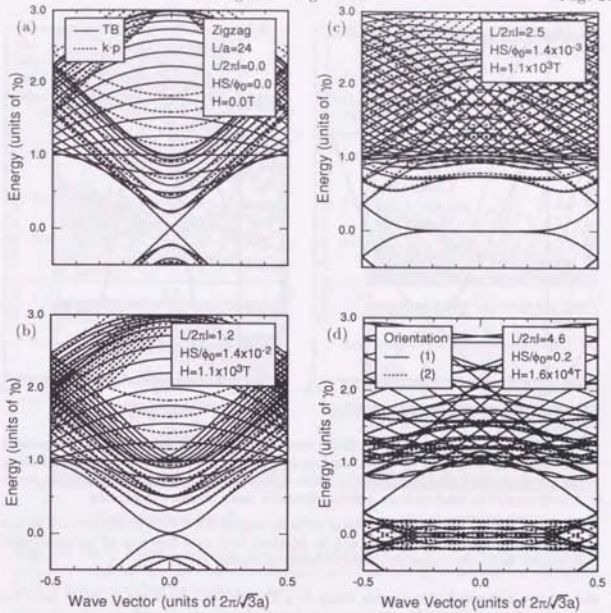


**Fig. 22** The band structure of a metallic zigzag CN ($L/a=24$ or $m=24$) in a magnetic field perpendicular to the tube axis. (a) $L/2\pi l=0$, (b) 1.2, (c) 2.5, and (d) 4.6. In (a), (b), and (c) the solid lines represent the bands calculated in the tight-binding model and the dotted lines those calculated in the lowest-order $\mathbf{k}\cdot\mathbf{p}$ theory. In (d) the solid and dotted lines represent tight-binding bands for two different microscopic orientations of CN with respect to the field direction as is illustrated in Fig. 21 (1) and (2), respectively.

$p_z$ orbital and chosen to be zero. In the following we shall confine ourselves to metallic CN's having zigzag or armchair structure, which is shown in Fig. 15, in the absence of magnetic flux passing through the axis.

### 3.2.2 Zigzag nanotubes

A zigzag CN has a chiral vector $\mathbf{L}=m\mathbf{a}$ with circumference length being $L=ma$ and the first Brillouin zone $-\pi/\sqrt{3}a \le k < \pi/\sqrt{3}a$. A zigzag CN is metallic for $m$ being multiple of 3 and semiconducting for all other $m$'s. Since both K and K' points where

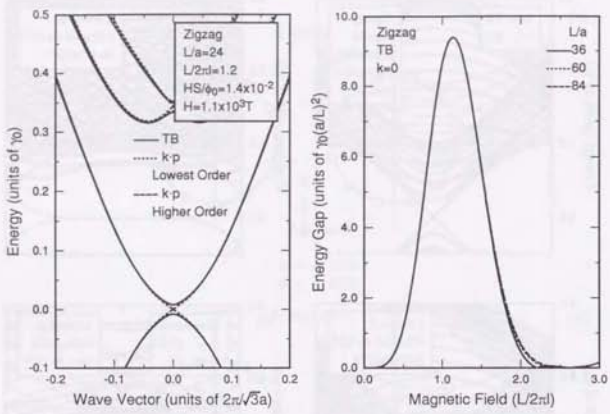


**Fig. 23** (Left) A blow-up of Fig. 22(b) near the Fermi level. The solid lines represent the bands calculated in the tight-binding model, the dotted lines those calculated in the lowest-order $\mathbf{k}\cdot\mathbf{p}$ theory, and the dashed lines those calculated in the higher-order $\mathbf{k}\cdot\mathbf{p}$ theory. The dashed lines overlap the solid lines almost completely.

**Fig. 24** (Right) A small band gap of metallic zigzag CN's with circumference $L/a=36$ (solid line), 60 (dotted line), and 84 (dashed line) as a function of perpendicular magnetic field calculated in the tight-binding model.

the valence and conduction bands touch in a 2D graphite sheet are mapped onto $k=0$, valence and conduction bands are always two-fold degenerate.

The calculated energy bands of a zigzag CN with $L/a=m=24$ are shown in Fig. 22. The magnetic-field strength is characterized by $L/2\pi l$ and also by $HS/\phi_0$. The latter is the ratio of magnetic flux passing through a hexagon with area $S=\sqrt{3}a^2/2$ to magnetic flux quantum $\phi_0$ and $HS/\phi_0=1$ corresponds to $7.9\times10^4$T. The former is the parameter introduced in the $\mathbf{k}\cdot\mathbf{p}$ theory (eq. (3.35)). As is shown below, the validity of the $\mathbf{k}\cdot\mathbf{p}$ theory is determined only by the condition $HS/\phi_0\ll1$, which is usually satisfied.

Figures 22(a), (b), and (c) represent the results for $HS/\phi_0\ll1$ and contain those calculated in the $\mathbf{k}\cdot\mathbf{p}$ theory. The bands calculated in the $\mathbf{k}\cdot\mathbf{p}$ theory are in excellent agreement with those in the tight-binding model particularly near the Fermi level.

Figure 22(d) gives the results for $HS/\phi_0=0.2$. The energy bands deviate from those obtained in the $\mathbf{k}\cdot\mathbf{p}$ theory considerably. This can be seen most easily from a large Harper broadening of the bands in the vicinity of the Fermi level. Further, the bands depend also on the microscopic orientation of a CN. In fact, the solid lines show



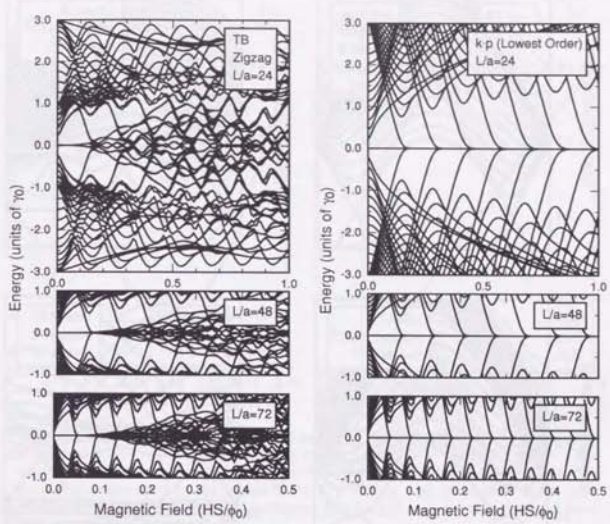


**Fig. 25** (Left) Energy bands at $k=0$ for metallic zigzag CN's with circumference $L/a=24$ (top), 48 (middle), and 72 (bottom) as a function of perpendicular magnetic field calculated in the tight-binding model.

**Fig. 26** (Right) Energy bands calculated in the lowest-order $\mathbf{k}\cdot\mathbf{p}$ theory corresponding to Fig. 25.

the bands for the orientation of magnetic field given in Fig. 21 (1) and the dotted lines for the orientation in Fig. 21 (2). For $HS/\phi_0\ll1$, this dependence on the microscopic orientation is negligibly small.

There is a small deviation from the result of the $\mathbf{k}\cdot\mathbf{p}$ theory in intermediate magnetic fields $L/2\pi l\sim1$, although it is not clearly seen in Fig. 22(b). Figure 23, a blow-up of the energy bands near the Fermi level for $L/2\pi l=1.2$, shows the opening of a small band-gap at $k=0$ in contrast to no band-gap predicted in the $\mathbf{k}\cdot\mathbf{p}$ theory. Figure 24 shows the band gap as a function of the magnetic field for three zigzag nanotubes with different circumference lengths. The band gap clearly falls on a universal curve independent of $L/a$ if measured in units of $\gamma_0(a/L)^2$. It will be shown below that this small gap is a result of higher order terms in the $\mathbf{k}\cdot\mathbf{p}$ perturbation.

The top of Fig. 25 gives the energy bands at $k=0$ for metallic zigzag CN's as a

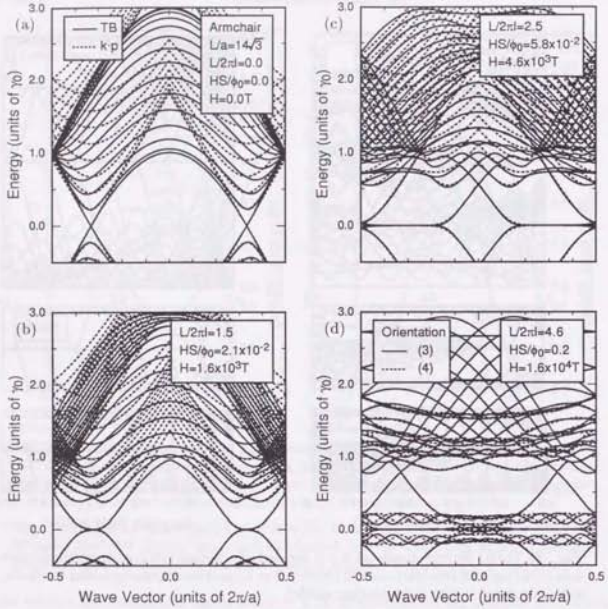


**Fig. 27** The band structure of an armchair CN ($L/a = 14\sqrt{3}$ or $m = 14$) in a magnetic field perpendicular to the tube axis. (a) $L/2\pi l = 0$, (b) 1.5, (c) 2.5, and (d) 4.6. In (a), (b), and (c) the solid lines represent the bands calculated in the tight-binding model and the dotted lines those calculated in the lowest-order $\mathbf{k}\cdot\mathbf{p}$ theory. In (d) the solid and dashed lines represent tight-binding bands for two different microscopic orientations of CN with respect to the field direction as is illustrated in Fig. 21 (3) and (4), respectively.

function of a magnetic field, $HS/\phi_0$. It is noted that a huge oscillation of the total band width reported by Saito *et al.*[47] is not reproduced in the present calculation.[48] The middle and the bottom of Fig. 25 show the energy bands in the range of $-\gamma_0 \le \varepsilon \le \gamma_0$ at $k = 0$ for CN's with larger circumference lengths.

Figure 26 gives the corresponding results obtained in the $\mathbf{k}\cdot\mathbf{p}$ theory. The $\mathbf{k}\cdot\mathbf{p}$ theory works quite well for the energy range close to the Fermi level ($\varepsilon = 0$) in weak magnetic fields $HS/\phi_0 \lesssim 0.1$. Since the range of $k$ where the Landau level is formed is given in eq. (3.40) in high magnetic fields, it easily exceeds the boundary of the first Brillouin zone



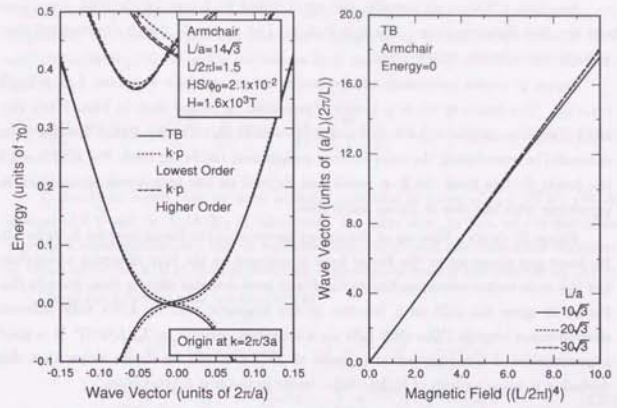


**Fig. 28** (Left) A blow-up of Fig. 27(b) near the Fermi level. Only the part in the vicinity of $k = 2\pi/3a$ is shown and that near $k = -2\pi/3a$ is its mirror image. The solid lines represent the bands calculated in the tight-binding model, the dotted lines those calculated in the lowest-order $\mathbf{k}\cdot\mathbf{p}$ theory, and the dashed lines those calculated in the higher-order $\mathbf{k}\cdot\mathbf{p}$ theory. The dashed lines overlap the solid lines almost completely.

**Fig. 29** (Right) The shift in the wave vector at which the valence and conduction bands touch for armchair CN's with circumference $L/a = 10$ (solid line), 20 (dotted line), and 30 (dashed line) as a function of perpendicular magnetic field calculated in the tight-binding model.

for CN's with large circumference length in high magnetic fields. The merging of bands both from above and below at $HS/\phi_0 = 0.08$ for $L/a = 48$ and $HS/\phi_0 = 0.04$ for $L/a = 72$ is a result of the folding of such Landau-level-like bands.

As is shown in eq. (3.48) the expansion parameter to obtain the $\mathbf{k}\cdot\mathbf{p}$ Hamiltonian is not $k_y$ but $k_y + R^x/l^2$. Therefore, the $\mathbf{k}\cdot\mathbf{p}$ theory is valid even for large $k$ in high magnetic fields as long as the energy is close to the Fermi level. This means that the Landau level near the Fermi level is always well represented by the $\mathbf{k}\cdot\mathbf{p}$ theory. The $\mathbf{k}\cdot\mathbf{p}$ theory starts to break down when a Landau level starts to have a dispersion and be broadened (the Harper broadening). For the Landau level lying at the Fermi level, the critical field is estimated as $HS/\phi_0 \sim 0.1$, corresponding to $7.9 \times 10^3$ T. The critical field is smaller for Landau levels away from the Fermi level as is expected.

### 3.2.3 Armchair nanotubes

Armchair CN's are all metallic and are specified by $\mathbf{L}=m(2\mathbf{a}+\mathbf{b})$ with $L=\sqrt{3}ma$ and the first Brillouin zone $-\pi/a \le k < \pi/a$. The K and K' points are mapped onto $+2\pi/3a$ and $-2\pi/3a$, respectively.

Figure 27 shows calculated energy bands for an armchair nanotube $L/a=14\sqrt{3}$ ($m=14$). The bands in the $\mathbf{k}\cdot\mathbf{p}$ theory represented by dotted lines in Figs. 27(a), (b), and (c) are calculated around both $k=-2\pi/3a$ and $2\pi/3a$. The $\mathbf{k}\cdot\mathbf{p}$ theory is again quite successful in reproducing the tight-binding results near the Fermi level. For $HS/\phi_0=0.2$ the bands deviate from the $\mathbf{k}\cdot\mathbf{p}$ result and depend on the microscopic orientation in agreement with the case of zigzag nanotubes.

Figure 28 shows a blow-up of the energy bands near the Fermi level for $L/2\pi l=1.5$. No band gap opens up at the Fermi level in contrast to the case of zigzag nanotubes, but the wave vector corresponding to the Fermi level deviates slightly from $k=\pm 2\pi/3a$. Figure 29 gives the shift as a function of the magnetic field for CN's with different circumference lengths. The shift falls on a universal curve $\propto (a/L)(L/2\pi l)^4$ in a good approximation if being measured in units of $2\pi/L$. It will be shown below that this deviation is again a result of higher order terms in the $\mathbf{k}\cdot\mathbf{p}$ perturbation.

## 3.3 Effective-Mass Theory in Higher Order

### 3.3.1 Hamiltonian

Let us consider a 2D graphite sheet. First we make a difference equation with respect to envelope functions and then take a continuum limit to get a higher order $\mathbf{k}\cdot\mathbf{p}$ Hamiltonian. In the tight-binding model, the wave function is expressed in terms of envelope wave functions at the K point as

$$\psi(\mathbf{r}) = \sum_{i=\mathrm{A,B}} \sum_{\mathbf{R}_i} \frac{1}{\sqrt{N_i}} F_{\mathbf{K}}^{i}(\mathbf{R}_i) \exp(\mathrm{i}\mathbf{K}\cdot\mathbf{R}_i)\Phi_{\mathbf{R}_i}(\mathbf{r}), \tag{3.49}$$

with $N_{\mathrm{A}}=N_{\mathrm{B}}$ being a half of the total number of the atomic sites and $\mathbf{K}$ being the wave vector corresponding to the K point given by $(2\pi/a)(1/3, 1/\sqrt{3})$.

The envelope function satisfies the following difference equations:

$$-\gamma_0 \sum_{l=1,2,3} \mathrm{e}^{-\mathrm{i}\mathbf{K}\cdot\vec{\tau}_l} \exp\left\{-\frac{1}{2}\frac{\mathrm{i}e}{\hbar c}[\mathbf{A}(\mathbf{R}_{\mathrm{A}})+\mathbf{A}(\mathbf{R}_{\mathrm{A}}-\vec{\tau}_l)]\cdot\vec{\tau}_l\right\} F_{\mathbf{K}}^{\mathrm{B}}(\mathbf{R}_{\mathrm{A}}-\vec{\tau}_l) = \varepsilon F_{\mathbf{K}}^{\mathrm{A}}(\mathbf{R}_{\mathrm{A}}), \tag{3.50}$$

and a similar one in which $F_{\mathbf{K}}^{\mathrm{A}}$ and $F_{\mathbf{K}}^{\mathrm{B}}$ are exchanged. In the above, $\vec{\tau}$ represents one of the three vectors connecting nearest A and B sites given by

$$\vec{\tau}_1 = \frac{a}{\sqrt{3}}\mathbf{e}'_y, \quad \vec{\tau}_2 = -\frac{a}{2}\mathbf{e}'_x - \frac{a}{2\sqrt{3}}\mathbf{e}'_y, \quad \vec{\tau}_3 = \frac{a}{2}\mathbf{e}'_x - \frac{a}{2\sqrt{3}}\mathbf{e}'_y, \tag{3.51}$$



with $\mathbf{e}'_x$ and $\mathbf{e}'_y$ being unit vectors fixed onto a graphite sheet as is shown in Fig. 11. Expanding the envelope function and vector potential up to the second order of $\vec{\tau}_l\cdot\vec{\nabla}$ and $(\mathrm{i}e/\hbar c)\mathbf{A}(\mathbf{R}_{\mathrm{A}})\cdot\vec{\tau}_l$, we get a continuum-limit equation of eq. (3.50) for the envelope function

$$-\gamma_0 \sum_{l=1,2,3} \mathrm{e}^{-\mathrm{i}\mathbf{K}\cdot\vec{\tau}_l}\left[1-\mathrm{i}\vec{\tau}_l\cdot\left(\frac{\vec{\nabla}}{i}+\frac{e}{\hbar c}\mathbf{A}(\mathbf{r})\right)-\frac{1}{2}\left\{\vec{\tau}_l\cdot\left(\frac{\vec{\nabla}}{i}+\frac{e}{\hbar c}\mathbf{A}(\mathbf{r})\right)\right\}^2\right] F_{\mathbf{K}}^{\mathrm{B}}(\mathbf{r}) = \varepsilon F_{\mathbf{K}}^{\mathrm{A}}(\mathbf{r}). \tag{3.52}$$

It should be noted that we have actually expanded in terms of $\vec{\tau}_l\cdot[-\mathrm{i}\vec{\nabla}+(e/\mathrm{i}\hbar)\mathbf{A}]$ instead of $\vec{\tau}_l\vec{\nabla}$ and $(\mathrm{i}e/\hbar c)\mathbf{A}(\mathbf{R}_{\mathrm{A}})\cdot\vec{\tau}_l$ separately. For large $\mathbf{A}(\mathbf{r})$, in fact, we can first make a gauge transformation such that $\mathbf{A}$ becomes sufficiently small and then make expansion in terms of $(\mathrm{i}e/\hbar c)\mathbf{A}(\mathbf{R}_{\mathrm{A}})\cdot\vec{\tau}_l$. The resulting expression is exactly the same as eq. (3.52).

Using the relations with $\omega=\exp(2\pi\mathrm{i}/3)$:

$$\begin{aligned}
&\sum_l \mathrm{e}^{-\mathrm{i}\mathbf{K}\cdot\vec{\tau}_l}\tau_l^x = \frac{\sqrt{3}}{2}\,\mathrm{i}\,\omega^2 a, \quad \sum_l \mathrm{e}^{-\mathrm{i}\mathbf{K}\cdot\vec{\tau}_l}\tau_l^y = \frac{\sqrt{3}}{2}\omega^2 a,\\
&\sum_l \mathrm{e}^{-\mathrm{i}\mathbf{K}\cdot\vec{\tau}_l}(\tau_l^x)^2 = -\frac{1}{4}\omega^2 a^2, \quad \sum_l \mathrm{e}^{-\mathrm{i}\mathbf{K}\cdot\vec{\tau}_l}(\tau_l^y)^2 = \frac{1}{4}\omega^2 a^2,\\
&\sum_l \mathrm{e}^{-\mathrm{i}\mathbf{K}\cdot\vec{\tau}_l}\tau_l^x\tau_l^y = -\frac{1}{4}\,\mathrm{i}\,\omega^2 a^2,
\end{aligned} \tag{3.53}$$

the $\mathbf{k}\cdot\mathbf{p}$ equation of 2D graphite in the higher order is given by

$$\begin{pmatrix} 0 & \gamma\left[(\hat{k}_x-\mathrm{i}\hat{k}_y)+\frac{a}{4\sqrt{3}}e^{3\mathrm{i}\eta}(\hat{k}_x+\mathrm{i}\hat{k}_y)^2\right] \\ \gamma\left[(\hat{k}_x+\mathrm{i}\hat{k}_y)+\frac{a}{4\sqrt{3}}e^{-3\mathrm{i}\eta}(\hat{k}_x-\mathrm{i}\hat{k}_y)^2\right] & 0 \end{pmatrix} \begin{pmatrix} F_{\mathbf{K}}^{\mathrm{A}}(\mathbf{r}) \\ F_{\mathbf{K}}^{\mathrm{B}}(\mathbf{r}) \end{pmatrix} = \varepsilon \begin{pmatrix} F_{\mathbf{K}}^{\mathrm{A}}(\mathbf{r}) \\ F_{\mathbf{K}}^{\mathrm{B}}(\mathbf{r}) \end{pmatrix}, \tag{3.54}$$

with

$$\hat{\mathbf{k}} = -\mathrm{i}\vec{\nabla} + \frac{e}{\hbar c}\mathbf{A}(\mathbf{r}), \tag{3.55}$$

where $\gamma=\sqrt{3}a\gamma_0/2$ and $\eta$ is the chiral angle between $\mathbf{e}'_x$ axis and the chiral vector $\mathbf{L}$ as is shown in Fig. 11, given by

$$\cos\eta = \begin{cases} \dfrac{2n_a-n_b}{2\sqrt{n_a^2+n_b^2-n_a n_b}} & \text{for } n_a\neq 0, \\ 0 & \text{for } n_a = 0. \end{cases} \tag{3.56}$$

The phase factor $\exp(3\mathrm{i}\eta)$ reflects the trigonal symmetry of 2D graphite and gives warping of the band around the K point.

It is worth noting that the $\mathbf{k}\cdot\mathbf{p}$ Hamiltonian in a magnetic field is obtained by just replacing $\mathbf{k}$ by $-\mathrm{i}\vec{\nabla}+(e/c\hbar)\mathbf{A}$. This corresponds to the fact that the coefficient of $k_x k_y$

is the same as that of $k_y k_x$ in the present case, leading to the absence of antisymmetric terms proportional to $\hat{k}_x\hat{k}_y - \hat{k}_y\hat{k}_x$.[49] The $\mathbf{k}\cdot\mathbf{p}$ Hamiltonian at the K' point can similarly be obtained through the replacement of $\mathbf{K}$ by $\mathbf{K}' = (2\pi/a)(2/3, 0)$. The result is

$$\begin{pmatrix} 0 & \gamma\left[(\hat{k}_x + i\hat{k}_y) - \frac{a}{4\sqrt{3}}e^{-3i\eta}(\hat{k}_x - i\hat{k}_y)^2\right] \\ \gamma\left[(\hat{k}_x - i\hat{k}_y) - \frac{a}{4\sqrt{3}}e^{3i\eta}(\hat{k}_x + i\hat{k}_y)^2\right] & 0 \end{pmatrix} \begin{pmatrix} F^{\mathrm{A}}_{\mathbf{K}'}(\mathbf{r}) \\ F^{\mathrm{B}}_{\mathbf{K}'}(\mathbf{r}) \end{pmatrix} = \varepsilon \begin{pmatrix} F^{\mathrm{A}}_{\mathbf{K}'}(\mathbf{r}) \\ F^{\mathrm{B}}_{\mathbf{K}'}(\mathbf{r}) \end{pmatrix}. \quad (3.57)$$

Thus, the Shrödinger equation near the K' point are obtained by the replacement $\eta \to \eta + \pi/3$ and $\hat{k}_y \to -\hat{k}_y$.

For a 2D graphite there exists a Landau level just at the Fermi energy even in the higher-order $\mathbf{k}\cdot\mathbf{p}$ equation and the wave function is given by

$$C\begin{pmatrix} 0 \\ h_0 + \sum_{n=1}(-1)^n\left(\frac{a}{2\sqrt{6}l}\right)^n \frac{\sqrt{(3n)!}}{3^n n!}e^{3in\eta}h_{3n} \end{pmatrix}, \quad (3.58)$$

where $C$ is a normalization factor. This shows that the Landau level of CN's formed at the Fermi energy is not affected by higher order terms in the $\mathbf{k}\cdot\mathbf{p}$ perturbation. It is worth noting that the sum over the level index $n$ of the harmonic oscillator in eq. (3.58) diverges. It should be cut off at a certain $n_c$ corresponding to the wave vector $k_c \sim \sqrt{2n_c}/l$ where the energy band given in the $\mathbf{k}\cdot\mathbf{p}$ theory starts to deviate from the corresponding actual bands.

The electronic states of CN's are obtained by replacing $k_x$ by discrete wave vectors given by eq. (3.23). Then, the energy levels around the K point are written as

$$\varepsilon = \pm\gamma\left\{\kappa^2 + k^2 + \frac{a}{2\sqrt{3}}[(\kappa^2 - 3k^2)\kappa\cos 3\eta + (k^2 - 3\kappa^2)k\sin 3\eta)] + \frac{a^2}{48}(\kappa^2 + k^2)^2\right\}^{1/2}, \quad (3.59)$$

where the upper (+) and lower (−) signs represent the conduction and valence bands, respectively. A zigzag CN corresponds to $\eta = 0$ and an armchair CN corresponds to $\eta = \pi/6$. Further, the bands for $\eta = \pi/3$ in eq. (3.59) correspond to those of a zigzag CN near the K' point and those for $\eta = \pi/2$ correspond to those of an armchair CN near the K' point.

It turns out from eq. (3.59) that a CN is metallic for $\nu = 0$ and semiconducting for $\nu = \pm 1$. The band gap changes in the presence of magnetic flux passing through the tube axis. These are in complete agreement with the prediction of the lowest order $\mathbf{k}\cdot\mathbf{p}$ theory. However, this band gap is slightly modified in the higher order term.

In a magnetic field perpendicular to the tube axis, we expand the envelope function into plane waves along the $x$ direction as in eq. (3.34) Then the equation for $G^{\mathrm{A,B}}_n$ is



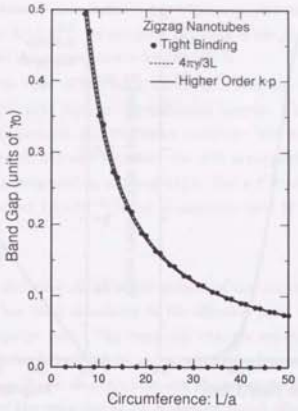


**Fig. 30** Band gap of zigzag nanotubes as a function of the circumference. The dots represent tight-binding results. The dotted line represents $4\pi\gamma/3L$ for semiconducting CN's given in the lowest order $\mathbf{k}\cdot\mathbf{p}$ theory and the solid lines for those given in the higher order $\mathbf{k}\cdot\mathbf{p}$ theory. The shift in the gap due to higher order terms is negative for $\nu = +1$ and positive for $\nu = -1$.

written as

$$\begin{cases} \frac{2\pi\gamma}{L}\sum_n H_{mn}G^{\mathrm{A}}_n = \varepsilon G^{\mathrm{B}}_m, \\ \frac{2\pi\gamma}{L}\sum_n H^*_{nm}G^{\mathrm{B}}_n = \varepsilon G^{\mathrm{A}}_m, \end{cases} \quad (3.60)$$

with

$$\begin{aligned} H_{nn} &= \tilde{\kappa}_{\nu\varphi}(n) + i\frac{Lk}{2\pi} + \frac{\pi}{2\sqrt{3}}\frac{a}{L}e^{-3i\eta}\left\{\left[\tilde{\kappa}_{\nu\varphi}(n) - i\frac{Lk}{2\pi}\right]^2 - \frac{1}{2}\left(\frac{L}{2\pi l}\right)^4\right\}, \\ H_{nn\pm1} &= \left(\frac{L}{2\pi l}\right)^2\left\{\mp\frac{1}{2} \pm \frac{\pi}{2\sqrt{3}}\frac{a}{L}e^{-3i\eta}\left[\tilde{\kappa}_{\nu\varphi}(n \pm 1) - i\frac{Lk}{2\pi} \mp \frac{1}{2}\right]\right\}, \\ H_{nn\pm2} &= \frac{\pi}{8\sqrt{3}}\frac{a}{L}\left(\frac{L}{2\pi l}\right)^4 e^{-3i\eta}. \end{aligned} \quad (3.61)$$

The energy levels can be calculated through the diagonalization of the matrix.

### 3.3.2 Numerical results

Figure 30 compares the band gap of zigzag CN's as a function of the circumference.

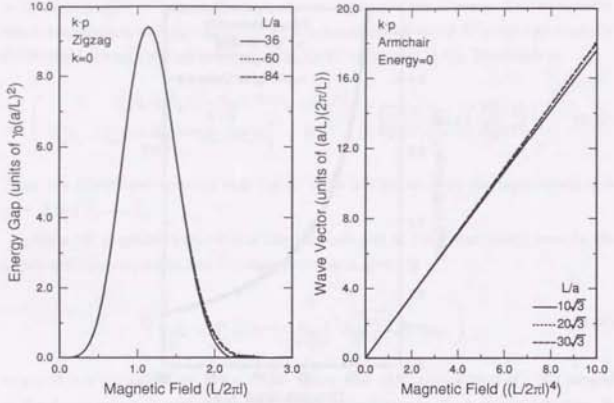


**Fig. 31** (Left) A small band gap of metallic zigzag CN's with circumference $L/a=36$ (solid line), 60 (dotted line), and 84 (dashed line) as a function of perpendicular magnetic field calculated in the higher-order $\mathbf{k}\cdot\mathbf{p}$ theory.

**Fig. 32** (Right) The shift in the wave vector at which the valence and conduction bands touch for armchair CN's with circumference $L/a=10$ (solid line), 20 (dotted line), and 30 (dashed line) as a function of perpendicular magnetic field calculated in the higher-order $\mathbf{k}\cdot\mathbf{p}$ theory.

calculated in the tight-binding model, the lowest order $\mathbf{k}\cdot\mathbf{p}$ theory ($4\pi\gamma/3L$), and the higher order $\mathbf{k}\cdot\mathbf{p}$ theory. The gap calculated in the lowest order $\mathbf{k}\cdot\mathbf{p}$ theory reproduces the tight-binding result remarkably well. The inclusion of higher order terms explains the slight deviation of the tight-binding result from $4\pi\gamma/3L$ depending on the signature of $\nu$. The deviation depending on $\eta$ as $\cos(3\eta)$ has been calculated including the effect of the mixing between $\pi$ and $\sigma$ orbitals due to nonzero curvature and has shown that the mixing enlarges the deviation.[50,51]

Figures 23 and 28 contain the energy bands calculated in this higher-order $\mathbf{k}\cdot\mathbf{p}$ theory. The slight deviation of the tight-binding result from that in the lowest-order $\mathbf{k}\cdot\mathbf{p}$ theory is explained fully by the inclusion of the higher order terms, *i.e.* by the band warping effect.

Figure 31 shows the band gap of metallic zigzag CN's as a function of magnetic field for various circumference lengths. The gap energy is given by a universal function of the magnetic-field parameter $L/2\pi l$ if being measured in units of $\gamma_0(a/L)^2$, in complete agreement with the tight-binding result given in Fig. 24. The term responsible for this



gap is $H_{nn}$ in eq. (3.61) and therefore the gap is proportional to $\gamma_0(a/L)^2(L/2\pi l)^4$ in a weak field. In magnetic field 10 T, for example, the peak in the gap in Fig. 31 corresponds to about 0.51 meV and the circumference length 580 Å.

Figure 32 gives the shift of the wave vector as a function of a magnetic field for armchair CN's ($\eta=\pi/3$) with various circumference lengths. The results again explain the tight-binding result given in Fig. 29 almost perfectly. The term responsible for this shift is again $H_{nn}$ in eq. (3.61) and therefore the shift is proportional to $(a/L)(L/2\pi l)^4$ in a weak field if being measured in units of $2\pi/L$. For a CN with diameter 300 Å, for example, the shift is about $2.4\times10^{-5}(2\pi/a)$ in magnetic field 10 T.

## 3.4 Summary

The energy-band structure of CN in the vicinity of the conduction-band bottom and the valence-band top has been calculated in the effective mass theory in both absence and presence of a magnetic field. The band gap changes sensitively depending on the structure of the nanotube between zero and a nonzero value inversely proportional to the tube diameter. It oscillates also as a function of a magnetic flux passing through the circular cross section of the tube due to an Aharonov-Bohm effect. In the presence of a magnetic field perpendicular to the tube axis, the band gap is reduced due to a formation of 2D Landau states. The energy spectra approach Landau levels of a 2D graphite sheet in high magnetic fields.

The validity of the $\mathbf{k}\cdot\mathbf{p}$ method in a magnetic field perpendicular to the tube axis has been studied in a tight-binding model. For states near the Fermi level, the results of a tight-binding model are in good agreement with those calculated in the lowest order $\mathbf{k}\cdot\mathbf{p}$ theory except in extremely high magnetic fields where the magnetic flux passing through the hexagonal unit cell of a 2D graphite becomes comparable to the flux quantum, *i.e.* $HS/\phi_0 \gtrsim 0.1$.

There are some slight deviations. In weak magnetic fields such that the magnetic length is larger than the circumference length and therefore Landau levels are not formed, a small band gap appears in zigzag CN's and the wave vector crossing the Fermi level is shifted slightly in armchair CN's, in contrast to the predictions of the lowest order $\mathbf{k}\cdot\mathbf{p}$ theory. In high magnetic fields where the magnetic length is smaller than the circumference length, this gap disappears due to the formation of Landau levels corresponding to the cyclotron motion on the top and bottom side of a CN where the perpendicular magnetic field is strongest, in agreement with the prediction of the lowest order $\mathbf{k}\cdot\mathbf{p}$ theory.

The higher order $\mathbf{k}\cdot\mathbf{p}$ Hamiltonian has been derived from the tight-binding model. It leads to a trigonal warping of bands near the K and K' points for a 2D graphite. The deviations of the tight-binding results from the lowest-order $\mathbf{k}\cdot\mathbf{p}$ theory in weak magnetic

fields can be explained by the higher order terms almost perfectly. In particular, it predicts that a weak magnetic field leads to opening of a small band gap in zigzag CN's and a slight shift in the wave vector corresponding to the conduction-band minimum and valence-band maximum from $\pm 2\pi/3a$ (the K or K' points in 2D graphite) in armchair CN's. For other CN's having chirality both modifications occur in general.

These deviations are quite small and the lowest-order $\mathbf{k}\cdot\mathbf{p}$ theory is usually sufficient. Therefore, in the following we shall use the lowest-order $\mathbf{k}\cdot\mathbf{p}$ method and neglect the higher order term completely.

# Chapter 4
# Optical Absorption

In the previous chapter, it has been shown that CN's can be metallic or semiconducting depending on the structure and that the band gap is drastically changed due to the AB effect in a magnetic field passing through the cross section of CN's. In this chapter we shall study the optical absorption spectra which can give direct information on the band gap. [52–54]

This chapter is organized as follows: In Sec. 4.1 dynamical conductivity is obtained. The absorption spectra for polarized light parallel and perpendicular to the tube axis are calculated in Secs. 4.2 and 4.3, respectively. A summary is given in Sec. 4.4.

## 4.1 Dynamical Conductivity

We shall calculate the optical absorption of CN's with an Aharonov-Bohm flux using the linear response theory. We first expand electric field $E_\xi(\theta,\omega)$ and induced current density $j_\xi(\theta,\omega)$ into a Fourier series:

$$\begin{aligned} E_\xi(\theta,\omega) &= \sum_l E_\xi^l(\omega)\exp(il\theta - i\omega t), \\ j_\xi(\theta,\omega) &= \sum_l j_\xi^l(\omega)\exp(il\theta - i\omega t), \end{aligned} \tag{4.1}$$

where $\xi$ denotes $x$ or $y$ and $\theta = 2\pi x/L$ represents the angle shown in Fig. 33 (a). It is quite straightforward to show that the induced current has the same Fourier component as that of the electric field as follows:

$$j_\xi^l(\omega) = \sigma_{\xi\xi}^l(\omega) E_\xi^l(\omega), \tag{4.2}$$

where $\sigma_{\xi\xi}^l(\omega)$ is the dynamical conductivity. The dynamical conductivity near the K point is calculated using the Kubo formula as

$$\sigma_{\xi\xi}^l(\omega) = \frac{1}{i\omega}[K_{\xi\xi}^l(\omega) - K_{\xi\xi}^l(0)], \tag{4.3}$$

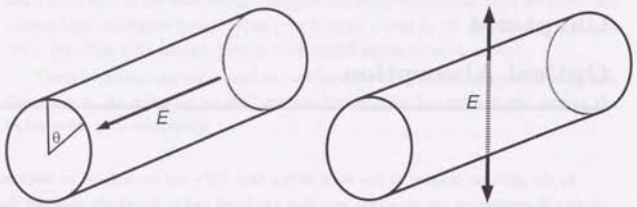


(a) (b)

**Fig. 33** The schematic picture of the polarized electric field parallel (a) and perpendicular (b) to the tube axis.

with

$$K^l_{\xi\xi}(\omega)=-\frac{2}{AL}\sum_{nk}\sum_{v,w=\pm}\frac{f[\varepsilon^{(v)}_{\nu\varphi}(n,k)]-f[\varepsilon^{(w)}_{\nu\varphi}(n+l,k)]}{\varepsilon^{(v)}_{\nu\varphi}(n,k)-\varepsilon^{(w)}_{\nu\varphi}(n+l,k)+\hbar\omega+\mathrm{i}\delta} \times|(n,k,v|\hat{j}^l_\xi|n+l,k,w)|^2 g_0[|\varepsilon^{(v)}_{\nu\varphi}(n,k)|]g_0[|\varepsilon^{(w)}_{\nu\varphi}(n+l,k)|], \tag{4.4}$$

where $f(\varepsilon)$ is the Fermi distribution function, the factor 2 comes from the spin degeneracy, and $g_0(\varepsilon)$ is a cutoff function. The cutoff function has been introduced to get the contribution of the electronic states for which the **k**·**p** approximation is valid. More details on the importance of the cutoff function will be discussed in the following chapters.

The current-density operator $\hat{j}^l_\xi$ at the K point is given by

$$\hat{j}^l_\xi=\frac{-e}{\mathrm{i}\hbar}[\hat{\xi}I_2,\gamma\vec{\sigma}\cdot\hat{\mathbf{k}}]\mathrm{e}^{-\mathrm{i}l\theta}=-\frac{e\gamma}{\hbar}\sigma_\xi\mathrm{e}^{-\mathrm{i}l\theta}, \tag{4.5}$$

where $\hat{\xi}=\hat{x},\hat{y}$ and $I_2$ is a $2\times2$ identity matrix. At the K' point, operator $\hat{j}^l_x$ is the same as that at the K point but $\hat{j}^l_y$ has the opposite sign of that at the K point. The factor $|(n,k,v|\hat{j}^l_\xi|n+l,k,w)|^2$, however, provides the same value for both K and K' points. Substituting eq. (4.4) into eq. (4.3) we get the conductivity

$$\sigma^l_{\xi\xi}(\omega)=\frac{2\hbar}{\mathrm{i}AL}\sum_{nk}\sum_{v,w=\pm}\frac{f[\varepsilon^{(w)}_{\nu\varphi}(n+l,k)]\{1-f[\varepsilon^{(v)}_{\nu\varphi}(k)]\}2\hbar\omega}{[\varepsilon^{(v)}_{\nu\varphi}(n,k)-\varepsilon^{(w)}_{\nu\varphi}(n+l,k)]^2-(\hbar\omega)^2-\mathrm{i}\hbar^2\omega/\tau} \times\frac{|(n,k,v|\hat{j}^l_\xi|n+l,k,w)|^2}{\varepsilon^{(v)}_{\nu\varphi}(n,k)-\varepsilon^{(w)}_{\nu\varphi}(n+l,k)}g_0[|\varepsilon^{(v)}_{\nu\varphi}(n,k)|]g_0[|\varepsilon^{(w)}_{\nu\varphi}(n+l,k)|], \tag{4.6}$$

where phenomenological relaxation time $\tau$ has been introduced. Using eq. (3.25), the



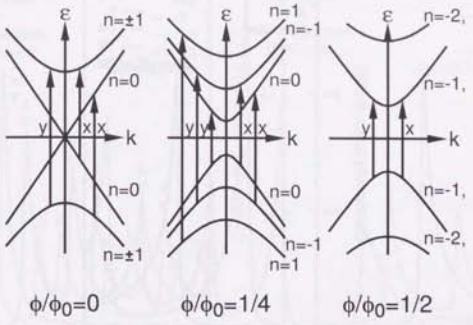


**Fig. 34** The band structures of metallic CN's with $\varphi=0$, 1/4, and 1/2. The arrows denoted by '$x$' and '$y$' show the allowed transitions for $\sigma_{xx}$ and for $\sigma_{yy}$, respectively.

matrix elements of the current-density operator near the K point are given by

$$\begin{aligned}(n,k,+|\hat{j}^l_x|n+l,k,\mp)&=-\frac{e\gamma}{\hbar}\frac{1}{2}\Big[\mp b^*_{\nu\varphi}(n,k)+b_{\nu\varphi}(n+l,k)\Big],\\ (n,k,+|\hat{j}^l_y|n+l,k,\mp)&=-\frac{e\gamma}{\hbar}\frac{\mathrm{i}}{2}\Big[\pm b^*_{\nu\varphi}(n,k)+b_{\nu\varphi}(n+l,k)\Big].\end{aligned} \tag{4.7}$$

## 4.2 Parallel Polarization

When the polarization of external electric field **D** is parallel to the tube axis as is shown in Fig. 33, the Fourier components of a total field are written as

$$E^l_y=D_y\delta_{l,0}.$$

Thus the absorption in a unit area is given by

$$P_y(\omega)=\frac{1}{2}\frac{1}{2\pi}\int_0^{2\pi}\mathrm{d}\theta\mathrm{Re}[j_y(\omega)E_y{}^*]=\frac{1}{2}\mathrm{Re}[\sigma^{l=0}_{yy}(\omega)]D_y^2. \tag{4.8}$$

For $l=0$, transitions occur between bands with the same band index $n$ as is seen from eq. (4.6). Since all the conduction bands are specified by different $n$'s, there is no transition among conduction bands. At a band edge $k=0$, in particular, $b_{\nu\varphi}(n,0)=\mathrm{sgn}[\kappa_{\nu\varphi}(n)]$ with $\mathrm{sgn}[x]$ representing the sign of $x$, and therefore it is found that transitions between valence and conduction bands having the same index $n$ are all allowed.

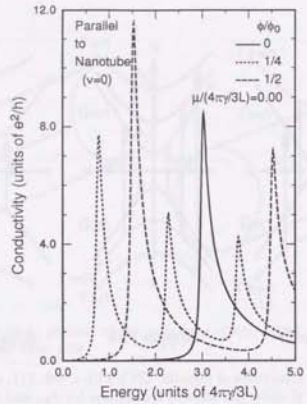


**Fig. 35** Calculated real part of $\sigma_{yy}$ of undoped metallic CN's for $\varphi=0$, 1/4, and 1/2.

In the limit $\tau\to\infty$ absorption spectra near the K point except for intraband Drude terms is proportional to

$$\mathrm{Re}[\sigma_{yy}^{l=0}(\omega)]=\frac{e^2}{h}\sum_n\left[\frac{2\gamma\kappa_{\nu\varphi}(n)}{\hbar\omega}\right]^2\frac{\gamma(2\pi/L)}{\sqrt{(\hbar\omega)^2-[2\gamma\kappa_{\nu\varphi}(n)]^2}} \times\theta[|\hbar\omega|-2\gamma|\kappa_{\nu\varphi}(n)|]g_0(|\hbar\omega|/2)^2, \tag{4.9}$$

where $\theta(x)$ is the step function defined by $\theta(x)=1$ for $x\geq 0$ and $\theta(x)=0$ for $x<0$.

Fig. 35 shows the calculated results of $\mathrm{Re}\sigma_{yy}^{l=0}(\omega)$ of a metallic CN for $\varphi=0$, 1/4, and 1/2. The peaks in Fig. 35 correspond to the transitions shown in Fig. 34. Since elements of the current-density operator for metallic CN's vanish between valence and conduction bands with $n=0$ except at the band edge $k=0$, there is no absorption in the region $\hbar\omega<3.0(4\pi\gamma/3L)$ for metallic CN's with $\varphi=0$. A corresponding result for a semiconducting CN's is given in Fig. 36. The spectra of a semiconducting CN's are more complicated because of the lifting of the degeneracy between the K and K' points in the presence of a magnetic flux.

Figure 37 exhibits $\mathrm{Re}[\sigma_{yy}^{l=0}(\omega)]$ of an electron-doped metallic CN. The electron concentration is fixed in such a way that the chemical potential in the absence of a magnetic flux is given by $\mu=(3/4)(4\pi\gamma/3L)$. For this doping, only the lowest conduction band is occupied for $\varphi=0$ and 1/4, while two degenerate lowest bands are occupied for $\varphi=1/2$.



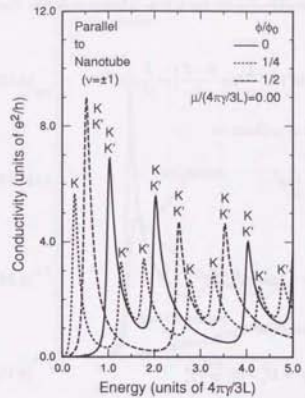


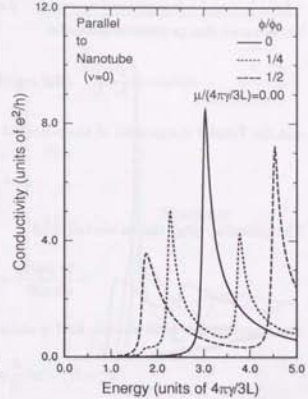


**Fig. 36** (Left) Calculated real part of $\sigma_{yy}$ of undoped semiconducting CN's for $\varphi=0$, 1/4, and 1/2. The symbols K and K' show transitions between states near the K and K' points, respectively.

**Fig. 37** (Right) Calculated real part of $\sigma_{yy}$ of doped metallic CN's for $\varphi=0$, 1/4, and 1/2.

These figures demonstrate clearly that the AB effect on the band structure manifests itself as a shift of the absorption peaks.

## 4.3 Perpendicular Polarization

When an external electric field is polarized in the direction perpendicular to the CN axis, effects of an electric field induced by the polarization of nanotubes should be considered. This depolarization effect is quite significant for absorption spectra.

Suppose an external electric field $D_x^l\exp(il\theta-i\omega t)$ is applied in the direction normal to the tube axis and let $j_x^l$ be the induced current. With the use of the equation of continuity

$$\frac{\partial}{\partial t}\rho^l e^{il\theta-i\omega t}+\frac{2\pi}{L}\frac{\partial}{\partial\theta}j_x^l e^{il\theta-i\omega t}=0, \tag{4.10}$$

the corresponding induced charge density localized on the cylinder surface is written as

$$\rho^l=\frac{2\pi}{L}\frac{l}{\omega}j_x^l. \tag{4.11}$$

The potential formed by line charge with the density $\rho dx$ at distance $r$ is given by

$-2\rho \mathrm{d}x \ln r$ and $r$ is expressed as $r=(L/\pi)|\sin[(\theta-\theta')/2]|$ for CN's. Then it is found that the induced charge leads to potential

$$\phi(\theta)=-2\frac{L}{2\pi}\int_0^{2\pi}\mathrm{d}\theta'\rho^l\exp(\mathrm{i}l\theta')\ln\left|\frac{L}{\pi}\sin\frac{\theta-\theta'}{2}\right|=\frac{L}{|l|}\rho^l\mathrm{e}^{\mathrm{i}l\theta}, \tag{4.12}$$

and the Fourier component of the potential is written as

$$\phi^l=\frac{L}{|l|}\rho^l. \tag{4.13}$$

The potential gives rise to electric field

$$-\frac{2\pi}{L}\frac{\partial\phi(\theta)}{\partial\theta}=-2\pi\mathrm{i}\frac{l}{|l|}\rho^l\mathrm{e}^{\mathrm{i}l\theta}, \tag{4.14}$$

and therefore the total electric field is obtained as

$$E_x^l=D_x^l-2\pi\mathrm{i}\frac{l}{|l|}\rho^l=D_x^l-\mathrm{i}|l|\frac{4\pi^2}{L\omega}j_x^l. \tag{4.15}$$

With the use of $j_x^l=\sigma_{xx}^l E_x^l$ we get

$$j_x^l=\tilde{\sigma}_{xx}^l D_x^l, \tag{4.16}$$

with

$$\tilde{\sigma}_{xx}^l=\sigma_{xx}^l\left(1+\mathrm{i}|l|\frac{4\pi^2}{L\omega}\sigma_{xx}^l\right)^{-1}. \tag{4.17}$$

For the external field being $\mathbf{D}=(D_x\sin\theta,0)$, the Fourier components of the external field and the induced current are written as

$$\begin{aligned} D_x^l&=\frac{D_x}{2\mathrm{i}}\delta_{l,1}-\frac{D_x}{2\mathrm{i}}\delta_{l,-1},\\ j_x^l&=\frac{D_x}{2\mathrm{i}}\sigma_{xx}^{l=1}(\omega)\delta_{l,1}-\frac{D_x}{2\mathrm{i}}\sigma_{xx}^{l=-1}(\omega)\delta_{l,-1}. \end{aligned} \tag{4.18}$$

Thus the absorption is given by

$$P_x(\omega)=\frac{1}{2}\frac{1}{2\pi}\int_0^{2\pi}\mathrm{d}\theta\mathrm{Re}[j_x(\omega)E_x^*]=\frac{1}{4}\mathrm{Re}[\tilde{\sigma}_{xx}(\omega)]D_x^2, \tag{4.19}$$

with

$$\tilde{\sigma}_{xx}=\frac{1}{2}(\tilde{\sigma}_{xx}^{l=1}+\tilde{\sigma}_{xx}^{l=-1}). \tag{4.20}$$

According to eq. (4.6) the absorption occurs between bands having band index $n$ and



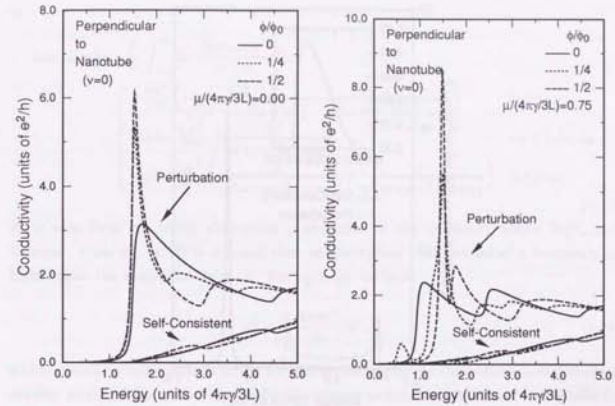


**Fig. 38** (Left) Calculated real part of $\sigma_{xx}$ (indicated by 'Perturbation') and $\tilde{\sigma}_{xx}$ (indicated by 'Self-Consistent') of undoped metallic CN's for $\varphi=0$, 1/4, and 1/2.

**Fig. 39** (Right) Calculated real part of $\sigma_{xx}$ and $\tilde{\sigma}_{xx}$ of doped metallic CN's for $\varphi=0$, 1/4, and 1/2.

$n\pm1$.

Let us consider a spectral edge corresponding to $k=0$ in which $b_{\nu\varphi}(n,0)=\mathrm{sgn}[\kappa_{\nu\varphi}(n)]$. From eq. (4.7) it is found that transitions between valence- and conduction-band states become allowed only when $\kappa_{\nu\varphi}(n)$ and $\kappa_{\nu\varphi}(n\pm1)$ have a sign opposite to each other. This leads to the conclusion in a metallic CN's, for example, that transitions from $n=0$ to $n=-1$ and from $n=-1$ to $n=0$ are allowed for $0\le\varphi<1$ as is shown in Fig. 34. Note that the corresponding energy $2\pi\gamma/L$ remains independent of an AB flux. Transitions between conduction bands become allowed for $\kappa_{\nu\varphi}(n)$ and $\kappa_{\nu\varphi}(n\pm1)$ being the same sign. Even in this case the energy giving allowed transitions are always $2\pi\gamma/L$ independent of a flux again.

In Fig. 38 $\mathrm{Re}\tilde{\sigma}_{xx}$ (indicated by 'Self-Consistent') and $\mathrm{Re}\sigma_{xx}$ (indicated by 'Perturbation') are shown for a metallic CN with magnetic flux $\varphi=0$, 1/4, and 1/2. The peaks around $2\pi\gamma/L$ correspond to the allowed transitions at $k=0$ discussed above. In the magnetic flux $\varphi=0$, the peak of $\sigma_{xx}$ is suppressed in comparison to the others. This is because of the absence of the divergence in the joint density of states at the band edge. It is quite interesting that these peaks disappear almost completely if the depolarization effect is taken into account. The $\mathrm{Re}\tilde{\sigma}_{xx}$ and $\mathrm{Re}\sigma_{xx}$ of metallic CN's doped with electrons

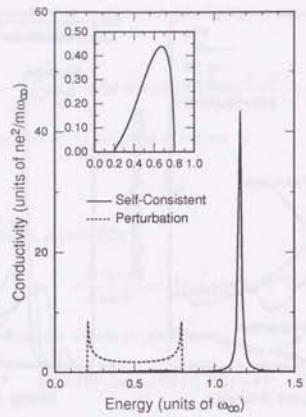


**Fig. 40** Calculated real part of $\tilde{\sigma}_{xx}$ (solid lines) and $\sigma_{xx}$ (dotted line) of a model conductivity.

are shown in Fig. 39. Again the peaks are suppressed almost completely due to the depolarization effect.

To understand the strong suppression of absorption peaks for perpendicular polarization, we consider a simple model in which the real part of conductivity is proportional to a joint density of states of one-dimensional materials and the oscillator strength is constant. The model conductivity is written as

$$\mathrm{Re}\sigma_{xx}(\omega)=\frac{1}{2}\frac{ne^2}{m}\frac{\theta(|\omega|-\omega_1)\theta(\omega_2-|\omega|)}{\sqrt{(|\omega|-\omega_1)(\omega_2-|\omega|)}} \qquad (0<\omega_1<\omega_2), \tag{4.21}$$

where $n$ is the electron density in an unit area and $m$ is the mass of the electron. This conductivity satisfies the intensity sum rule given by

$$\frac{2}{\pi}\int_0^\infty d\omega \mathrm{Re}\sigma_{xx}(\omega)=\frac{ne^2}{m}. \tag{4.22}$$

By the use of the Kramers-Krönig relation, we get the imaginary part of the conductivity



as

$$\mathrm{Im}\sigma_{xx}(\omega)=-\frac{\mathrm{P}}{\pi}\int_{-\infty}^{\infty}d\omega'\frac{\mathrm{Re}\sigma_{xx}(\omega')}{\omega'-\omega}$$
$$=\begin{cases}-\frac{ne^2}{2m}\left(\frac{1}{\sqrt{(\omega-\omega_1)(\omega-\omega_2)}}-\frac{1}{\sqrt{(\omega+\omega_1)(\omega+\omega_2)}}\right) & |\omega|<\omega_1\\ \mathrm{sgn}(\omega)\frac{ne^2}{2m}\frac{1}{\sqrt{(\omega+\omega_1)(\omega+\omega_2)}} & \omega_1\le|\omega|<\omega_2\\ \mathrm{sgn}(\omega)\frac{ne^2}{2m}\left(\frac{1}{\sqrt{(\omega-\omega_1)(\omega-\omega_2)}}+\frac{1}{\sqrt{(\omega+\omega_1)(\omega+\omega_2)}}\right) & |\omega|\ge\omega_2\end{cases} \tag{4.23}$$

As is seen from eq. (4.19) absorption peaks exist at the frequency where $\mathrm{Re}[\tilde{\sigma}_{xx}(\omega)]$ diverges. From eq. (4.16) it is found that an absorption peak occurs at a frequency $\omega_\mathrm{p}$ higher than the absorption edge $\omega_2$. For $\omega_\mathrm{p}\gg\omega_2$, we have

$$\omega_\mathrm{p}^2=\frac{\pi}{L}\frac{4\pi ne^2}{m}\equiv\omega_\infty^2, \tag{4.24}$$

which is nothing but a plasma frequency corresponding to the three-dimensional electron density $\pi n/L$. This is the reason for the strong suppression of absorption peaks for perpendicular polarized field. A example of $\mathrm{Re}\tilde{\sigma}_{xx}$ and $\mathrm{Re}\sigma_{xx}$ is shown for the model conductivity in Fig. 40.

## 4.4 Summary

The absorption spectra of CN's are calculated in the presence of an Aharonov-Bohm flux. The AB effect, which gives rise to the band-gap oscillation between 0 and $2\pi\gamma/L$ with the period of the magnetic flux quantum, can be observed directly by optical absorption for light polarization parallel to the tube axis as the oscillation of absorption peaks. When the polarized light is perpendicular to the axis, the depolarization field almost completely suppresses the optical absorption peaks. These characteristic features are not modified by carrier doping.

# Chapter 5

# Lattice Instability

It is well-known that 1D metallic systems tend to be unstable against lattice distortions. In fact, based on the extended Su-Schrieffer-Heeger (SSH) model,[55,56] the possibility of bond alternation patterns (the so-called Kekulé pattern) has been studied within a simple 1D model[8] and for finite-size tubules.[57,58] The Kekulé structure consists of a network of hexagons with the alternating short and long bonds like in the classical benzene molecule. Although these works predict that the distortion does not alter electronic properties of CN drastically, there remains a considerable disagreement in their estimated energy gaps. On the other hand, the possibility of an out-of-plane distortion was considered also.[9]

In this chapter, a comprehensive study is made on both in-plane and out-of-plane distortions in metallic CN's using both $\mathbf{k}\cdot\mathbf{p}$ and tight-binding approaches.[59] It is shown that two kinds of distortion cannot coexist in general and two different approaches predict amount of distortions in excellent agreement with each other. Further, effects of a magnetic field on lattice distortions are studied. [53,60,61] In the presence of a magnetic field perpendicular to the tube axis, the energy bands turn into flat Landau levels near the K and K' points at the Fermi energy. It gives rise to considerable lowering of the electronic energy.

This section is organized as follows: In Sec. 5.1 the $\mathbf{k}\cdot\mathbf{p}$ Hamiltonian in the presence of in-plane and out-of-plane distortions are obtained. The gap equation is solved analytically and the use of the $\mathbf{k}\cdot\mathbf{p}$ method is justified by comparing with the results given by a tight-binding model. In Sec. 5.2 the effect of a magnetic field perpendicular to the tube axis are studied in the approximation that the gap parameter is uniform. In Sec. 5.3 the spatial variation of the gap parameter is discussed in a magnetic field. A summary is given in Sec. 5.4.

## 5.1 Absence of Perpendicular Magnetic Field

### 5.1.1 Effective-mass approximation

In the presence of electron-phonon interactions, metallic CN's ($\nu=0$), for which the energy bands cross at the K and K' points of the graphite Brillouin zone, are expected





to be unstable against lattice distortions which open an energy gap at the Fermi energy and consequently lower the total energy. In the following, we consider two different kinds of distortions, (i) in-plan lattice distortions which induce the formation of a Kekulé structure and (ii) out-of-plane distortions.

The Kekulé structure illustrated in Fig. 41(b) is a three-sublattice system. The unit-cell area is $3\sqrt{3}a^2/2$ and contains six carbon atoms (three A's and three B's). There are two kinds of bonds and each atom has one large and two small distorted bonds attached to it. One changes its length by $-2u_1$ and another changes by $u_1$, where $u_1$ is positive or negative. In Fig. 41(c) the large ($-2u_1$) and the small ($u_1$) distortion are indicated by the thick and normal lines, respectively.

The area of the Brillouin zone for the distorted lattice is one-third of that of graphite as shown in Fig. 42, where the six corners (i.e. K and K' points) of the original Brillouin zone come to the center ($\Gamma$ point with $\mathbf{k}=0$). When the Kekulé distortion is introduced, a small energy gap proportional to $|u_1|$ appears at the Fermi level due to an interaction between bands at K and K' points crossing at the $\Gamma$ point in the new Brillouin zone. The possibility of this distortion was pointed out within a simple 1D model[8] and studied for finite-size tubules in the absence of an AB flux.[57,58]

For the out-of-plane distortions, the sites A and B move up and down by $\pm u_2$ in the $z$ directions perpendicular to the graphite sheet, which are represented in Fig. 41(c) by open and full circles. The size of the unit cell is unchanged and the site energy of CN's for A and B carbon atoms is shifted by an energy proportional to $u_2$, leading to a gap at K and K' points of the original Brillouin zone. We note that this distortion is possible because of finite curvature of CN's, which breaks the mirror symmetry of the 2D graphite sheet about $z=0$. The possibility of this distortion has been considered in the absence of an AB flux.[9]

In the presence of two kinds of lattice distortions, the $\mathbf{k}\cdot\mathbf{p}$ Hamiltonian is given by the following $4\times4$ matrix

$$\begin{pmatrix} \gamma(\sigma_x k_x+\sigma_y k_y)+\sigma_z\Delta_2 & -\mathrm{i}\sigma_y\Delta_1 \\ \mathrm{i}\sigma_y\Delta_1 & \gamma(\sigma_x k_x-\sigma_y k_y)+\sigma_z\Delta_2 \end{pmatrix} \begin{pmatrix} F_{\mathrm{K}}(\mathbf{r}) \\ F_{\mathrm{K'}}(\mathbf{r}) \end{pmatrix} = \varepsilon \begin{pmatrix} F_{\mathrm{K}}(\mathbf{r}) \\ F_{\mathrm{K'}}(\mathbf{r}) \end{pmatrix}, \tag{5.1}$$

where $\Delta_1$ represents energy corresponding to the in-plane Kekulé distortion and $\Delta_2$ that to the out-of-plane distortion. This Hamiltonian will be derived in a tight-binding model in a following section.

Introducing a three components wave vector $\tilde{\mathbf{k}}=(k_x,k_y,k_z)$ with $k_z=-\Delta_1/\gamma$ and a 4-column vector of envelope functions

$$\psi(\mathbf{r}) = \begin{pmatrix} F^{\mathrm{A}}(\mathbf{r}) \\ F^{\mathrm{B}}(\mathbf{r}) \end{pmatrix}, \tag{5.2}$$

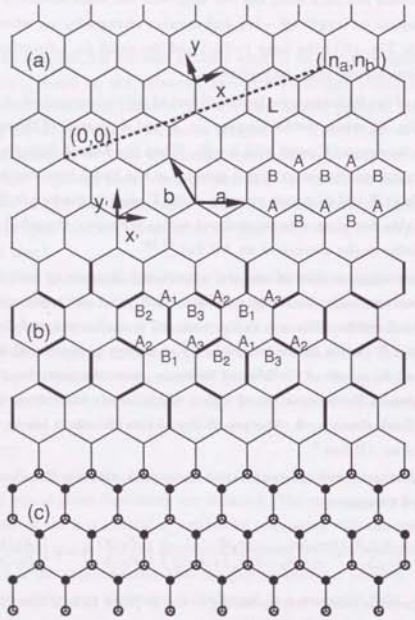


**Fig. 41** A single layer of graphite. (a) The structure of a nanotube is specified by the chiral vector $\mathbf{L}=n_a\mathbf{a}+n_b\mathbf{b}$ with $\mathbf{a}$ and $\mathbf{b}$ being primitive translation vector. There are two kinds of sites A and B. (b) In-plane Kekulé lattice distortion. Thick and normal lines show larger and smaller distorted bonds, respectively. There are six kinds of sites $A_1$, $A_2$, $\cdots$, $B_3$. (c) Out-of-plane lattice distortion. The black-dot atoms shift in the positive $z$ direction and the white-dot ones in the opposite direction.



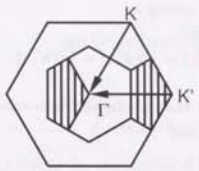


**Fig. 42** The larger hexagon represents the first Brillouin zone of non-deformed lattice. When the in-plane lattice-distortion occurs, the Brillouin zone is reduced to the smaller hexagon.

with

$$F^{\mathrm{A}}(\mathbf{r})=\begin{pmatrix}F^{\mathrm{A}}_{\mathbf{K}}(\mathbf{r})\\ F^{\mathrm{A}}_{\mathbf{K}'}(\mathbf{r})\end{pmatrix} \quad \text{and} \quad F^{\mathrm{B}}(\mathbf{r})=\begin{pmatrix}F^{\mathrm{B}}_{\mathbf{K}'}(\mathbf{r})\\ F^{\mathrm{B}}_{\mathbf{K}}(\mathbf{r})\end{pmatrix}, \tag{5.3}$$

we can rewrite eq. (5.1) into the form of Dirac's relativistic equation

$$\left(\gamma\hat{\alpha}\cdot\hat{\mathbf{k}}+\hat{\beta}\Delta_2\right)\psi=\varepsilon\psi, \tag{5.4}$$

where $\hat{\alpha}_i$ $(i=x,y,z)$ and $\hat{\beta}$ are the $4\times4$ matrices defined as

$$\hat{\alpha}_i=\begin{pmatrix}0 & \sigma_i\\ \sigma_i & 0\end{pmatrix} \quad \text{and} \quad \hat{\beta}=\begin{pmatrix}I_2 & 0\\ 0 & -I_2\end{pmatrix}, \tag{5.5}$$

with $I_2$ being a $2\times2$ identity matrix.

It is well-known that the eigenvalues of Dirac's equation are doubly degenerate and given by

$$\varepsilon^{(\pm)}=\pm\sqrt{\gamma^2\mathbf{k}^2+{\Delta_2}^2}=\pm\sqrt{\gamma^2(k_x^2+k_y^2)+{\Delta_1}^2+{\Delta_2}^2}. \tag{5.6}$$

The energy bands of a metallic carbon nanotube in the presence of the lattice distortions are obtained by putting $k_x=\kappa_\varphi(n)$ and $k_y=k$ in the above solution

$$\varepsilon^{(\pm)}_{\varphi}(n,k,\Delta_1,\Delta_2)=\pm\sqrt{\gamma^2\kappa_\varphi(n)^2+\gamma^2k^2+{\Delta_1}^2+{\Delta_2}^2}. \tag{5.7}$$

When $\varphi=0$, a gap $E_g=2\sqrt{{\Delta_1}^2+{\Delta_2}^2}$ opens up at $k=0$.

### 5.1.2 Gap equations

The gap parameters $\Delta_1$ and $\Delta_2$ are determined by the condition that the total energy is minimum. The total energy consists of the electronic part given in the $\mathbf{k}\cdot\mathbf{p}$

scheme by the contribution coming from the region near the Fermi energy and the lattice or phonon part. The latter can be written as

$$E_p(\Delta_1, \Delta_2) = \frac{1}{2}NK_1u_1^2 + \frac{1}{2}NK_2u_2^2, \tag{5.8}$$

where $K_1$ and $K_2$ are the in-plane and out-of-plane force constants, respectively, $N$ is the total number of carbon atoms, and

$$\Delta_1 = f_1u_1 \quad \text{and} \quad \Delta_2 = f_2u_2, \tag{5.9}$$

with $f_1$ and $f_2$ being appropriate constants. It should be noted that there is no cross term proportional to $u_1u_2$ in (5.8). This can be understood when we consider the fact that the A and B carbon atoms are equivalent even in the presence of the Kekulé structure and therefore the energy under the distortion $+u_2$ should be the same as that under $-u_2$ even for nonvanishing $u_1$.

The total energy is written as

$$E = 4\frac{A}{2\pi}\sum_{n=-\infty}^{\infty}\int_{-\infty}^{\infty}\mathrm{d}k\,\varepsilon_\varphi^{(-)}\,g_0\left(|\varepsilon_\varphi^{(-)}|\right) + N\frac{K_1\Delta_1^2}{2f_1^2} + N\frac{K_2\Delta_2^2}{2f_2^2}, \tag{5.10}$$

where $\varepsilon_\varphi^{(-)}$ is valence-bands energy given by eq. (3.24), a factor 4 comes from the double degeneracy of each energy band and the summation over two spin states, and $g_0(\varepsilon)$ is a cutoff function defined as

$$g_0(\varepsilon) = \frac{\varepsilon_c^{\alpha_c}}{\varepsilon^{\alpha_c} + \varepsilon_c^{\alpha_c}}. \tag{5.11}$$

This cutoff function contains two parameters, $\varepsilon_c$ and $\alpha_c$. The parameter $\varepsilon_c$ represents an energy cut off and should be selected in such a way that the effective-mass approximation is valid for the energy range given by $|\varepsilon| \lesssim \varepsilon_c$. The parameter $\alpha_c$ determines the way of cutoff. For small $\alpha_c$ the cutoff function decreases slowly, while for large $\alpha_c$ it approaches a step function. As will be shown later, the results are independent of the choice of $\alpha_c$ and $\varepsilon_c$ as long as $\varepsilon_c$ is sufficiently large.

Minimizing the total energy with respect to $\Delta_1$ and $\Delta_2$ we obtain a system of self-consistent gap equations

$$\begin{aligned} 0 &= -4\frac{A}{2\pi}\Delta_1\sum_{n=-\infty}^{\infty}\int_{-\infty}^{\infty}\mathrm{d}k\,\frac{g_1\left(|\varepsilon_\varphi^{(-)}(n,k,\Delta_1,\Delta_2)|\right)}{|\varepsilon_\varphi^{(-)}(n,k,\Delta_1,\Delta_2)|} + N\frac{K_1\Delta_1}{f_1^2}, \\ 0 &= -4\frac{A}{2\pi}\Delta_2\sum_{n=-\infty}^{\infty}\int_{-\infty}^{\infty}\mathrm{d}k\,\frac{g_1\left(|\varepsilon_\varphi^{(-)}(n,k,\Delta_1,\Delta_2)|\right)}{|\varepsilon_\varphi^{(-)}(n,k,\Delta_1,\Delta_2)|} + N\frac{K_2\Delta_2}{f_2^2}, \end{aligned} \tag{5.12}$$



where $g_1(\varepsilon)$ is a new cutoff function given by

$$g_1(\varepsilon) = g_0(\varepsilon) + \varepsilon\frac{\partial g_0(\varepsilon)}{\partial\varepsilon}, \tag{5.13}$$

which satisfies

$$\int_0^\infty \mathrm{d}\varepsilon\, g_1(\varepsilon) = 0. \tag{5.14}$$

This plays an important role in the elimination of the cut-off parameters $\varepsilon_c$ and $\alpha_c$, as will be shown later.

It is straightforward to show that the gap equations (5.12) have a non-trivial solution (1) $\Delta_1 > 0$ and $\Delta_2 = 0$ and (2) $\Delta_1 = 0$ and $\Delta_2 > 0$ and that the total energy takes an absolute minimum at (1) when $K_1/f_1^2 < K_2/f_2^2$ and at (2) when $K_1/f_1^2 > K_2/f_2^2$. In the case (1) only an in-plane distortion can exist, while only an out-of-plane occurs in the case (2). Only exception is the special case $K_1/f_1^2 = K_2/f_2^2$, for which the energy is degenerate along a circle given by $\Delta_1^2+\Delta_2^2=\Delta^2$. In the following, we shall consider only one kind of distortion and put $\Delta=\Delta_i$, $f=f_i$, and $K=K_i$ $(i=1,2)$.

Because a unit cell of a 2D graphite with area $\sqrt{3}a^2/2$ contains two carbon atoms, the total number of site is calculated as $N=4AL/\sqrt{3}a^2$. The gap equation is written as

$$\Delta = \Delta\frac{\lambda_L}{2}I(\varphi,\Delta), \tag{5.15}$$

with

$$I(\varphi,\Delta) = \gamma\sum_{n=-\infty}^{\infty}\int_{-\infty}^{\infty}\mathrm{d}k\,\frac{g_1\left(|\varepsilon_\varphi^{(-)}(n,k,\Delta)|\right)}{|\varepsilon_\varphi^{(-)}(n,k,\Delta)|}, \tag{5.16}$$

and

$$\varepsilon_\varphi^{(\pm)}(n,k,\Delta) = \pm\sqrt{\gamma^2\kappa_\varphi(n)^2+\gamma^2k^2+\Delta^2}, \tag{5.17}$$

where $\lambda_L$ is the $L$ dependent effective coupling constant given by

$$\lambda_L = \lambda\frac{a}{L}, \tag{5.18}$$

with

$$\lambda = \frac{\sqrt{3}af^2}{\pi K\gamma}, \tag{5.19}$$

which is the coupling constant for a 2D graphite.

The gap will appear only when the original gap in the absence of lattice distortion is small, i.e. only when $\varphi$ is close to an integer. Because all the quantities are periodic

in $\varphi$, we shall limit ourselves to the case $|\varphi| \ll 1$. As is described in Appendix B, an analytic expression for $I(\varphi, \Delta)$ is obtained for sufficiently large cutoff $\varepsilon_c$ as

$$I(\varphi, \Delta) = -\ln\left[\varphi^2 + \left(\frac{L}{2\pi\gamma}\Delta\right)^2\right] - 2\ln 2 - 2 - 2C. \tag{5.20}$$

with a constant $C$ given by

$$C = \sum_{l=1}^{\infty} \frac{\zeta(2l)}{l(2l+1)2^{2l}} \approx 0.1445972, \tag{5.21}$$

where $\zeta(p)$ is Riemann's zeta-function defined as

$$\zeta(z) = \sum_{n=1}^{\infty} \frac{1}{n^z}. \tag{5.22}$$

Combining eqs. (5.15) and (5.20), we find a quite simple analytic expression for the gap $E_g(\varphi) = 2\Delta(\varphi)$,

$$E_g(\varphi) = E_g\sqrt{1 - \left(\frac{\varphi}{\varphi_c}\right)^2}, \tag{5.23}$$

where $E_g = 2\Delta(0)$ is the gap in the absence of a magnetic flux, given by

$$E_g = \frac{2\pi\gamma}{L}\exp\left(-\frac{L}{a\lambda} - 1 - C\right), \tag{5.24}$$

and the critical flux $\varphi_c$ is given by

$$\varphi_c = \frac{\phi_c}{\phi_0} = \frac{LE_g}{4\pi\gamma}. \tag{5.25}$$

The energy gap is a monotone decreasing function of the circumference $L/a$. As will be discussed later in this chapter, the coupling constant $\lambda$ for the Kekulé distortion is not much larger than unity and that for the out-of-plane distortion decreases rapidly with increasing circumference length. Therefore, it is safe to conclude that the lattice distortion is not important for metallic CN's with large tubule diameter.

### 5.1.3 Tight-binding model

We introduce $\psi_z(\mathbf{r})$ of the wave function which is a normalized $p_z$ orbital for an isolated carbon atom. For simplicity we shall neglect the overlapping of the wave functions for different atoms. In the tight-binding approximation the usual basis set is $\{\psi_{\eta\mathbf{k}}\}$ where $\eta = A_1, A_2, A_3, B_1, B_2, B_3$, with

$$\psi_{\eta\mathbf{k}}(\mathbf{r}) = \sqrt{\frac{6}{N}}\sum_{\mathbf{R}_\eta} \exp(i\mathbf{k}\cdot\mathbf{R}_\eta)\Phi_{\mathbf{R}_\eta}(\mathbf{r}), \tag{5.26}$$



where $\mathbf{R}_\eta$ is the position of the $\eta$-th kind of carbon atoms.

In the SSH model the transfer integral for bond with larger and smaller length changes from $-\gamma_0$ into $p$ and $q$, respectively, with

$$p = -\gamma_0 - 2\alpha u_1 \quad \text{and} \quad q = -\gamma_0 + \alpha u_1, \tag{5.27}$$

where $\alpha$ being the electron-phonon coupling constant. The Hamiltonian matrix is obtained as

$$\begin{array}{c} \\ A_1 \\ A_2 \\ A_3 \\ B_1 \\ B_2 \\ B_3 \end{array}\!\!\begin{array}{c} \begin{array}{cccccc} A_1 & A_2 & A_3 & B_1 & B_2 & B_3 \end{array} \\ \begin{pmatrix} 0 & 0 & 0 & pe^{-i\vec{r}_1\cdot\mathbf{k}} & qe^{-i\vec{r}_3\cdot\mathbf{k}} & qe^{-i\vec{r}_2\cdot\mathbf{k}} \\ 0 & 0 & 0 & qe^{-i\vec{r}_2\cdot\mathbf{k}} & qe^{-i\vec{r}_1\cdot\mathbf{k}} & pe^{-i\vec{r}_3\cdot\mathbf{k}} \\ 0 & 0 & 0 & qe^{-i\vec{r}_3\cdot\mathbf{k}} & pe^{-i\vec{r}_2\cdot\mathbf{k}} & qe^{-i\vec{r}_1\cdot\mathbf{k}} \\ pe^{i\vec{r}_1\cdot\mathbf{k}} & qe^{i\vec{r}_2\cdot\mathbf{k}} & qe^{i\vec{r}_3\cdot\mathbf{k}} & 0 & 0 & 0 \\ qe^{i\vec{r}_3\cdot\mathbf{k}} & pe^{i\vec{r}_3\cdot\mathbf{k}} & qe^{i\vec{r}_1\cdot\mathbf{k}} & 0 & 0 & 0 \\ qe^{i\vec{r}_2\cdot\mathbf{k}} & pe^{i\vec{r}_3\cdot\mathbf{k}} & qe^{i\vec{r}_1\cdot\mathbf{k}} & 0 & 0 & 0 \end{pmatrix} \end{array}, \tag{5.28}$$

where $\vec{r}_1, \vec{r}_2$, and $\vec{r}_3$ are shown in Fig. 11 and given in eq. (3.51).

Introduce the following unitary matrix:

$$\frac{1}{\sqrt{3}}\begin{array}{c} \begin{array}{cccccc} \Gamma_A & \Gamma_B & K_A & K_B & K'_A & K'_B \end{array} \\ \begin{pmatrix} 1 & 0 & 1 & 0 & 1 & 0 \\ 1 & 0 & \omega & 0 & \omega^2 & 0 \\ 1 & 0 & \omega^2 & 0 & \omega & 0 \\ 0 & 1 & 0 & -1 & 0 & 1 \\ 0 & 1 & 0 & -\omega & 0 & \omega^2 \\ 0 & 1 & 0 & -\omega^2 & 0 & \omega \end{pmatrix} \end{array}, \tag{5.29}$$

with $\omega = \exp(2\pi i/3)$. The column vectors denoted as $K_A$, $K_B$, $K'_A$, and $K'_B$ are the eigenvectors at K and K' points in a 2D graphite sheet. The bonding state formed by $\Gamma_A$ and $\Gamma_B$ corresponds to the bottom of the valence band at the $\Gamma$ point in the unperturbed Brillouin zone and the anti-bonding state to the top of the conduction band. For this basis set the Hamiltonian is rewritten as

$$\begin{array}{c} \\ \Gamma_A \\ \Gamma_B \\ K_A \\ K_B \\ K'_A \\ K'_B \end{array}\!\!\begin{array}{c} \begin{array}{cccccc} \Gamma_A & \Gamma_B & K_A & K_B & K'_A & K'_B \end{array} \\ \begin{pmatrix} 0 & -\gamma_0 R & 0 & \alpha u_1 T & 0 & -\alpha u_1 S \\ -\gamma_0 R^* & 0 & -\alpha u_1 T^* & 0 & -\alpha u_1 S^* & 0 \\ 0 & -\alpha u_1 T & 0 & \gamma_0 S & 0 & -\alpha u_1 R \\ \alpha u_1 T^* & 0 & \gamma_0 S^* & 0 & \alpha u_1 R^* & 0 \\ 0 & -\alpha u_1 S & 0 & \alpha u_1 R & 0 & -\gamma_0 T \\ -\alpha u_1 S^* & 0 & -\alpha u_1 R^* & 0 & -\gamma_0 T^* & 0 \end{pmatrix} \end{array}, \tag{5.30}$$

with

$$R = \exp(-i\vec{r}_1\cdot\mathbf{k})+\exp(-i\vec{r}_2\cdot\mathbf{k})+\exp(-i\vec{r}_3\cdot\mathbf{k}),$$
$$S = \exp(-i\vec{r}_1\cdot\mathbf{k})+\exp(-i\vec{r}_2\cdot\mathbf{k}-2\pi i/3)+\exp(-i\vec{r}_3\cdot\mathbf{k}+2\pi i/3), \quad (5.31)$$
$$T = \exp(-i\vec{r}_1\cdot\mathbf{k})+\exp(-i\vec{r}_2\cdot\mathbf{k}+2\pi i/3)+\exp(-i\vec{r}_3\cdot\mathbf{k}-2\pi i/3).$$

The $4\times4$ sub-matrix with respect to K and K' points is reduced to the $\mathbf{k}\cdot\mathbf{p}$ Hamiltonian (5.1), if being expanded up to the first power in $k$. We have the relation: $\gamma = \sqrt{3}a\gamma_0/2$, $\Delta_1 = 3\alpha u_1$, and $f_1 = 3\alpha$. It is almost evident that $\pm\Delta_2$ represents a shift in the local site energy of A and B carbon atoms due to the distortion in the $z$ direction. A self-consistent band structure calculation is necessary for the determination of $f_2$ giving a relation between $\Delta_2$ and displacement $u_2$, which is out of the scope of the present paper. Therefore, we shall exclusively consider the in-plane Kekulé distortion and put $u=u_1$ in the following.

The elastic energy is written as

$$E_p = \frac{K_0}{6}\sum_{<ij>} u_{ij}^2, \quad (5.32)$$

where $u_{ij}$ is the length displacement of the bond between $i$-th and $j$-th atoms and the sum is taken over nearest-neighbor pairs of $<ij>$. Since the number of larger distorted bonds is $1/3$ of the total bonds $3N/2$ and that of smaller distorted one is $2/3$ of $3N/2$, we get

$$E_p = \frac{K_0}{6}\frac{3N}{2}\left[\frac{1}{3}(2u)^2+\frac{2}{3}u^2\right] = \frac{1}{2}NK_0u^2. \quad (5.33)$$

It should be noted that this force constant $K_0$ is different from $K=K_1$ introduced in eq. (5.8) in the $\mathbf{k}\cdot\mathbf{p}$ scheme. There is an ambiguity in separation of the total-energy shift due to lattice distortion into the electronic part and the lattice part. In the $\mathbf{k}\cdot\mathbf{p}$ scheme, the electronic part consists only of the contribution in the vicinity of the Fermi level, where 1D nature of CN's plays a decisive role. In the present SSH model, on the other hand, an appreciable contribution comes from energy shifts of the whole occupied valence bands. This contribution exists also in a 2D graphite sheet and can be written as $(1/2)NK_eu^2$ with an appropriate force constant $K_e$. In the $\mathbf{k}\cdot\mathbf{p}$ scheme, $K_e$ should be added to the force constant and we have

$$K = K_0 + K_e. \quad (5.34)$$

The force constant $K_e$ due to the occupied valence bands in 2D graphite can be calculated in the second order perturbation theory within the present tight-binding model. The result is $K_e = -5.81\alpha^2/\gamma_0$. Details are given in Appendix C.



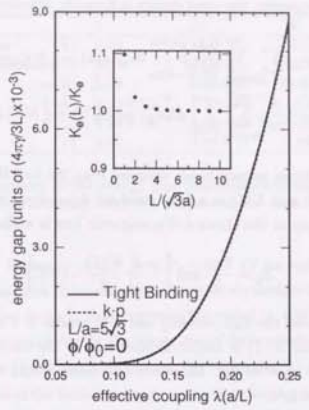


**Fig. 43** The energy gap calculated in the tight-binding model of CN's having circumference $L=5\sqrt{3}a$ as a function of the coupling constant $\lambda$ (the solid line) and analytic result obtained in the effective-mass scheme (the dotted line). The inset shows the calculated force constant $K_e(L)$ of CN's as a function of the circumference.

The electronic states of nanotubes are obtained from eq. (5.28) by the replacement of wave vector in the circumference direction by discrete one given by eq. (3.23). Because the electronic states are mainly determined by the sum $n_a+n_b$, we shall confine ourselves to the non-chiral armchair structure with chiral vector $\mathbf{L} = (2m, m)a$ with integer $m$ from now on. We have $k_x = (2\pi/L)n$ with $n = 1, \ldots, 2m$. The first Brillouin zone is given by $-\pi/3a \le k_y < \pi/3a$. It is straightforward to calculate the total energy by summing up energy of all occupied bands and determine gap $\Delta$ by a minimization. The resulting gap for $m=5$ corresponding to $L/a=5\sqrt{3}$ is shown as a function of the effective coupling constant $\lambda(a/L)$ in Fig. 43. The analytic result obtained in the effective-mass approximation is in excellent agreement with that of a tight-binding method even for such a narrow tubule.

Because the contribution to the total energy shift due to lattice distortion is proportional to $u^2$ except in the vicinity of the top of the highest valence band where the $\mathbf{k}\cdot\mathbf{p}$

description is quite accurate, the total energy is formally rewritten as

$$E = \sum_{v=1,2,3}\sum_{n=1}^{2m}\frac{2A}{2\pi}\int_{-\pi/3a}^{\pi/3a} \mathrm{d}k_y\, \varepsilon_v(\mathbf{k}) + \frac{1}{2}NK_0u^2$$
$$= 4\frac{A}{2\pi}\sum_{n=-\infty}^{\infty}\int_{-\infty}^{\infty} \mathrm{d}k\, \varepsilon_\varphi^{(-)} g_0(|\varepsilon_\varphi^{(-)}|) + \frac{1}{2}NK(L)u^2, \tag{5.35}$$

where $v = 1, 2, 3$ are three valence bands obtained from the 6×6 Hamiltonian (5.28), $\varepsilon_\varphi^{(-)}$ is given by eq. (5.17), and $K(L)$ is a force constant depending on the circumference. In terms of $K(L)$, the gap in the absence of a magnetic flux is written as

$$E_g = \frac{2\pi\gamma}{L}\exp\left[-\frac{L}{a\lambda}\frac{K(L)}{K} - 1 - C\right]. \tag{5.36}$$

The agreement between the tight-binding and $\mathbf{k}\cdot\mathbf{p}$ results is a direct result of the fact that the force constant $K(L)$ is almost independent of the circumference $L/a$. This is demonstrated in the inset to Fig. 43, where calculated $K_v(L) \equiv K(L) - K_0$ is plotted against circumference $L/a$.

### 5.1.4 Comparison with other studies

Quantitative discussion is possible for the in-plane Kekulé distortion, because parameters are known without performing self-consistent band-structure calculation. Following Harigaya,[62] we shall use the parameters appropriate for $C_{60}$:

$$\gamma_0 = 2.5 \text{ eV}, \quad \alpha = f_1/3 = 6.31 \text{ eV/Å}, \quad \text{and} \quad K_0 = 3\times 49.7 \text{ eV/Å}^2.$$

Note that present $K_0$ is three times as large as $K_0$ used by Harigaya and coworkers[57,58] due to the difference of definition but gives the same value of force constant. For these parameters, we have $K_v = -92.6$ eV/Å$^2$ and $K = 56.5$ eV/Å$^2$. Thus the dimensionless coupling constant is $\lambda \approx 1.62$. Table 4 gives some examples for $E_g$, $u$, $\varphi_c$, and critical magnetic field $H_c$ for armchair tubules $\mathbf{L}/a = (2m, m)$ with $m = 5$, 10, and 20. It shows that even for a narrow tubule with $m = 5$ effects of the lattice distortion are quite small and that a small magnetic flux easily destroys the distortion.

Harigaya and Fujita[58] obtained $E_g \approx 4.4\times10^{-3}$ eV and $u \approx 5.6\times10^{-4}$ Å for an armchair nanotube with $m = 5$ from the extrapolation of the results for finite tubes to infinitely long one. The present values given in Table I are slightly smaller but in the same order of magnitude as this result. This disagreement is partly due to the fact that Harigaya and Fujita allowed distortion different from the pure Kekulé type and partly due to an ambiguity in their extrapolation to an infinitely long nanotube. It is expected that deviations from the pure Kekulé pattern become less important with the increase



| $m$ | | 5 | 10 | 20 |
|---|---|---|---|---|
| Diameter | (Å) | 6.78 | 13.6 | 27.1 |
| Circumference | (Å) | 21.3 | 42.6 | 85.2 |
| $E_g$ | (meV) | 2.38 | $5.68\times10^{-3}$ | $6.46\times10^{-8}$ |
| $u$ | (Å) | $6.29\times10^{-5}$ | $1.50\times10^{-7}$ | $1.71\times10^{-12}$ |
| $\varphi_c$ | | $7.58\times10^{-4}$ | $3.62\times10^{-6}$ | $8.23\times10^{-11}$ |
| $H_c$ | (T) | 8.67 | $1.04\times10^{-2}$ | $5.89\times10^{-8}$ |

**Table 4** Some examples of the energy gap, bond-length change, critical flux, and corresponding critical magnetic field $H_c$, calculated for armchair nanotubes with chiral vector $\mathbf{L}/a = (2m, m)$.

of the circumference. Mintmire *et al.*[8] gave $E_g < 10^{-4}$ eV for nanotubes with the same circumference, which is more than one order of magnitude smaller than the present result. This is presumably due to their inappropriate 1D model in which the gap is given by $E_g = 4\alpha u$ instead of $6\alpha u$ and due to the wrong use of force constant $K_0$ instead of $K$.

In the case of the out-of-plane distortion, the coefficient $f_2$ defined in eq. (5.9) becomes nonzero because of the finite curvature and is therefore expected to be proportional to $a/L$. Thus, the coupling constant $\lambda$ is proportional to $(a/L)^2$, leading to $\lambda_L \propto (a/L)^3$, and the gap decreases very rapidly with the diameter as $\exp[-(L/a)^3]$. This is quite in contrast to the result of Saito *et al.*[9] that the distortion approaches that of a 2D graphite with increasing $L$.

## 5.2 Effects of Perpendicular Magnetic Field

A magnetic field perpendicular to the tube axis modifies the energy bands considerably. In high magnetic fields where the magnetic length $l \equiv \sqrt{ch/eH}$ is much smaller than the circumference, well-defined Landau levels can be formed. Figure 44 gives some examples of the lowest conduction band and the highest valence band calculated numerically, which become almost independent of $k$ up to a certain critical wave vector $k_H$ estimated in eq. (3.40). Correspondingly, the density of states near the Fermi level is drastically enhanced from the value $2/\pi\gamma L$ in the absence of a magnetic field, as is shown in Fig. 45. It causes the increase of instability against lattice distortions considerably. It should be noted that the energy levels become almost independent of $\varphi$ and also of whether CN's are metals or semiconductors.

First we assume that lattice distortions are independent of the position to understand the effects of magnetic field on lattice distortions briefly in this section. Effects of spatial variation of distortions will be included in the next section.

### 5.2.1 Gap equations

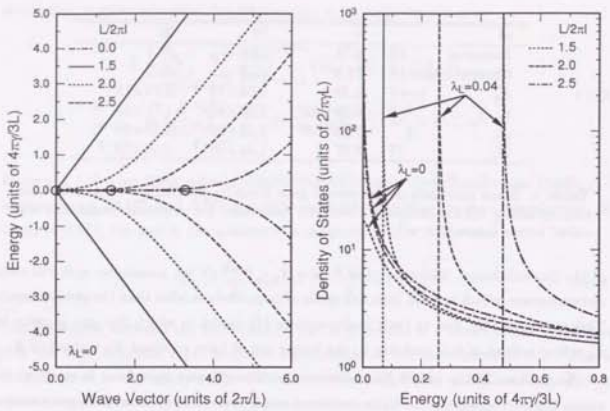


**Fig. 44** (Left) Calculated highest valence band and lowest conduction band of a metallic CN for various magnetic fields perpendicular to the tube axis. The critical wave vector $k_H$ given by eq. (3.40) is denoted by open circles.

**Fig. 45** (Right) Calculated density of states in the vicinity of the Fermi level for a metallic CN in magnetic field perpendicular to the tube axis. The density of states in the presence of a lattice distortion with a gap for $\lambda_L = 0.04$ is also shown. The density of states in the absence of a field and lattice distortion is given by $2/\pi\gamma L$.

Let $\mathbf{F}_{nk}(\mathbf{r})$ be the eigen function of the $n$th conduction band with wave vector $k$ in the $y$ direction associated with the K point in the absence of a lattice distortion, i.e.,

$$\gamma(\sigma_x\hat{k}_x+\sigma_y\hat{k}_y)\mathbf{F}_{nk}(\mathbf{r}) = \varepsilon^{(0)}_{\varphi H}(n,k)\mathbf{F}_{nk}(\mathbf{r}). \tag{5.37}$$

Then, it is easy to show that $\sigma_x\mathbf{F}_{nk}(\mathbf{r})$ is the eigenvector of the valence band with energy $-\varepsilon^{(0)}_{\varphi H}(n,k)$. Further, $\sigma_x\mathbf{F}_{nk}(\mathbf{r})$ and $\sigma_z\sigma_x\mathbf{F}_{nk}(\mathbf{r})$ are the eigenvectors of the conduction band with energy $\varepsilon^{(0)}_{\varphi H}(n,k)$ and valence band with $-\varepsilon^{(0)}_{\varphi H}(n,k)$, respectively, of the K' point. The orthonormality conditions are written as

$$\begin{aligned}\int \mathrm{d}\mathbf{r}\ \mathbf{F}_{nk}(\mathbf{r})^+\mathbf{F}_{n'k'}(\mathbf{r}) &= \delta_{nn'}\delta_{kk'},\\ \int \mathrm{d}\mathbf{r}\ \mathbf{F}_{nk}(\mathbf{r})^+\sigma_x\mathbf{F}_{n'k'}(\mathbf{r}) &= 0,\end{aligned} \tag{5.38}$$

where the former represents the condition among conduction bands and the latter that between conduction and valence bands.



In the presence of the lattice distortion, the Hamiltonian in eq. (5.1) has a nonvanishing matrix element among states $\{\mathbf{F}_{nk}, \sigma_x\mathbf{F}_{nk}\}$ of a K point and $\{\sigma_x\mathbf{F}_{nk}, \sigma_z\sigma_x\mathbf{F}_{nk}\}$ of a K' point. Within these bases the Hamiltonian is written as

$$\mathcal{H}_{nn'}(k) = \begin{array}{c} \\ K \\ K' \end{array}\begin{array}{c} \begin{array}{cc} K & K' \end{array} \\ \begin{pmatrix} \varepsilon^{(0)}_{\varphi H}(n,k)\sigma_z+\Delta_2\sigma_x & -\Delta_1\sigma_x \\ -\Delta_1\sigma_x & \varepsilon^{(0)}_{\varphi H}(n,k)\sigma_z-\Delta_2\sigma_x \end{pmatrix} \end{array}\delta_{nn'}. \tag{5.39}$$

Thus, the energy can be obtained by the diagonalization of the 4×4 matrix as

$$\varepsilon^{(\pm)}_{\varphi H}(n,k) = \pm\sqrt{\varepsilon^{(0)}_{\varphi H}(n,k)^2+\Delta_1^2+\Delta_2^2}, \tag{5.40}$$

where upper sign (+) and lower sign (−) correspond to conduction and valence bands, respectively. The lattice distortion opens an energy gap $2\sqrt{\Delta_1^2+\Delta_2^2}$.

The gap equations in the presence of perpendicular field are given by just replacement $\varepsilon^{(-)}_{\varphi}(n,k,\Delta_1,\Delta_2)$ in eq. (5.12) by $\varepsilon^{(-)}_{\varphi}(n,k,H,\Delta_1,\Delta_2)$ and one of the in-plane and out-of-plane distortions occurs in the same condition with that described below eq. (5.14). In the following we shall consider only one kind of distortion and put $\Delta=\Delta_i$, $f=f_i$, and $K=K_i$ $(i=1,2)$.

### 5.2.2 High magnetic field

In high magnetic fields where the magnetic length is much smaller than the circumference, $L/2\pi l \gg 1$, Landau states with no dispersion are formed at the Fermi level and their contribution to the band-energy shift becomes dominant in the weak-coupling limit $(\lambda_L \to 0)$. Therefore, the total energy is approximately given by

$$E \approx -4\frac{A}{2\pi}2\Delta k_H + N\frac{K\Delta^2}{2f^2}, \tag{5.41}$$

where $Lk_H/2\pi \approx (L/2\pi l)^2$. The minimization of this gives the energy gap

$$E_g = 2\Delta \approx 2\lambda_L\gamma k_H = \frac{\lambda}{\pi}\frac{a\gamma}{l^2}. \tag{5.42}$$

In the case of a 2D graphite sheet, a single nondegenerate Landau level is formed at the Fermi level for K and K' points in magnetic fields. These Landau levels are split into $\pm|\Delta|$ in the presence of a lattice distortion. Because the number of states with energy $-|\Delta|$ is $AL/2\pi l^2$ with $AL$ being the area of the graphite sheet, the total energy is given by

$$E = -2\frac{LA}{2\pi l^2}\Delta + N\frac{K\Delta^2}{2f^2}, \tag{5.43}$$

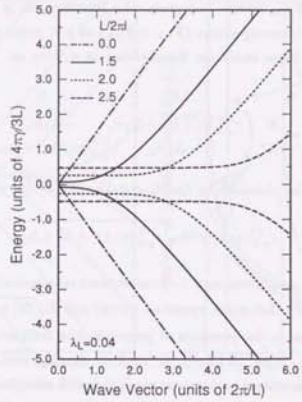


**Fig. 46** The highest valence band and lowest conduction band of a metallic CN for various magnetic fields perpendicular to the tube axis in the presence of a lattice distortion.

where the factor 2 represents the double degeneracy of spin. Thus the energy gap is obtained as

$$E_g = 2\Delta = \frac{\lambda}{2}\frac{a\gamma}{l^2}. \tag{5.44}$$

The result is $\pi/2$ times as large as that given by eq. (5.42). In nanotubes the effective magnetic field is given by its component $H\cos\theta$ perpendicular to the cylinder surface. Therefore, the number of states is reduced from that of a 2D graphite sheet by $\langle|\cos\theta|\rangle = 2/\pi$, where $\langle\cdots\rangle$ is an average over $\theta$. This explains the difference between a 2D graphite sheet and nanotubes with infinitely large circumference.

### 5.2.3 Numerical results

Figure 46 shows the highest valence band and lowest conduction band as a function of $k$. The corresponding density of states are given in Fig. 45.

Figure 47 gives the numerical results in CN's with $L=\sqrt{3}ma$ (armchair nanotubes) for coupling constant $\lambda = 1.62$ corresponding to the in-plain Kekulé distortion. Use has been made of $a = 2.46$ Å and $\gamma = 5.33$ eV·Å ($\gamma_0 = 2.5$eV). For $\varphi = 0$, the gap parameter increases from the value given by (5.24) monotonically with the increase of a magnetic field. For $\varphi = 1/2$ a gap parameter becomes nonzero suddenly at a certain critical magnetic field and rapidly approaches the parameter for $\varphi = 0$ with the increase of the



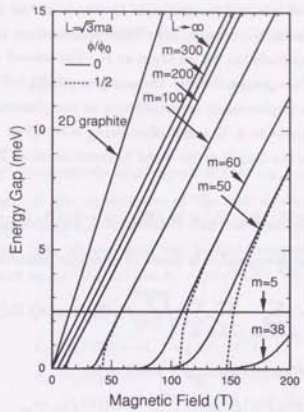


**Fig. 47** Calculated energy gap as a function of a magnetic field perpendicular to the tube axis for metallic CN's with various circumferences. The solid lines represent the gaps for $\varphi = 0$ and the dashed lines those for $\varphi = 1/2$. The results in the limit $L \to \infty$ and for a 2D graphite are also included.

field. In high magnetic fields the gap parameter increases almost in proportion to the field and approaches the value for infinite $L$, *i.e.* eq. (5.42), with the increase of $m$. It is concluded that a strong magnetic field can induce a sizable amount of lattice distortions in metallic carbon nanotubes though it may be exponentially small in the absence of a field.

## 5.3 Position-Dependent Distortion

For CN's the effective magnetic field depends on the position in the circumference direction as $H\cos\theta$ and the magnetic length changes as $l/\sqrt{|\cos\theta|}$. Since the lowering of the electronic energy comes mainly from the Landau states at the Fermi energy, the magnitude of distortions also depends on the position. In this section we shall study the spatial variation of distortions in a perpendicular magnetic field.

### 5.3.1 Effective-mass Hamiltonian

We should note first that the Kekulé distortion corresponds to the phonon mode of a 2D graphite sheet at the K and K' points having the highest energy. The displacement corresponding the phonon at the K' point is written as

$$\mathbf{u}_i(\mathbf{R}_i) = u_{\mathbf{R}_i}\mathbf{e}_i \exp(i\mathbf{K}'\cdot\mathbf{R}_i) + \text{c.c.} \tag{5.45}$$

where $i$ denotes A or B site and $\mathbf{e}_i$ represents the eigenvectors of the phonon mode at the K' point ($\mathbf{k}=\mathbf{K}'$ with $\mathbf{K}'=(4\pi/3a,0)$). We shall introduce a slowly varying spatial dependence in the amplitude $u_{\mathbf{R}}$ for an atom at $\mathbf{R}$. The second term 'c.c.' in the right hand side of the above equation denotes the complex conjugate of the first term. This actually describes the displacement corresponding to the phonon mode at the K point, because $-\mathbf{K}'$ corresponds to a K point after being subtracted by a reciprocal lattice vector. The change in the length of the bond between atom at $\mathbf{R}_{\mathrm{A}}$ and that at $\mathbf{R}_{\mathrm{A}}-\vec{r}_l$ is written as

$$u(\mathbf{R}_{\mathrm{A}},\mathbf{R}_{\mathrm{A}}-\vec{r}_l)=[\mathbf{u}_{\mathrm{B}}(\mathbf{R}_{\mathrm{A}}-\vec{r}_l)-\mathbf{u}_{\mathrm{A}}(\mathbf{R}_{\mathrm{A}})]\cdot\frac{\vec{r}_l}{|\vec{r}_l|}. \tag{5.46}$$

The wave function is expanded in terms of envelope functions as

$$\psi(\mathbf{r})=\sum_{\mathbf{G}=\mathbf{K},\mathbf{K}'}\sum_{i=\mathrm{A},\mathrm{B}}\sum_{\mathbf{R}_i}\sqrt{\frac{1}{2N_i}}F^i_{\mathbf{G}}(\mathbf{R}_i)\exp[\mathrm{i}\mathbf{G}\cdot\mathbf{R}_i]\Phi_{\mathbf{R}_i}(\mathbf{r}). \tag{5.47}$$

In the SSH model the transfer integral is given by

$$\int \mathrm{d}\mathbf{r}\Phi^*_{\mathbf{R}_{\mathrm{A}}}(\mathbf{r})\mathcal{H}\Phi_{\mathbf{R}_{\mathrm{A}}-\vec{r}_l}(\mathbf{r})=-\gamma_0-\alpha u(\mathbf{R}_{\mathrm{A}},\mathbf{R}_{\mathrm{A}}-\vec{r}_l). \tag{5.48}$$

Multiplying the Schrödinger equation from left-hand side by $\Phi^*_{\mathbf{R}_{\mathrm{A}}}(\mathbf{r})$, integrating it over $\mathbf{r}$, and multiplying it by $\exp(-\mathrm{i}\mathbf{K}\cdot\mathbf{R}_{\mathrm{A}})$, we have the following difference equation.

$$\begin{aligned}
&\sum_{l=1,2,3}\Big[-\gamma_0\mathrm{e}^{-\mathrm{i}\mathbf{K}\cdot\vec{r}_l}F^{\mathrm{B}}_{\mathbf{K}}(\mathbf{R}_{\mathrm{A}}-\vec{r}_l)-\alpha\big(\mathrm{e}^{\mathrm{i}\mathbf{K}'\cdot\vec{r}_l}u_{\mathbf{R}_{\mathrm{A}}-\vec{r}_l}\mathbf{e}_{\mathrm{B}}-\mathrm{e}^{\mathrm{i}\mathbf{K}\cdot\vec{r}_l}u_{\mathbf{R}_{\mathrm{A}}}\mathbf{e}_{\mathrm{A}}\big)\cdot\frac{\vec{r}_l}{|\vec{r}_l|}F^{\mathrm{B}}_{\mathbf{K}'}(\mathbf{R}_{\mathrm{A}}-\vec{r}_l)\Big]\\
&\quad-\gamma_0\sum_{l=1,2,3}\mathrm{e}^{\mathrm{i}\mathbf{K}\cdot\mathbf{R}_{\mathrm{A}}}\mathrm{e}^{-\mathrm{i}\mathbf{K}'\vec{r}_l}F^{\mathrm{B}}_{\mathbf{K}'}(\mathbf{R}_{\mathrm{A}}-\vec{r}_l)\\
&\quad-\alpha\sum_{l=1,2,3}\mathrm{e}^{\mathrm{i}\mathbf{K}\cdot\mathbf{R}_{\mathrm{A}}}\Big[\mathrm{e}^{\mathrm{i}\mathbf{K}\cdot\vec{r}_l}u^*_{\mathbf{R}_{\mathrm{A}}-\vec{r}_l}\mathbf{e}_{\mathrm{B}}-\mathrm{e}^{\mathrm{i}\mathbf{K}'\cdot\vec{r}_l}u^*_{\mathbf{R}_{\mathrm{A}}}\mathbf{e}_{\mathrm{A}}\Big]\cdot\frac{\vec{r}_l}{|\vec{r}_l|}F^{\mathrm{B}}_{\mathbf{K}}(\mathbf{R}_{\mathrm{A}}-\vec{r}_l)\\
&\quad-\alpha\sum_{l=1,2,3}\mathrm{e}^{\mathrm{i}\mathbf{K}'\cdot\mathbf{R}_{\mathrm{A}}}\Big[u_{\mathbf{R}_{\mathrm{A}}-\vec{r}_l}\mathbf{e}_{\mathrm{B}}-\mathrm{e}^{\mathrm{i}\mathbf{K}'\cdot\vec{r}_l}u_{\mathbf{R}_{\mathrm{A}}}\mathbf{e}_{\mathrm{A}}\Big]\cdot\frac{\vec{r}_l}{|\vec{r}_l|}F^{\mathrm{B}}_{\mathbf{K}}(\mathbf{R}_{\mathrm{A}}-\vec{r}_l)\\
&\quad-\alpha\sum_{l=1,2,3}\mathrm{e}^{\mathrm{i}\mathbf{K}'\cdot\mathbf{R}_{\mathrm{A}}}\Big[u^*_{\mathbf{R}_{\mathrm{A}}-\vec{r}_l}\mathbf{e}_{\mathrm{B}}-\mathrm{e}^{\mathrm{i}\mathbf{K}\cdot\vec{r}_l}u^*_{\mathbf{R}_{\mathrm{A}}}\mathbf{e}_{\mathrm{A}}\Big]\cdot\frac{\vec{r}_l}{|\vec{r}_l|}F^{\mathrm{B}}_{\mathbf{K}'}(\mathbf{R}_{\mathrm{A}}-\vec{r}_l)\\
&=\varepsilon F^{\mathrm{A}}_{\mathbf{K}}(\mathbf{R}_{\mathrm{A}})+\varepsilon\mathrm{e}^{\mathrm{i}\mathbf{K}\cdot\mathbf{R}_{\mathrm{A}}}F^{\mathrm{A}}_{\mathbf{K}'}(\mathbf{R}_{\mathrm{A}}),
\end{aligned} \tag{5.49}$$

where use has been made of the relations $\exp(\mathrm{i}\mathbf{K}\mathbf{R}_{\mathrm{A}})=\exp(-\mathrm{i}\mathbf{K}'\mathbf{R}_{\mathrm{A}})$ and $\exp(2\mathrm{i}\mathbf{K}'\mathbf{R}_{\mathrm{A}})=\exp(\mathrm{i}\mathbf{K}\cdot\mathbf{R}_{\mathrm{A}})$. We can safely assume that the displacement $u_{\mathbf{R}}$ and the envelope function $F^i_{\mathbf{G}}(\mathbf{r})$ vary only slowly over the range corresponding to the extended unit cell which is three times as large as the original cell of a 2D graphite sheet without lattice distortions. When we take an average of eq. (5.49) over the extended unit cell, all the terms except



the first in the left hand side of the above equation vanish and the second term in the right hand side vanishes also. Therefore, the difference equation is reduced to

$$\begin{aligned}
&-\gamma_0\sum_{l=1,2,3}\mathrm{e}^{-\mathrm{i}\mathbf{K}\cdot\vec{r}_l}F^{\mathrm{B}}_{\mathbf{K}}(\mathbf{R}_{\mathrm{A}}-\vec{r}_l)-\alpha\sum_{l=1,2,3}\Big[\mathrm{e}^{\mathrm{i}\mathbf{K}'\cdot\vec{r}_l}u_{\mathbf{R}_{\mathrm{A}}}\mathbf{e}_{\mathrm{B}}-\mathrm{e}^{\mathrm{i}\mathbf{K}\cdot\vec{r}_l}u_{\mathbf{R}_{\mathrm{A}}}\mathbf{e}_{\mathrm{A}}\Big]\cdot\frac{\vec{r}_l}{|\vec{r}_l|}F^{\mathrm{B}}_{\mathbf{K}'}(\mathbf{R}_{\mathrm{A}}-\vec{r}_l)\\
&=\varepsilon F^{\mathrm{A}}_{\mathbf{K}}(\mathbf{R}_{\mathrm{A}}),
\end{aligned} \tag{5.50}$$

where we have introduced the approximation that $u_{\mathbf{R}_{\mathrm{A}}-\vec{r}_l}\sim u_{\mathbf{R}_{\mathrm{A}}}$.

In Appendix D the eigenvectors of the four modes are given in a simple model in which a force constant is introduced only for bond stretching between the nearest-neighbor atoms. The phonon with the highest frequency has the eigen vector $\mathbf{e}_{\mathrm{A}}=(-\mathrm{i}/2,-1/2)$ and $\mathbf{e}_{\mathrm{B}}=(-\mathrm{i}/2,1/2)$ at $\mathbf{K}'=(4\pi/3a,0)$. We have

$$\begin{aligned}
&\mathrm{e}^{-\mathrm{i}\mathbf{K}'\cdot\vec{r}_1}=1,\quad \mathrm{e}^{-\mathrm{i}\mathbf{K}'\cdot\vec{r}_2}=\mathrm{e}^{2\mathrm{i}\pi/3},\quad \mathrm{e}^{-\mathrm{i}\mathbf{K}'\cdot\vec{r}_3}=\mathrm{e}^{-2\mathrm{i}\pi/3},\\
&\mathbf{e}_{\mathrm{A}}\cdot(\vec{r}_1/|\vec{r}_1|)=-1,\quad \mathbf{e}_{\mathrm{B}}\cdot(\vec{r}_1/|\vec{r}_1|)=1,\\
&\mathbf{e}_{\mathrm{A}}\cdot(\vec{r}_2/|\vec{r}_2|)=\mathrm{e}^{\mathrm{i}\pi/3},\quad \mathbf{e}_{\mathrm{B}}\cdot(\vec{r}_2/|\vec{r}_2|)=\mathrm{e}^{2\mathrm{i}\pi/3},\\
&\mathbf{e}_{\mathrm{A}}\cdot(\vec{r}_3/|\vec{r}_3|)=\mathrm{e}^{-\mathrm{i}\pi/3},\quad \mathbf{e}_{\mathrm{B}}\cdot(\vec{r}_3/|\vec{r}_3|)=\mathrm{e}^{-2\mathrm{i}\pi/3},
\end{aligned} \tag{5.51}$$

Expanding the envelope functions with respect to $\vec{r}_l\cdot\vec{\nabla}$ up to the first order for the terms proportional to $\gamma_0$ and to the lowest order for terms proportional to $\alpha$, the effective-mass equation is obtained as

$$\gamma(\hat{k}_x-\mathrm{i}\hat{k}_y)F^{\mathrm{B}}_{\mathbf{K}}(\mathbf{r})-\Delta_1(\mathbf{r})F^{\mathrm{B}}_{\mathbf{K}'}(\mathbf{r})=\varepsilon F^{\mathrm{A}}_{\mathbf{K}}(\mathbf{r}), \tag{5.52}$$

with

$$\Delta_1(\mathbf{r})=3\alpha u(\mathbf{r}). \tag{5.53}$$

The equations for $F^{\mathrm{B}}_{\mathbf{K}}(\mathbf{r})$, $F^{\mathrm{A}}_{\mathbf{K}'}(\mathbf{r})$, and $F^{\mathrm{B}}_{\mathbf{K}'}(\mathbf{r})$ are obtained in the similar manner.

There are other phonon modes at the K' point. For the mode with the smallest frequency the bond-length change does not occur. For the two-fold degenerate modes with an intermediate frequency, the leading term of electron phonon interaction is proportional to $\hat{k}$ and is small. Therefore, the mode having the Kekulé pattern has the strongest interaction with electrons among all modes at the point $\mathbf{K}$ and/or $\mathbf{K}'$. In the following calculation we shall consider only the Kekulé pattern as the possible in-plane lattice distortion.

The final $\mathbf{k}\cdot\mathbf{p}$ equation becomes

$$\begin{pmatrix}\gamma(\sigma_x k_x+\sigma_y k_y)+\sigma_z\Delta_2(\mathbf{r}) & -\mathrm{i}\sigma_y\Delta_1(\mathbf{r})\\ \mathrm{i}\sigma_y\Delta_1^*(\mathbf{r}) & \gamma(\sigma_x k_x-\sigma_y k_y)+\sigma_z\Delta_2(\mathbf{r})\end{pmatrix}\begin{pmatrix}\mathbf{F}_{\mathbf{K}}(\mathbf{r})\\ \mathbf{F}_{\mathbf{K}'}(\mathbf{r})\end{pmatrix}=\varepsilon\begin{pmatrix}\mathbf{F}_{\mathbf{K}}(\mathbf{r})\\ \mathbf{F}_{\mathbf{K}'}(\mathbf{r})\end{pmatrix}. \tag{5.54}$$

Note that the gap parameter for the in-plane Kekulé distortion ($\Delta_1$) is complex in contrast to the real $\Delta_2$ describing the out-of-plane distortion.

In CN's the lattice displacement $\mathbf{u}_i(\mathbf{R}_i)$ given in eq. (5.45) should satisfy the boundary condition

$$\mathbf{u}_i(\mathbf{R}_i+\mathbf{L}) = \mathbf{u}_i(\mathbf{R}_i). \tag{5.55}$$

Because $\exp[\mathrm{i}\mathbf{K}'\cdot(\mathbf{r}+\mathbf{L})] = \exp(\mathrm{i}\mathbf{K}'\cdot\mathbf{r})\exp(-2\pi\nu\mathrm{i}/3)$, we get the boundary condition:

$$u_{\mathbf{R}_i+\mathbf{L}} = u_{\mathbf{R}_i}\exp\Big(-\mathrm{i}\frac{4\pi\nu}{3}\Big), \tag{5.56}$$

which leads to the following condition for the gap parameter:

$$\Delta_1(\mathbf{r}+\mathbf{L}) = \Delta_1(\mathbf{r})\exp\Big(-\mathrm{i}\frac{4\pi\nu}{3}\Big). \tag{5.57}$$

Note that the extra phase factor guarantees the fact that the equations remain the same under translation $\mathbf{r}\to\mathbf{r}+\mathbf{L}$ even for $\nu=\pm1$. On the other hand, the boundary condition for $\Delta_2(\mathbf{r})$ is given by

$$\Delta_2(\mathbf{r}+\mathbf{L}) = \Delta_2(\mathbf{r}), \tag{5.58}$$

since the wave vector of out-of-plane distortion is zero as is shown in Fig. 41 (c).

### 5.3.2 Minimization of total energy

We expand the gap parameters for the circumference direction as

$$\begin{aligned}\Delta_1(x) &= \sum_{n=-\infty}^{\infty}\Delta_1^{(n)}\exp\Big(\mathrm{i}\frac{2\pi n}{L}x\Big)\exp\Big(-\mathrm{i}\frac{4\pi\nu}{3}\frac{x}{L}\Big),\\ \Delta_2(x) &= \sum_{n=-\infty}^{\infty}\Delta_2^{(n)}\exp\Big(\mathrm{i}\frac{2\pi n}{L}x\Big),\end{aligned} \tag{5.59}$$

with $\Delta_1^{(n)}$ and $\Delta_2^{(n)}$ being expansion coefficients, and the envelope functions as in eq. (3.34). The equations for $G$'s are written as

$$\begin{aligned}
&\frac{2\pi\gamma}{L}\sum_n\big(H^{\mathrm{K_B K_A}}_{mn}G^{\mathrm{A}}_{\mathbf{K}n}+H^{\mathrm{K_B K_B}}_{mn}G^{\mathrm{B}}_{\mathbf{K}n}+H^{\mathrm{K_B K'_A}}_{mn}G^{\mathrm{A}}_{\mathbf{K}'n}\big)=\varepsilon G^{\mathrm{B}}_{\mathbf{K}m},\\
&\frac{2\pi\gamma}{L}\sum_n\big(H^{\mathrm{K_A K_B}}_{mn}G^{\mathrm{B}}_{\mathbf{K}n}+H^{\mathrm{K_A K_A}}_{mn}G^{\mathrm{A}}_{\mathbf{K}n}+H^{\mathrm{K_A K'_B}}_{mn}G^{\mathrm{B}}_{\mathbf{K}'n}\big)=\varepsilon G^{\mathrm{A}}_{\mathbf{K}m},\\
&\frac{2\pi\gamma}{L}\sum_n\big(H^{\mathrm{K'_B K'_A}}_{mn}G^{\mathrm{A}}_{\mathbf{K}'n}+H^{\mathrm{K'_B K'_B}}_{mn}G^{\mathrm{B}}_{\mathbf{K}'n}+H^{\mathrm{K'_B K_A}}_{mn}G^{\mathrm{A}}_{\mathbf{K}'n}\big)=\varepsilon G^{\mathrm{B}}_{\mathbf{K}'m},\\
&\frac{2\pi\gamma}{L}\sum_n\big(H^{\mathrm{K'_A K'_B}}_{mn}G^{\mathrm{B}}_{\mathbf{K}'n}+H^{\mathrm{K'_A K'_A}}_{mn}G^{\mathrm{A}}_{\mathbf{K}'n}+H^{\mathrm{K'_A K_B}}_{mn}G^{\mathrm{B}}_{\mathbf{K}n}\big)=\varepsilon G^{\mathrm{A}}_{\mathbf{K}'m},
\end{aligned} \tag{5.60}$$



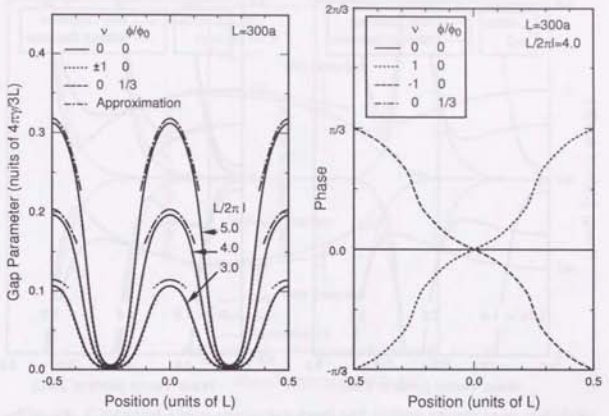


**Fig. 48** (Left) Calculated Kekulé distortion (absolute value of $\Delta_1$) of metallic CN's with $\varphi=0$ (solid lines), $\varphi=1/3$ (dashed lines), and semiconducting CN's with $\varphi=0$ (dotted lines) in various perpendicular field as a function of the position in the circumference direction. Dash-dotted lines correspond to the approximated results.

**Fig. 49** (Right) Calculated phase of $\Delta_1$ versus the position in the circumference direction. The dash-dotted line overlap the solid line completely.

with

$$\begin{aligned}
&H^{\mathrm{K_B K_A}}_{nn}=H^{\mathrm{K'_A K'_B}}_{nn}=\tilde{\kappa}_{\nu\varphi}(n)+\mathrm{i}\frac{Lk}{2\pi},\quad H^{\mathrm{K'_B K'_A}}_{nn}=H^{\mathrm{K_A K_B}}_{nn}=\tilde{\kappa}_{-\nu\varphi}(n)-\mathrm{i}\frac{Lk}{2\pi},\\
&H^{\mathrm{K_B K_A}}_{n\,n\pm1}=-H^{\mathrm{K_A K_B}}_{n\,n\pm1}=-H^{\mathrm{K'_B K'_A}}_{n\,n\pm1}=H^{\mathrm{K'_A K'_B}}_{n\,n\pm1}=\mp\frac{1}{2}\Big(\frac{L}{2\pi l}\Big)^2,
\end{aligned} \tag{5.61}$$

and

$$\begin{aligned}
&H^{\mathrm{K_B K'_A}}_{mn}=-H^{\mathrm{K_A K'_B}}_{mn}=-H^{\mathrm{K'_B K_A}}_{mn}=H^{\mathrm{K'_A K_B}}_{mn}=\frac{L}{2\pi\gamma}\Delta_1^{(m-n)},\\
&H^{\mathrm{K_A K_A}}_{mn}=-H^{\mathrm{K_B K_B}}_{mn}=H^{\mathrm{K'_A K'_A}}_{mn}=-H^{\mathrm{K'_B K'_B}}_{mn}=\frac{L}{2\pi\gamma}\Delta_2^{(m-n)}.
\end{aligned} \tag{5.62}$$

The energy bands $\varepsilon^{(\pm)}_{\nu\varphi}(n,k,H,\{\Delta_1^{(n)}\},\{\Delta_2^{(n)}\})$ are obtained by the diagonalization of eq. (5.60).

The elastic energy of the Kekulé pattern distortion is given by

$$E_{\mathrm{p1}}(\{\Delta_1^{(n)}\}) = \frac{K_1}{6}\sum_{\mathbf{R_A}}\sum_{l=1,2,3}u(\mathbf{R_A},\mathbf{R_A}-\vec{\tau}_l)^2 = \frac{1}{2}NK_1\sum_{n=-\infty}^{\infty}|u_1^{(n)}|^2. \tag{5.63}$$

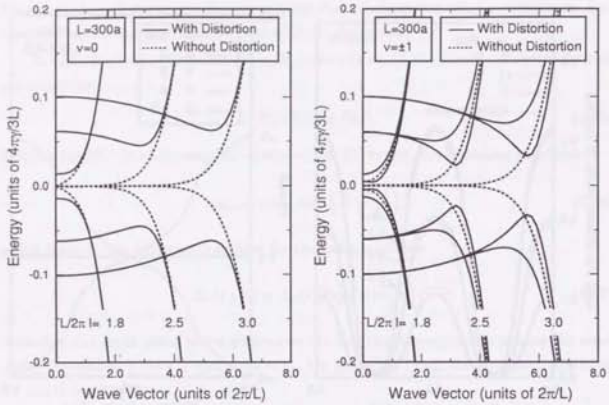


**Fig. 50** Calculated lowest conduction band and highest valence band of metallic (a) and semiconducting (b) CN's in various magnetic fields perpendicular to the tube axis in the presence (solid lines) and the absence (dotted lines) of the in-plane lattice distortion.

The energy of the out-of-plane distortion is obtained in a similar way and written as

$$E_{p2}=\frac{1}{2}NK_2\sum_{n=-\infty}^{\infty}|u_2^{(n)}|^2. \tag{5.64}$$

Then the total energy is obtained by

$$E=2\frac{A}{2\pi}\sum_{m=-\infty}^{\infty}\int_{-\infty}^{\infty}\mathrm{d}k\varepsilon_{\nu\varphi}^{(-)}g_0(|\varepsilon_{\nu\varphi}^{(-)}|)+\frac{NK_1}{2f_1^2}\sum_{n=-\infty}^{\infty}|\Delta_1^{(n)}|^2+\frac{NK_2}{2f_2^2}\sum_{n=-\infty}^{\infty}|\Delta_2^{(n)}|^2. \tag{5.65}$$

In general, Kekulé and out-of-plane distortions may coexist in contrast to the case of constant distortion, in which only Kekulé or out-of-plane distortion occurs. In this paper we shall calculate gap parameter of Kekulé distortion numerically. A series of gap parameters $\Delta_1^{(n)}$ is obtained by searching the minimum of the total energy numerically with use of the conjugate gradient method instead of solving gap equations.

### 5.3.3 High magnetic field

In the limit of $L/2\pi l\to\infty$ the distortion at position $\theta$ approaches that of a 2D graphite sheet in magnetic field $H\cos\theta$ except in the region $\theta\sim\pm\pi/2$. Thus, from eq.



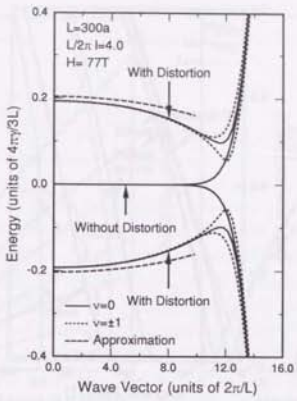


**Fig. 51** Calculated lowest conduction band and highest valence band of metallic and semiconducting CN's in a magnetic field perpendicular to the tube axis in the presence and the absence of in-plane lattice distortion.

(5.44) the gap parameter $\Delta=\Delta_1$ or $\Delta_2$ at $\theta$ is obtained as

$$\Delta(\theta)=\frac{\lambda}{4}\frac{a\gamma}{l^2}|\cos\theta|. \tag{5.66}$$

It is noted that the average of eq. (5.66) over $\theta$ agrees with the gap approximated by constant distortions written as eq. (5.42).

### 5.3.4 Numerical results

Figure 48 shows the absolute value of the gap parameter$\Delta_1$ calculated for $\lambda_1=1.62$ as a function of the position in the circumference direction. The magnitude of the distortion is independent of whether CN's are metallic or semiconducting and the magnetic flux. The distortion becomes maximum at $x/L=0$ (top) and $\pm1/2$ (bottom) and minimum at $x/L=\pm1/4$ (side). The maximum distortion increases with the increase of the magnetic field. The approximate gap parameter $\Delta_1(\theta)$ given by eq. (5.66) is denoted by the dashed lines in the range of the position where a well-defined Landau level is formed.

Figure 49 exhibits the phase of $\Delta_1$ as a function of the position. Because of the boundary condition of $\Delta_1$ in eq. (5.57) a non-vanishing phase appears for semiconducting CN's.

Figure 50 shows the calculated energy bands of metallic (a) and semiconducting

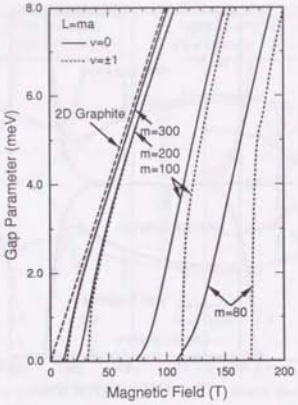


**Fig. 52** Calculated absolute value of gap parameter $\Delta_1$ versus magnetic field for metallic and semiconducting CN's.

(b) CN's near the K and K' points in a various perpendicular field. In a weak field ($L/2\pi l = 1.8$) the band gap increases monotonically with increase of $|k|$. However, in a strong field the gap takes its maximum at $k=0$ and decreases gradually with increasing $|k|$. The gap takes its minimum value near the critical wave vector in which the flat levels in the absence of distortion (denoted by 'Without Distortion') start to depend on $k$. At the minimum gap the degeneracy of K and K' points is lifted for semiconducting CN's while the two-fold degeneracy remains for metallic CN's. This is discussed in Appendix E.

Figure 51 shows the calculated energy bands of metallic and semiconducting CN's. The dashed lines denote the gap parameter approximated by eq. (5.66) with $\sin\theta(k) = -2\pi l^2 k/L$. It is demonstrated in Appendix E that the gap parameter corresponds to the lowest conduction and the highest valence bands. The deviation from the numerical results increase with wave vector, since the spatial extent of the wave function of the cyclotron motion becomes larger and the approximation becomes less valid.

Figure 52 exhibits the absolute value of the gap parameter $\Delta_1$ at $k=0$ of metallic and semiconducting CN's with various circumferences $L=ma$ with integer $m$ with use of $\lambda = 1.62$. The gap parameter of semiconducting CN's approaches that of metallic CN's with the increase of the magnetic field. The parameter for both metallic and semiconducting CN's having infinitely large circumference approaches that of a 2D graphite sheet as is



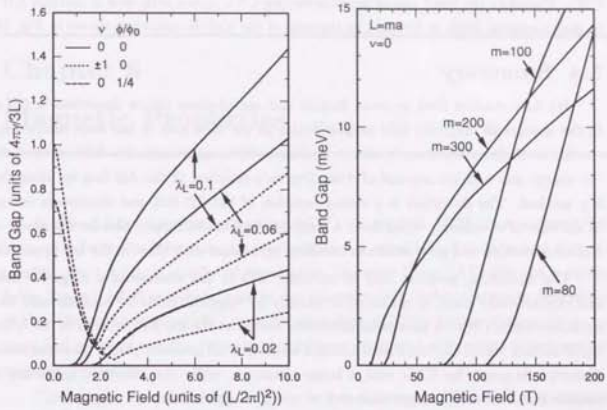


**Fig. 53** (Left) Calculated band gap versus dimensionless magnetic field.
**Fig. 54** (Right) Calculated band gap of metallic CN's versus magnetic field.

expected.

Figure 53 shows the band gap of metallic and semiconducting CN's with various coupling constants. The band gap of semiconducting CN's does not agree with that of metallic CN's even in a strong magnetic field because two-fold degeneracy of bands is lifted at the corresponding wave vector. The band gap of metallic CN's are shown in Fig. 54. The gap of CN's having larger circumference becomes smaller in high magnetic field. This is because of the fact that the highest conduction band starts to decrease with $|k|$ in a weaker magnetic field for CN's having larger circumference.

Let us discuss the case of the out-of-plane distortion qualitatively without explicit calculations. It is expected that the spatial variation of the absolute value of $\Delta_2$ and its dependence on the magnetic field are similar to those for $\Delta_1$ shown in Fig. 48. The phase of $\Delta_2$, however, becomes zero everywhere independent of whether CN's are metallic or semiconducting in contrast to that of $\Delta_1$ having nonvanishing phase for semiconducting CN's shown in Fig. 49. This is because of the fact that there is no extra phase factor in the boundary condition for $\Delta_2$ given by eq. (5.58) even for semiconducting CN's. The dispersion curves of the lowest conduction band and the highest valence band are expected to be similar to those for the Kekulé distortion exhibited in Figs. 50 and 51. However, the degeneracy in the conduction band is not lifted even for semiconducting

CN's. Therefore the band gap of semiconducting CN's agrees with that of metallic CN's in high magnetic fields in contrast to the case of the Kekulé distortion shown in Fig. 53.

## 5.4 Summary

We have studied both in-plane Kekulé and out-of-plane lattice distortion in CN's. In the absence of magnetic field perpendicular to the tube axis, it has been shown that two kinds of distortion cannot coexist and an analytic expression has been derived for the energy gap and the amount of distortion as a function of the AB flux by using the **k·p** method. The distortion is a strong function of the AB flux and disappears except in the case of vanishingly small flux. A tight-binding model is used also for the study of Kekulé distortion and gave results in excellent agreement with those in the **k·p** approach.

The distortion, presents only in metallic CN's in the absence of a magnetic field and exponentially small, is enhanced drastically by magnetic fields for both metallic and semiconducting CN's. A maximum distortion occurs at the top and bottom of the cylindrical surface where electrons form Landau levels in a 2D graphite plane. The maximum distortion is larger for CN's with a larger diameter, while the minimum distortion is smaller for CN's with a larger diameter in strong magnetic fields.

# Chapter 6
# Magnetic Properties

In this chapter magnetic properties of CN's are studied. [63–66] In a magnetic field perpendicular to the tube axis, the magnetization is essentially determined by that of a graphite sheet, while it is induced also by the Aharonov-Bohm (AB) effect in a parallel field. The AB effect manifests itself in the magnetic-field and temperature dependence of the differential susceptibility even for ensembles of CN's having various circumferences and orientations. The theoretical results are compared with recent experiments on magnetic properties.

This chapter is organized as follows: In Sec. 6.1 susceptibility and magnetization are studied for single-shell CN's with carrier doping. In Sec. 6.2 the magnetization and the susceptibility of realistic samples of CN's without carrier doping are calculated. A summary is given in Sec. 6.3.

## 6.1 Magnetic Properties of Single Nanotubes

### 6.1.1 Magnetization and susceptibility

In the following calculation, the $M^{\parallel}(\chi^{\parallel})$ and $M^{\perp}(\chi^{\perp})$ represent the components of magnetic moment (susceptibility) in the direction of parallel and perpendicular direction of tube axis, respectively, as shown in Fig. 55. Further, a set of the quantum numbers $(\lambda, n, k)$ specifying each state is represented by a single character $\tau$. We have

$$\varepsilon_\tau = \varepsilon_{\nu\varphi}^{(\lambda)}(n, k, H_\perp), \tag{6.1}$$

and

$$\sum_\tau = \frac{A}{2\pi} \sum_{\lambda=\pm} \sum_{n=-\infty}^{\infty} \int_{-\infty}^{\infty} \mathrm{d}k. \tag{6.2}$$

Noting that $\nu$ and $\varphi$ appear in energy as a combination $\varphi - \nu/3$, we have the free energy for electrons in the vicinity of the K point

$$F\left(\varphi - \frac{\nu}{3}, H_\perp\right) = N\mu - k_\mathrm{B}T \sum_\tau g_0(\varepsilon_\tau) \ln\left[1 + \exp\left(-\frac{\varepsilon_\tau - \mu}{k_\mathrm{B}T}\right)\right], \tag{6.3}$$

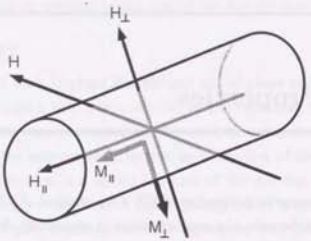


**Fig. 55** Components of magnetic moment (susceptibility) in the parallel ($M^{\parallel}(\chi^{\parallel})$) and the perpendicular ($M^{\perp}(\chi^{\perp})$) direction to the tube axis.

where $T$ is temperature, $k_B$ is the Boltzmann constant, and $\mu$ is the chemical potential satisfying the condition that the electron number is constant. Further, $g_0(\varepsilon)$ is the cutoff function defined in eq. (5.11) containing two parameters, $\varepsilon_c$ and $\alpha_c$. Results do not depend on these parameters, as long as $\varepsilon_c$ is sufficiently large and $\alpha$ is not extremely large. In fact, this cutoff function can be eliminated in an appropriate procedure. Details are discussed in Appendix F.

The magnetic moment in the direction parallel ($\parallel$) or perpendicular ($\perp$) to the axis is calculated by taking a first derivative of $F$ with respect to the field under the condition that the total number of electrons is fixed. The result is represented as

$$M^{\parallel,\perp}\Big(\varphi-\frac{\nu}{3},H_\perp\Big)=\int_{-\infty}^{\infty}\mathrm{d}\,\varepsilon M^{\parallel,\perp}\Big(\varphi-\frac{\nu}{3},H_\perp,\varepsilon\Big)\Big(-\frac{\partial f(\varepsilon)}{\partial\varepsilon}\Big), \tag{6.4}$$

where $f(\varepsilon)$ is the Fermi distribution function and $M^{\parallel,\perp}(\varepsilon)$ is the magnetic moment at zero temperature for the Fermi level $\varepsilon$, given by

$$M^{\parallel,\perp}\Big(\varphi-\frac{\nu}{3},H_\perp,\varepsilon\Big)=-\sum_\tau\frac{\partial\varepsilon_\tau}{\partial H_{\parallel,\perp}}g_1(\varepsilon_\tau)\theta(\varepsilon-\varepsilon_\tau), \tag{6.5}$$

with $\theta(\varepsilon-\varepsilon_\tau)$ being the step function. Equation (6.5) is also obtained from the derivative of a total energy under the condition of the particle number conservation. Adding the contribution from K' point and multiplying the factor two of spin degeneracy (the spin-Zeeman energy is small and therefore neglected for simplicity), we obtain the magnetic



moment $M_M$ of a metallic CN and $M_S$ of a semiconducting one as follows:

$$\begin{cases} M_M^{\parallel,\perp}(\varphi,H_\perp)=4M^{\parallel,\perp}(\varphi,H_\perp),\\ M_S^{\parallel,\perp}(\varphi,H_\perp)=2M^{\parallel,\perp}(\varphi+1/3,H_\perp)+2M^{\parallel,\perp}(\varphi-1/3,H_\perp).\end{cases} \tag{6.6}$$

The susceptibility per unit area at nonzero temperatures can be also written in terms of the susceptibility at zero temperature in the same way as the magnetic moment.

$$\chi^{\parallel,\perp}\Big(-\frac{\nu}{3}\Big)=\int_{-\infty}^{\infty}\mathrm{d}\varepsilon\,\chi^{\parallel,\perp}\Big(-\frac{\nu}{3},\varepsilon\Big)\Big(-\frac{\partial f(\varepsilon)}{\partial\varepsilon}\Big), \tag{6.7}$$

with

$$\chi^{\parallel,\perp}\Big(-\frac{\nu}{3},\varepsilon\Big)=\frac{1}{AL}\lim_{H_{\parallel,\perp}\to0}\frac{\partial}{\partial H_{\parallel,\perp}}M^{\parallel,\perp}\Big(\varphi-\frac{\nu}{3},H_\perp,\varepsilon\Big). \tag{6.8}$$

Adding the contribution of K' point, we get the susceptibility of metallic and semiconducting CN's as follows:

$$\begin{cases}\chi_M^{\parallel,\perp}(T,\mu)=4\chi^{\parallel,\perp}(0),\\ \chi_S^{\parallel,\perp}(T,\mu)=2\chi^{\parallel,\perp}(1/3)+2\chi^{\parallel,\perp}(-1/3).\end{cases} \tag{6.9}$$

### 6.1.2 Undoped CN's at Zero Temperature

Let us first consider magnetic properties of undoped CN's at zero temperature in the parallel field. In a straightforward calculation from eq. (6.5), we get

$$M^{\parallel}(\varphi,0)=\mu_B\frac{A}{a}\frac{2ma\gamma}{\hbar^2}W_1(\varphi), \tag{6.10}$$

where $\mu_B=e\hbar/2mc$ is the Bohr magneton and $W_1(\varphi)$ is dimensionless quantity given by

$$W_1(\varphi)=\frac{1}{4\pi}\sum_{n=-\infty}^{\infty}\int_{-\infty}^{\infty}d\tilde{k}\,\frac{\kappa_{0\varphi}(n)}{\sqrt{\kappa_{0\varphi}(n)^2+\tilde{k}^2}}\,g_1\big(|\varepsilon_{0\varphi}^{(-)}(n,k)|\big), \tag{6.11}$$

with $\tilde{k}=Lk/2\pi$. As is derived in Appendix F, in the vicinity of $\varphi=n$ with $n$ being an integer, $W_1$ is obtained as

$$W_1(\varphi)\approx-\frac{1}{2\pi}(\varphi-n)\ln|\varphi-n|\quad(|\varphi-n|\ll1). \tag{6.12}$$

Therefore, the moment itself vanishes but its derivative diverges logarithmically (positive infinite) at $\varphi=n$ and metallic CN's show paramagnetism in a weak parallel field.

Figure 56 shows the magnetic moment of a metallic and semiconducting CN as a function of $\varphi$ obtained in the present $\mathbf{k}\cdot\mathbf{p}$ approximation (a) and in a tight-binding model

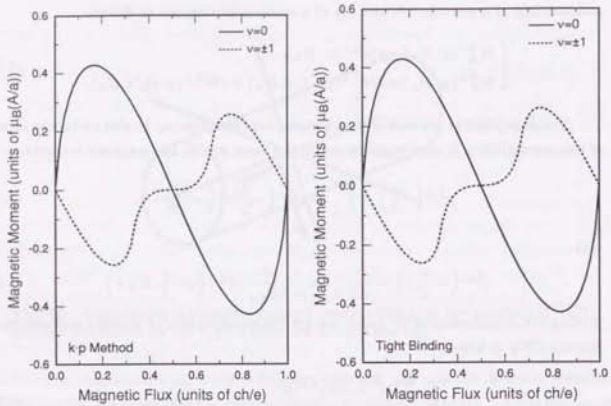


**Fig. 56** Magnetic moment of metallic (solid line) and semiconducting (dotted line) CN's versus magnetic flux parallel to the tube axis calculated in the effective-mass approximation (a) and tight-binding model (b).

(b). The moment calculated in the effective-mass approximation is in excellent agreement with that of a tight-binding model. The magnetic moment is a periodic function of flux with period of magnetic flux quantum since the moment is induced by the AB flux. In a weak field metallic and semiconducting CN's show paramagnetism and diamagnetism, respectively.

It should be noted that this magnetic moment is closely related to the persistent current in metallic rings.[67,68] For a small metallic ring with magnetic flux, each eigenstate carries a nonzero current along the ring. Because of a large cancellation the total current becomes very small after the summation over all occupied states up to the Fermi level.[69,70] Though the situation in CN is certainly different from that in usual metallic rings, similar large cancellation exists even in CN.

In order to calculate the susceptibility for a magnetic field perpendicular to the tube axis, we first calculate the shift of the energy levels up to the second order in magnetic-field strength $H_\perp$. As has been shown in Chapter 3, the magnetic field introduces the following perturbation described by the Hamiltonian $H'$ defined by

$$H'_{n'n} = \mp\frac{1}{2}\frac{2\pi\gamma}{L}\Big(\frac{L}{2\pi\ell}\Big)^2\begin{pmatrix}0 & 1\\ 1 & 0\end{pmatrix}\delta_{n'n\pm1}. \tag{6.13}$$



The matrix elements between the eigenstates in the absence of a magnetic field are calculated as

$$\begin{aligned}(n',+|H'|n,-) &= \pm\frac{1}{4}\frac{2\pi\gamma}{L}\Big(\frac{L}{2\pi l}\Big)^2\big[b^*_{\nu\varphi}(n,k)-b_{\nu\varphi}(n\pm1,k)\big]\delta_{n'n\pm1},\\ (n',-|H'|n,-) &= \mp\frac{1}{4}\frac{2\pi\gamma}{L}\Big(\frac{L}{2\pi l}\Big)^2\big[b^*_{\nu\varphi}(n,k)+b_{\nu\varphi}(n\pm1,k)\big]\delta_{n'n\pm1}.\end{aligned} \tag{6.14}$$

Except in the case of an accidental degeneracy mentioned later, the magnetic field causes an energy shift to the second order in its strength. We have

$$\Delta\varepsilon^{(-)}_{\nu\varphi}(n,k) = \sum_{w=\pm}\sum_{n'=n\pm1}\frac{\big|(n,-|H'|n',w)\big|^2}{\varepsilon^{(-)}_{\nu\varphi}(n,k)-\varepsilon^{(w)}_{\nu\varphi}(n',k)}. \tag{6.15}$$

The shift in the total energy becomes

$$\begin{aligned}\Delta E\Big(\varphi-\frac{\nu}{3}\Big) &= \frac{A}{2\pi}\sum_{n=-\infty}^{\infty}\int_{-\infty}^{\infty}dk\Big[\big(\varepsilon^{(-)}_{\nu\varphi}+\Delta\varepsilon^{(-)}_{\nu\varphi}\big)\,g_0\big(|\varepsilon^{(-)}_{\nu\varphi}+\Delta\varepsilon^{(-)}_{\nu\varphi}|\big)-\varepsilon^{(-)}_{\nu\varphi}\,g_0\big(|\varepsilon^{(-)}_{\nu\varphi}|\big)\Big]\\ &= \frac{A}{2\pi}\sum_{n=-\infty}^{\infty}\int_{-\infty}^{\infty}dk\,\Delta\varepsilon^{(-)}_{\nu\varphi}(n,k)\;g_1\big(|\varepsilon^{(-)}_{\nu\varphi}(n,k)|\big).\end{aligned} \tag{6.16}$$

The susceptibility per unit area is calculated as

$$\chi^\perp\Big(\varphi-\frac{\nu}{3}\Big) = -\frac{1}{AL}\frac{A}{2\pi}\sum_{n=-\infty}^{\infty}\int_{-\infty}^{\infty}dk\frac{\partial^2\Delta\varepsilon^{(-)}_{\nu\varphi}(n,k)}{\partial H^2}g_1(|\varepsilon^{(-)}_{\nu\varphi}(n,k)|). \tag{6.17}$$

Note the change in the cutoff function from $g_0(\varepsilon)$ to $g_1(\varepsilon)$ (defined in (5.13)) in the above.

There occurs an accidental degeneracy for some values of $\nu$ and $\varphi$. Consider the case $\nu=0$ and $\varphi=1/2$, for example. In this case, the valence-band states with $n=0$ and $n=-1$ are degenerate with each other and the second order perturbation breaks down because of the presence of the shift to the first order in $H$. When the energy shifts are summed over all the occupied valence band states, this first order energy shift cancels out with each other and does not contribute to the total energy. The only modification is that intermediate states $n'$ accidentally degenerate with the band $n$ should be excluded in the summation in Eq. (6.15). This is a result of the fact that the trace of a matrix is invariant under any unitary transformations.

After a straightforward manipulation, $\chi(\varphi)$ is transformed into the following expression:

$$\chi(\varphi) = -\chi^*\,\frac{L}{a}\,W_2(\varphi), \tag{6.18}$$

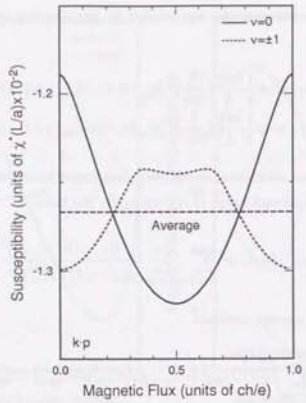


**Fig. 57** Susceptibility of metallic (solid line) and semiconducting (dotted line) CN's versus magnetic flux parallel to the tube axis calculated in the effective-mass approximation.

where $W_2(\varphi)$ is the dimensionless quantity defined by

$$W_2(\varphi) = \frac{1}{2\pi^4} \sum_{n=-\infty}^{\infty} \int_{-\infty}^{\infty} d\tilde{k}\, \frac{\sqrt{(n+\varphi)^2+\tilde{k}^2}}{1-4(n+\varphi)^2}\, g_1(|\varepsilon_{0\varphi}^{(-)}(n,k)|), \tag{6.19}$$

and $\chi^*$ is a characteristic susceptibility defined by

$$\chi^* = \frac{2\pi\gamma}{a}\left(\frac{\phi_0}{\pi a^2}\right)^{-2}\frac{1}{a^2}, \tag{6.20}$$

corresponding to $1.46\times10^{-4}$emu/mol or $1.21\times10^{-5}$emu/g for $\gamma=6.46$eV·Å.

Figure 57 shows the calculated susceptibility of a metallic and semiconducting CN's. The susceptibility is negative irrespective of $\varphi$, i.e., CN's are diamagnetic for a magnetic field perpendicular to the axis. The absolute magnitude of the susceptibility of a metallic CN is smallest for $\phi=0$ and takes a maximum at $\varphi=1/2$, though the variation itself is small. Further the susceptibility of metallic and semiconducting CN's is not so different from each other.

The weak dependence of the susceptibility on the magnetic flux is understood as follows. When a magnetic field perpendicular to the axis is applied, Landau levels begin to be formed. The Landau levels are essentially those of a 2D graphite layer and therefore



the band gap decreases with magnetic field as has been discussed in Chapter 3. This effect, which is the origin of the diamagnetism, is larger for CN's with larger band gap in the absence of a magnetic field. Consequently, the diamagnetic susceptibility takes a maximum for CN's with largest band gap ($\varphi=1/2$ for $\nu=0$) and a minimum with vanishing gap ($\varphi=0$ for $\nu=0$).

Equation (6.18) shows that the susceptibility is proportional to the circumference $L$ and therefore diverges in the limit of infinitely large $L$. This dependence is closely related to the susceptibility of a 2D graphite sheet. The following expression was derived for the susceptibility per unit area of a graphite sheet:[71,72]

$$\chi = -\frac{\gamma^2}{3\pi}\frac{1}{\mu}\left(\frac{e}{ch}\right)^2, \tag{6.21}$$

For a single ideal 2D graphite layer, the Fermi energy $\mu$ vanishes and the susceptibility diverges at zero temperature. Because of the large interlayer spacing in comparison with $a$, the diamagnetic response of graphite is dominated by that of a single graphite layer. Weak interlayer coupling leads to a small dispersion in the direction perpendicular to the layer and modifies the Fermi energy.[73] Consequently, a 3D graphite has a finite but very large diamagnetic susceptibility observed experimentally.[74]

An expression independent of the cutoff function is derived in Appendix F. In particular, the average over $\varphi$ can be calculated analytically as $\bar{W}_2=1/32\pi^2$, which gives

$$\bar{\chi}_M = \bar{\chi}_S = -1.27\times10^{-2}\times\frac{L}{a}\chi^*. \tag{6.22}$$

Equation (6.21) is written as

$$\chi = -\frac{1}{3\pi^3}\frac{2\pi\gamma}{L}\mu^{-1}\frac{L}{a}\chi^* = -1.08\times10^{-2}\,\frac{2\pi\gamma}{L}\mu^{-1}\frac{L}{a}\chi^*. \tag{6.23}$$

This agrees with the susceptibility of CN if we replace $\mu$ by $0.85\times\gamma(2\pi/L)$ which is the typical confining energy due to a finite circumference.

### 6.1.3 Numerical results: susceptibility

Susceptibility at zero temperature is calculated by using eq. (6.8), and the results are shown in Fig. 58 as a function of the Fermi energy $\mu$. The susceptibility at $\mu=0$ agrees with that of a previous paper.[63,64,75] Both metallic and semiconducting CN's show positive divergent susceptibility in the parallel field where the Fermi energy lies at band edges. The divergence for metallic CN's is logarithmic as shown in Appendix G, while that for semiconducting CN's corresponds to that of the density of states at band edges. When the Fermi energy moves away from band edges, the parallel susceptibility becomes negative (diamagnetic). For a perpendicular field, CN is diamagnetic but turns into paramagnetic when the Fermi energy becomes away from $\mu=0$.

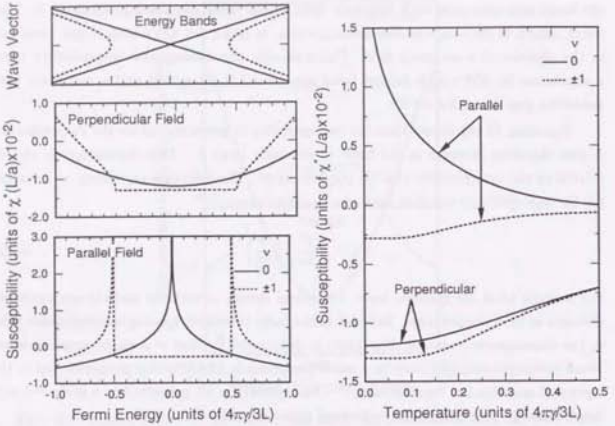


**Fig. 58** (Left) (Up) The band structures of metallic (solid lines) and semiconducting (dotted lines) CN's. Calculated susceptibility of metallic (solid lines) and semiconducting (dotted lines) CN's in the direction of perpendicular (Middle) and parallel (Down) to the tube axis versus chemical potential at zero temperature.

**Fig. 59** (Right) Calculated susceptibility of metallic (solid lines) and semiconducting (dotted lines) CN's in the direction of parallel and perpendicular to the tube axis versus temperature.

Figure 59 shows the susceptibility in the parallel and perpendicular directions for $\mu=0$ as a function of temperature. Note that the chemical potential does not vary with temperature due to the symmetry of the density of states about $\varepsilon=0$. The positive susceptibility of metallic CN's in the parallel direction decreases rapidly with temperature, while the other negative susceptibilities rise very slowly. This temperature dependence can easily be understood from the Fermi-level dependence of the zero-temperature susceptibility shown in Fig. 58.

### 6.1.4 Numerical results: magnetization

Figure 60 gives calculated magnetization in a parallel direction of metallic CN's at zero temperature. It shows that the parallel magnetization is reduced considerably in a strong perpendicular magnetic field. This is a direct consequence of the fact that the energy shift induced by the AB flux becomes small in a perpendicular magnetic field, as has been discussed in Chapter 3. The figure contains also the result for nonvanishing carrier density $n_d$ per unit area. For $n_d L^2 = 4$, for example, the magnetic moment is



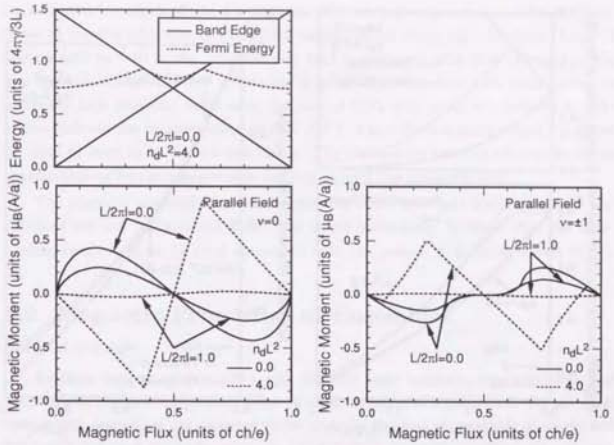


**Fig. 60** (Left) (Up) Edges of the lowest and the second lowest conduction bands (solid lines) and Fermi energy (dotted line) for metallic CN's with carrier density $n_d L^2 = 4$ versus magnetic flux passing through the cross section of CN's in the absence of perpendicular magnetic field. (Down) Calculated magnetization in the parallel direction for metallic CN's for $n_d L^2 = 0$ and 4 in a magnetic field $L/2\pi l = 0$ and 1 at zero temperature.

**Fig. 61** (Right) Calculated magnetization in the parallel direction for semiconducting CN's with $n_d L^2 = 0$ and 4 in a magnetic field $L/2\pi l = 0$ and 1 at zero temperature.

negative corresponding to the diamagnetic susceptibility shown in Fig. 58 in a weak parallel field, but exhibits cusps when the Fermi level crosses band edges as shown in the upper panel of Fig. 60. The magnetization for $n_d L^2 = 4$ nearly vanishes in a strong perpendicular magnetic field.

The results for semiconducting CN's are shown in Fig. 61. In the absence of carrier and perpendicular field, the magnetic moment decreases linearly in a weak field and increases sharply in the range of $0.3 \lesssim \phi/\phi_0 \lesssim 0.4$. The change of magnetization curves due to carrier doping and perpendicular field can be understood in the same way of that for metallic CN's.

Figure 62 shows the magnetization of metallic CN's at zero temperature as a function of perpendicular field. In the undoped case, the absolute value of the magnetization increases smoothly with the magnetic field. In the case of $n_d L^2 = 7.5$, on the other hand, the magnetization changes from positive (paramagnetic) to negative (diamagnetic). This

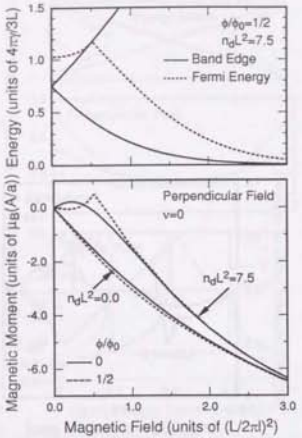


**Fig. 62** (Left) (Up) Edges of the lowest and the second lowest conduction bands (solid lines) and Fermi energy (dotted line) for metallic CN's versus perpendicular magnetic field with AB flux $\varphi = 1/2$ and carrier density $n_d L^2 = 7.5$. (Down) Calculated magnetization for metallic CN's versus perpendicular magnetic field in AB flux $\phi/\phi_0 = 0$ and $1/2$ for carrier density $n_d L^2 = 0$ and 7.5.

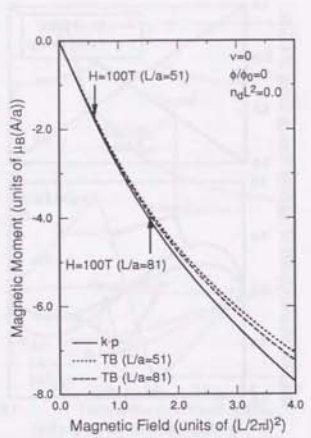


**Fig. 63** (Right) Calculated magnetization of metallic CN's with $n_d L^2 = 0$ versus perpendicular magnetic field in both **kp** approximation (solid line) and tight-binding model of zigzag CN's having circumference $L = 51a$ (dotted line) and $81a$(dashed line). The magnetization in the **k·p** method shows good agreement with that in the tight-binding model up to about 100 T.

change is again due to the band-edge crossing of the Fermi level. In sufficiently high magnetic fields, the magnetization becomes nearly independent of the carrier concentration. This is a consequence of the fact that the lowest band forms dispersionless Landau level and does not contribute to magnetization when $L/2\pi l \gg 1$.

Figure 62 contains results for the AB flux $\phi/\phi_0 = 1/2$. In the absence of the perpendicular field, two bands with $n = 0$ and $-1$ are degenerate and this degeneracy is lifted linearly with increasing field as shown in the upper panel and as has been discussed in Sec. 6.1.2. The magnetization becomes independent of the AB flux again in sufficiently high magnetic fields.

### 6.1.5 Tight-binding model

The magnetization and susceptibility of CN's can be calculated also in a tight-binding model in which effects of a magnetic field can be incorporated as a Peierls' phase factor in transfer integrals. In Fig. 63 the magnetization of zig-zag nanotubes ($L/a = 51$ and 81 with $n_b = 0$) in the perpendicular field is compared with that obtained in the **k·p** approximation. The two results are in good agreement with each other except in extremely high magnetic fields or in the case of CN's with small circumferences. The arrows indicate the magnetization at $H = 100$ T, where the magnetic length $l$ is about 10 times as large as the lattice constant $a$. The discrepancy between the results of two approximations becomes appreciable roughly around this magnetic field.

The magnetic susceptibility was recently calculated in a tight-binding model[76] and therefore will not be presented here. It is worth mentioning, however, that the tight-binding result is again in good agreement with the present **k·p** result shown in Fig. 58.



## 6.2 Magnetic Properties of Ensembles

### 6.2.1 Average

Realistic samples contain CN's with different layer numbers, circumferences, and orientations. Because interactions between adjacent layers of a multi-shell CN are weak, its magnetic properties are expected to be given by those of an ensemble of single-shell CN's with different circumferences. In the following, we shall calculate the magnetic moment of ensembles of CN's. We shall confine ourselves to the case of undoped CN's for simplicity. The ensemble average of magnetic moment is given by

$$\langle M(H)\rangle_{\rm av} = \frac{1}{3}\langle M_{\rm M}(H)\rangle_{\rm av} + \frac{2}{3}\langle M_{\rm S}(H)\rangle_{\rm av}, \tag{6.24}$$

where

$$\begin{aligned}\langle M_{\rm M,S}(H)\rangle_{\rm av} = \int {\rm d}L\rho(L)\int\frac{{\rm d}\Omega}{4\pi}\Big[M^{\parallel}_{\rm M,S}\Big(\frac{L^2H}{4\pi\phi_0}\cos\theta, H\sin\theta\Big)\cos\theta \\ + M^{\perp}_{\rm M,S}\Big(\frac{L^2H}{4\pi\phi_0}\cos\theta, H\sin\theta\Big)\sin\theta\Big],\end{aligned} \tag{6.25}$$

with $H$ being the strength of magnetic field, $\Omega$ being solid angle, $\theta$ being the angle between a magnetic field and tube's axis, and $\rho(L)$ being a normalized distribution function of circumference length of a sample.

In weak magnetic fields, the magnetic moment is written by using the susceptibility as

$$\begin{cases} M^{\parallel}_{\rm M,S}(H) = \chi^{\parallel}_{\rm M,S} H\cos\theta\cdot AL, \\ M^{\perp}_{\rm M,S}(H) = \chi^{\perp}_{\rm M,S} H\sin\theta\cdot AL. \end{cases} \tag{6.26}$$

From eqs. (6.24)–(6.26), the magnetic moment of ensembles of CN's is represented as

$$\langle M(H)\rangle_{\rm av} = \langle\chi\rangle_{\rm av} H\cdot AL_{\rm av}, \tag{6.27}$$

with

$$\langle\chi\rangle_{\rm av} = \int {\rm d}L\rho(L)\frac{1}{9}\left[\chi_{\rm M}^{\parallel}+2\chi_{\rm M}^{\perp}+2\chi_{\rm S}^{\parallel}+4\chi_{\rm S}^{\perp}\right]. \tag{6.28}$$

At zero temperature the susceptibility diverges for some values of $\mu$ corresponding to band edges, where the magnetization is not given by eq. (6.26). However, this divergence is removed at nonzero temperatures. At sufficiently low temperatures and in low magnetic fields, the magnetization exhibits a small paramagnetism due to the AB effect of metallic CN's.[66] The corresponding temperature is very low and is given by $k_{\rm B}T \lesssim \gamma(2\pi/L)\times 10^{-7}$ as shown in Appendix G.

The distribution function $\rho(L)$ is not known and therefore we shall consider following three different kinds:

$$\begin{aligned}
&\rho(L)=\frac{1}{\sqrt{2\pi}\sigma}\exp\left[-\frac{(L-L_{\rm av})^2}{2\sigma^2}\right]: && \text{Gaussian Distribution,}\\
&\rho(L)=\frac{1}{L_{\rm mx}-L_{\rm mn}} \quad (L_{\rm mn}<L<L_{\rm mx}): && \text{Rectangular Distribution,}\\
&\rho(L)=2\frac{L_{\rm mx}-L}{(L_{\rm mx}-L_{\rm mn})^2} \quad (L_{\rm mn}<L<L_{\rm mx}): && \text{Triangular Distribution.}
\end{aligned} \tag{6.29}$$

The first is the Gaussian distribution around a certain average circumference $L_{\rm av}$ with the root-mean-square deviation $\sigma$. The rectangular distribution roughly corresponds to the situation that CN's with different circumferences are distributed equally and the average layer number of multi-shell CN's is independent of the circumference. When the average layer number of CN's increases with the circumference, on the other hand, the number of CN's with small circumferences is effectively enhanced and the distribution becomes asymmetric about $L_{\rm av}$. The most extreme case can be realized if we assume that each CN has layers such that the circumference of the inner-most shell is always $L_{\rm mn}$. In this case the distribution is given by a triangular form.

### 6.2.2 Numerical results

Figure 64 gives the calculated magnetization and differential susceptibility of CN ensembles at zero temperature as a function of a magnetic field. Results for the Gaussian and triangular distributions are shown and the unit $(L/2\pi l)^2$ of the magnetic field is for $L_{\rm av}$. This shows clearly that characteristic features of the magnetic properties are essentially determined by those of single-shell CN's having the average circumference.

The magnetic moment is negative (diamagnetic) and its absolute value increases as a function of the magnetic field. This overall dependence is governed by that of the magnetic moment for perpendicular magnetic field shown in Fig. 62 and the parallel contribution or the AB effect appears as a slight deviation. This deviation becomes clearer in the differential susceptibility. In fact, the differential susceptibility increases with the decrease of the magnetic field sharply in weak magnetic fields $(L/2\pi L)^2 \lesssim 0.2$. This is a result of the divergent paramagnetic susceptibility of metallic CN's in the



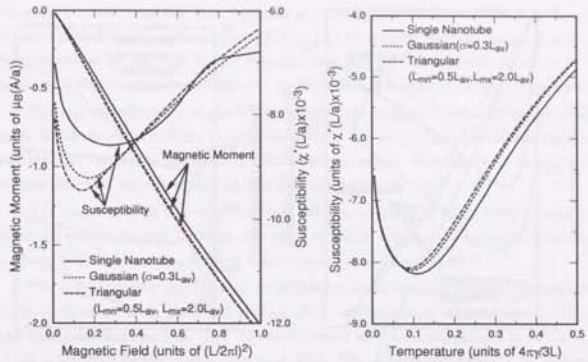


**Fig. 64** (Left) Calculated magnetization and differential susceptibility of realistic samples in which the distribution of circumference is delta-function (solid lines), Gaussian with $\sigma = 0.3L_{\rm av}$ (dotted lines), and triangular having $L_{\rm mn} = 0.5L_{\rm av}$ and $L_{\rm mx} = 2L_{\rm av}$ (dashed lines). Solid lines represent the results of single CN's having the same circumference length.

**Fig. 65** (Right) Calculated susceptibility of realistic samples without carrier versus temperature in which the distribution of circumference is delta-function (solid lines) Gaussian with $\sigma = 0.3L_{\rm av}$ (dotted lines), and triangular having $L_{\rm mn} = 0.5L_{\rm av}$ and $L_{\rm mx} = 2L_{\rm av}$ (dashed lines). The susceptibility rises at low temperature because of the AB effect.

parallel field. Further, the negative contribution present for the magnetic-field range $(L/2\pi l)^2 \lesssim 0.7$ is essentially due to the diamagnetic moment of semiconducting CN's in the parallel field.

Figure 65 shows the zero-field susceptibility of ensembles as a function of temperature. In this figure $L$ means $L_{\rm av}$ for the Gaussian and triangular distributions and it is found that the temperature dependence of susceptibility is essentially given by that of single-shell CN's having the average circumference also. The absolute value of susceptibility gradually decreases with temperature except at low temperatures. The sharp rise at $k_BT \lesssim 0.1\times(4\pi\gamma/3L)$ is again due to the divergent paramagnetic susceptibility of metallic CN's, i.e., a direct manifestation of the AB effect.

The magnetic properties of CN's were recently measured experimentally.[77,79] Figure 66 shows the experimental result of ref. 77 together with the magnetization and differential susceptibility calculated for the rectangular and triangular distribution with $L_{\rm mn} = 22$Å corresponding to the finest CN so far observed and $L_{\rm mx} = 942.5$ Å corresponding to the thickest CN. The calculation can explain the experiments qualitatively, but

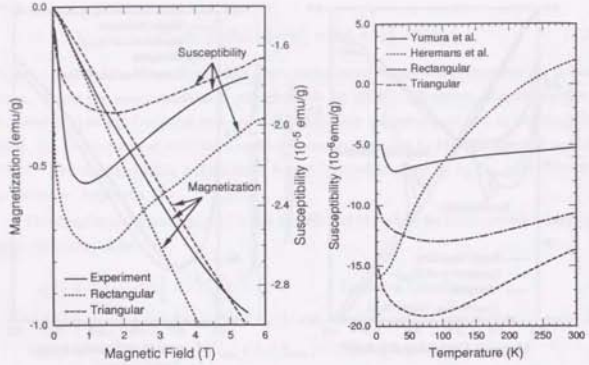


**Fig. 66** (Left) Calculated ensemble average of magnetic moment and differential susceptibility for CN's with rectangular (dotted lines) and triangular (dashed lines) circumference distribution having $L_{\rm mn} = 22$Å and $L_{\rm mx} = 942.5$Å. Solid lines denote the experimental results of magnetization and differential susceptibility.[77]

**Fig. 67** (Right) Ensemble average of susceptibility versus temperature by Yumura *et al.*[78] and Heremans *et al.*[77]. Calculated results are obtained for CN's with rectangular and triangular circumference distribution having $L_{\rm mn} = 22$Å and $L_{\rm mx} = 942.5$Å.

more detailed information on the distribution of CN's is indispensable for more quantitative comparison.

The temperature dependence of the susceptibility was measured also and the results are shown in Fig. 67 including the calculated results for the circumference distribution being rectangular and triangular. The experimental results of Ramirez *et al.*[79] and Heremans *et al.*[77] do not exhibit the increase at low temperatures predicted by the theory (Fig. 65). However, Yumura *et al.*[78] observed an increase of the susceptibility in the range of 0 to 30K in samples of purified nanotubes without other carbon structures.

The susceptibility of bundles of aligned CN's was measured also.[80] However, the experimentally observed susceptibility is larger for the parallel field than for the perpendicular field, quite in contrast to the theoretical prediction shown in Figs. 58 and 59. The origin of this discrepancy is not known.

## 6.3 Summary

The magnetic properties of single and ensembles of CN's have been studied in an effective-mass approximation. The magnetic moment oscillates as a function of $\phi$ with



the period of the magnetic flux quantum $\phi_0$. The phase of the oscillation is opposite between metallic and semiconducting CN's, i.e., for a small flux the moment is in the same direction as the flux in the metallic case and in the opposite direction in the semiconducting case. In both cases the moment does not depend on the circumference.

The susceptibility of a single CN is negative (diamagnetic) and does not depend so much on whether it is metallic or semiconducting. It is proportional to the circumference and becomes infinite in the limit of infinite circumference. This has been understood in conjunction with the susceptibility of a 2D graphite sheet.

The magnetization in a weak field and the susceptibility of single CN's change drastically by carrier doping. However, the magnetization becomes independent of carrier in a strong field where all the carriers exist in well-defined Landau level.

The magnetization and the susceptibility of realistic undoped samples are calculated for three different kinds of the distribution of the circumference; a Gaussian, rectangular, and triangular distributions. The Aharonov-Bohm effect manifests itself as the increase of the differential susceptibility in a weak field. The experimental results by Heremans *et al.*[77] exhibit the characteristic structure and lie between those for the rectangular and triangular distribution. The AB effect also appears as the increase of the susceptibility at low temperatures. The experimental results by Heremans *et al.*[77] and Ramirez *et al.*[79] do not exhibit the increase of susceptibility in a weak field, while that by Yumura *et al.*[78] seems to this characteristic features predicted theoretically.

# Chapter 7

# Summary and Conclusion

In this paper we have studied electronic states, optical absorption, lattice instability, and magnetic properties of carbon nanotubes in magnetic fields in the effective-mass theory.

In Chapter 3 electronic states of CN's have been calculated. The sensitive change of CN's from a metal to a semiconductor depending on its structure is well reproduced in the **k·p** method. The band gap is inversely proportional to the tube diameter and exhibits a drastic change as a function of magnetic flux passing through the cylinder cross-section with the period of the magnetic flux quantum due to the Aharonov-Bohm effect.

In a magnetic field perpendicular to the tube axis, a well defined Landau level is formed at the Fermi energy, which agrees with the result of a tight-binding model in a wide magnetic-field range except in except extremely high fields where the flux passing through the unit cell of a two-dimensional graphite is comparable to the flux quantum, *i.e.* $\sim 4000$T. A slight deviation of the tight-binding results from that in the **k·p** method in weak magnetic fields can be explained by the inclusion of higher order terms in the **k·p** expansion leading to trigonal warping of bands.

In Chapter 4 optical absorption spectra have been calculated in the presence of a magnetic field parallel to the tube axis. A drastic change in the band gap due to the AB effect manifests itself in optical spectra for light polarization parallel to the axis. In the case of perpendicular polarization, the absorption is suppressed strongly by a large depolarization effect. These characteristic features are not modified by carrier doping.

In Chapter 5 we have studied lattice instability toward in-plane Kekulé and out-of-plane distortions is studied. The **k·p** model Hamiltonian with the distortions is given by Dirac's relativistic equation. In the absence of a magnetic field perpendicular to the tube axis, only metallic CN's are unstable against the distortions. The resulting gap equation has been solved analytically in the presence of an AB flux, leading to the conclusion that the Kekulé and out-of-plane distortions cannot coexist. A tight-binding model gives results in excellent agreement with **k·p** results and justifies the **k·p** model Hamiltonian.

The distortion is enhanced drastically by a perpendicular magnetic field for both metallic and semiconducting CN's. A maximum distortion occurs at the top and bottom





of the cylinder surface where electrons form Landau levels in a 2D graphite plane, and its magnitude is independent of the magnetic flux and whether CN's are metallic or semiconducting. A minimum distortion occurs at the side wall region of the cylinder surface where the effective perpendicular magnetic field vanishes.

In Chapter 6 magnetic properties of CN's have been calculated in the **k·p** model. The magnetic moment in a magnetic flux parallel to the tube axis oscillates as a function of the flux and exhibits paramagnetism and diamagnetism for metallic and semiconducting CN's in a weak field, respectively. In a magnetic field perpendicular to the axis, both metallic and semiconducting CN's exhibit a large diamagnetism originated from a 2D graphite sheet.

The paramagnetism of metallic CN's induced by the AB flux manifests itself in the magnetic-field and temperature dependence of the differential susceptibility of ensembles of CN's having various circumference and orientations. The magnetic properties turn out to be strongly dependent on carrier doping.

# Acknowledgments

Over the course of working on this thesis, there have been many people who have helped me along my path. It is great pleasure to acknowledge their contributions

I would like to express my sincerest gratitude to Professor Tsuneya Ando for his continual guidance and encouragement throughout the course of the present work and his critical reading of the manuscript. I thank Professor Nguyen Ai Viet for his collaboration of a part of the thesis. I appreciate Professor Hiroshi Akera, Professor Masahito Ueda, Dr. Hiroyuki Tamura, Dr. Takeshi Inoshita, Mr. Satoru Ishizaka, Dr. Takeshi Nakanishi, Mr. Seiji Uryu, Mr. Ken-ichi Asano, and Mr. Takuji Seri for useful advice and discussions. I express my gratitude to Ms. Shizue Maruyama, who encourage me very heartily. I acknowledges the financial support from the Research Fellowships of the Japan Society for the Promotion of Science for Young Scientists and Texas Instruments Japan Ltd.

Finally I would like to express special gratitude to Aya Takemoto for help and continual encouragement during the master and doctor courses. The author express deepest gratitude to my parents for their support and encouragement for years.

I dedicate this dissertation to my parents and A. Takemoto.



# Appendix A

# Peierls' Phase

In a magnetic field, a translation of an electron is accompanied by a phase factor called the Peierls' phase. In this Appendix we will review this phase.

Introduce a wave function $\Phi_{\mathbf{R}}(\mathbf{r})$ for a nondegenerate level of an atom located at position $\mathbf{R}$. The Schrödinger equation is written as

$$\left[\frac{1}{2m}\left(\mathbf{p}+\frac{e}{c}\mathbf{A}(\mathbf{r})\right)^2+V(\mathbf{r}-\mathbf{R})\right]\Phi_{\mathbf{R}}(\mathbf{r})=\varepsilon\Phi_{\mathbf{R}}(\mathbf{r}). \tag{A1}$$

For a uniform magnetic field, we have $\mathrm{rot}A(\mathbf{r}) = \mathrm{rot}A(\mathbf{r}-\mathbf{R}) = \mathbf{H}$ and consequently $\mathrm{rot}[\mathbf{A}(\mathbf{r})-\mathbf{A}(\mathbf{r}-\mathbf{R})]=0$. Define $\chi_{\mathbf{R}}(\mathbf{r})$ such that

$$\vec{\nabla}\chi_{\mathbf{R}}(\mathbf{r}) = \mathbf{A}(\mathbf{r}) - \mathbf{A}(\mathbf{r}-\mathbf{R}). \tag{A2}$$

It is straightforward to show that the wave function

$$\tilde{\Phi}_{\mathbf{R}}(\mathbf{r}) = \Phi_{\mathbf{R}}(\mathbf{r})\exp\left[\mathrm{i}\frac{e}{c\hbar}\chi_{\mathbf{R}}(\mathbf{r})\right] \tag{A3}$$

satisfies

$$\left[\frac{1}{2m}\left(\mathbf{p}+\frac{e}{c}\mathbf{A}(\mathbf{r}-\mathbf{R})\right)^2+V(\mathbf{r}-\mathbf{R})\right]\tilde{\Phi}_{\mathbf{R}}(\mathbf{r}) = \varepsilon\tilde{\Phi}_{\mathbf{R}}(\mathbf{r}), \tag{A4}$$

*i.e.*, $\tilde{\Phi}_{\mathbf{R}}(\mathbf{r})\propto\Phi_0(\mathbf{r}-\mathbf{R})$. This means

$$\Phi_{\mathbf{R}}(\mathbf{r})=\Phi_0(\mathbf{r}-\mathbf{R})\exp\left[-\frac{\mathrm{i}e}{\hbar c}\chi_{\mathbf{R}}(\mathbf{r})\right]\exp[\mathrm{i}\vartheta(\mathbf{R})], \tag{A5}$$

where $\vartheta(\mathbf{R})$ is any function of $\mathbf{R}$.

For Landau or symmetric gauges in which $\mathbf{A}(\mathbf{r})$ is a linear function of $\mathbf{r}$, we can choose

$$\vec{\nabla}\chi_{\mathbf{R}}(\mathbf{r}) = \mathbf{A}(\mathbf{R}) \quad \text{or} \quad \chi_{\mathbf{R}}(\mathbf{r}) = \mathbf{A}(\mathbf{R})\cdot\mathbf{r}. \tag{A6}$$

Therefore, we have

$$\Phi_{\mathbf{R}}(\mathbf{r})=\Phi_0(\mathbf{r}-\mathbf{R})\exp\left[-\frac{\mathrm{i}e}{\hbar c}\mathbf{A}(\mathbf{R})\cdot(\mathbf{r}-\mathbf{R})\right], \tag{A7}$$

where we have chosen the phase such that $\vartheta(\mathbf{R}) = (e/ch)\mathbf{A}(\mathbf{R})\cdot\mathbf{R}$. As long as the magnetic length $l$ is much larger than the extent of the atomic wave function, effects of the magnetic field can be neglected and we can safely replace $\Phi_0(\mathbf{r}-\mathbf{R})$ by the wave function in the absence of the field.

# Appendix B

# Gap Equations with Infinite Cutoff

It is possible to obtain an analytic expression for $I(\varphi,\Delta)$ for small $\Delta$ and $\varphi$. First, we note that eq. (5.14) can be written as

$$0 = \sum_{n=-\infty}^{\infty}\int_{-\infty}^{\infty} dk \int_{-1/2}^{1/2} dt \frac{g_1\left(|\varepsilon_\varphi^{(-)}(n+t,k,0)|\right)}{|\varepsilon_\varphi^{(-)}(n+t,k,0)|}. \tag{B1}$$

Thus, eq. (5.16) is rewritten as

$$I = \gamma \sum_{n=-\infty}^{\infty}\int_{-\infty}^{\infty} dk \int_{-1/2}^{1/2} dt \left[\frac{g_1\left(|\varepsilon_\varphi^{(-)}(n,k,\Delta)|\right)}{|\varepsilon_\varphi^{(-)}(n,k,\Delta)|} - \frac{g_1\left(|\varepsilon_\varphi^{(-)}(n+t,k,0)|\right)}{|\varepsilon_\varphi^{(-)}(n+t,k,0)|}\right]. \tag{B2}$$

We first separate the summation into

$$I = f(0,\varphi,\delta) + \sum_{n=-1}^{-\infty} f(n,\varphi,\delta) + \sum_{n=1}^{\infty} f(n,\varphi,\delta), \tag{B3}$$

where

$$f(n,\varphi,\delta) = \int_{-\infty}^{\infty} d\tilde{k} \int_{-1/2}^{1/2} dt \left[\frac{g_1\left(\sqrt{\tilde{k}^2+(n+\varphi)^2+\delta^2}\right)}{\sqrt{\tilde{k}^2+(n+\varphi)^2+\delta^2}} - \frac{g_1\left(\sqrt{\tilde{k}^2+(n+\varphi+t)^2}\right)}{\sqrt{\tilde{k}^2+(n+\varphi+t)^2}}\right]. \tag{B4}$$

with $\tilde{k} = Lk/2\pi$ and $\delta = \Delta L/2\pi\gamma$.

Because $f(n,\varphi,\delta)$ decays rapidly for large $n$ and the series converges, we can extend the cutoff to infinity and eliminate the cutoff functions. Thus we have

$$f(n,\varphi,\delta) = \int_{-\infty}^{\infty} d\tilde{k} \int_{-1/2}^{1/2} dt \left[\frac{1}{\sqrt{\tilde{k}^2+(n+\varphi)^2+\delta^2}} - \frac{1}{\sqrt{\tilde{k}^2+(n+\varphi+t)^2}}\right]. \tag{B5}$$

For small $\delta$ and $\varphi$, the leading contribution comes from the first term $n=0$, which is calculated as

$$f(0,\varphi,\delta) = -\ln(\varphi^2+\delta^2) - 2\ln 2 - 2. \tag{B6}$$

For $n \neq 0$, we can neglect $\delta$ and $\varphi$ safely and get

$$f(n,\varphi,\delta) \approx -2\Big[1-\Big(n+\frac{1}{2}\Big)\ln\Big(1+\frac{1}{2n}\Big)+\Big(n-\frac{1}{2}\Big)\ln\Big(1-\frac{1}{2n}\Big)\Big] = -\sum_{l=1}^{\infty}\frac{1}{l(2l+1)2^{2l}}\frac{1}{n^{2l}}. \tag{B7}$$

Therefore, the integral becomes

$$I(\varphi,\Delta) = -\ln(\varphi^2+\delta^2)-2\ln 2-2-2C_0, \tag{B8}$$

where

$$C_0 = \sum_{l=1}^{\infty}\frac{\zeta(2l)}{l(2l+1)2^{2l}} \approx 0.1445972, \tag{B9}$$

with $\zeta(p)$ is Riemann's zeta-function, defined as

$$\zeta(p) = \sum_{n=1}^{\infty}\frac{1}{n^p}. \tag{B10}$$

# Appendix C

# Force Constant for Graphite Sheet

For graphite sheet the effective force constant which comes from electronic states can be calculated by the second order perturbation. We first perform a unitary transformation for the Hamiltonian (5.30) to diagonalize the non-perturbative part:

$$\begin{array}{c} \\ \Gamma^- \\ \Gamma^+ \\ \mathrm{K}^- \\ \mathrm{K}^+ \\ \mathrm{K}'^- \\ \mathrm{K}'^+ \end{array}\!\!\begin{array}{c} \begin{array}{cccccc} \Gamma^- & \Gamma^+ & \mathrm{K}^- & \mathrm{K}^+ & \mathrm{K}'^- & \mathrm{K}'^+ \end{array} \\ \begin{pmatrix} -\gamma_0|R| & 0 & -\alpha u\xi_1 & \alpha u\xi_2 & -\alpha u\xi_3 & \alpha u\xi_4 \\ 0 & \gamma_0|R| & -\alpha u\xi_2 & \alpha u\xi_1 & -\alpha u\xi_4 & \alpha u\xi_3 \\ -\alpha u\xi_1^* & -\alpha u\xi_2^* & -\gamma_0|S| & 0 & -\alpha u\xi_5 & \alpha u\xi_6 \\ \alpha u\xi_2^* & \alpha u\xi_1^* & 0 & \gamma_0|S| & -\alpha u\xi_6 & \alpha u\xi_5 \\ -\alpha u\xi_3^* & -\alpha u\xi_4^* & -\alpha u\xi_5^* & -\alpha u\xi_6^* & -\gamma_0|T| & 0 \\ \alpha u\xi_4^* & \alpha u\xi_3^* & \alpha u\xi_6^* & \alpha u\xi_5^* & 0 & \gamma_0|T| \end{pmatrix} \end{array}, \tag{C1}$$

with

$$\xi_1 = \frac{R^*T}{2|R|}+\frac{T^*S}{2|S|}, \quad \xi_2 = \frac{R^*T}{2|R|}-\frac{T^*S}{2|S|}, \quad \xi_3 = \frac{R^*S}{2|R|}+\frac{S^*T}{2|T|}, \\ \xi_4 = \frac{R^*S}{2|R|}-\frac{S^*T}{2|T|}, \quad \xi_5 = \frac{S^*R}{2|S|}+\frac{R^*T}{2|T|}, \quad \xi_6 = \frac{S^*R}{2|S|}-\frac{R^*T}{2|T|}, \tag{C2}$$

where $(-)$ and $(+)$ mean valence and conduction bands, respectively.

Because the trace of a matrix is invariant under any unitary transformation, energy shifts due to interaction among valence-band states do not contribute to the total energy shift and those due to interactions between valence and conduction bands should be calculated. It is clear that the energy shift is $O(u^2)$ except in the vicinity of the $\Gamma$ point where valence and conduction bands are degenerate. At the $\Gamma$ point, the energy changes to the first order in $u$, but the vanishing density of states at the Fermi level in 2D graphite makes this contribution negligibly small. Therefore the second order perturbation is applicable all over the first Brillouin zone. The electronic contribution to the force constant $K_e$ is obtained through the relation $\delta E = NK_e u^2/2$ in terms of the energy shift $\delta E$ given by

$$\delta E = -\frac{4\alpha^2u^2}{\gamma_0}\frac{AL}{(2\pi)^2}\int \mathrm{d}^2k\Big(\frac{|\xi_2|^2}{|R|+|S|}+\frac{|\xi_4|^2}{|R|+|T|}+\frac{|\xi_6|^2}{|S|+|T|}\Big). \tag{C3}$$

where the integral is carried out over the first Brillouin zone in the distorted lattice. Actual numerical calculation is performed by introducing a small imaginary number in the denominator and gives $K_\alpha = -5.81\alpha^2/\gamma_0$.

# Appendix D
# Phonon Modes of 2D Graphite

In this appendix in-plane phonon modes are discussed using a simple model in which a force constant is nonzero for only the nearest-neighbor stretching motion. The Lagrangian for phonon is given by

$$\mathcal{L} = \frac{M}{2}\sum_{i=\mathrm{A,B}}\sum_{\mathbf{R}_i}|\dot{\mathbf{u}}_i(\mathbf{R}_i)|^2 - \frac{K}{2}\sum_{\mathbf{R}_\mathrm{A}}\sum_{l=1,2,3}\left\{[\mathbf{u}_\mathrm{A}(\mathbf{R}_\mathrm{A})-\mathbf{u}_\mathrm{B}(\mathbf{R}_\mathrm{A}-\vec{r}_l)]\cdot\frac{\vec{r}_l}{|\vec{r}_l|}\right\}^2, \tag{D1}$$

where $M$ is the mass of carbon atoms, $K$ is the force constant, and $\mathbf{u}$ is the displacement of carbon atoms. From Euler's equation

$$\frac{\mathrm{d}}{\mathrm{d}t}\frac{\partial\mathcal{L}}{\partial\dot{u}_i^\mu(\mathbf{R}_i)} - \frac{\partial\mathcal{L}}{\partial u_i^\mu(\mathbf{R}_i)} = 0, \quad (\mu = x, y), \tag{D2}$$

we get equations of motion

$$\begin{cases} M\ddot{u}^\mu_{\mathbf{R}_\mathrm{A}} = -K\sum_l[\mathbf{u}_\mathrm{A}(\mathbf{R}_\mathrm{A})-\mathbf{u}_\mathrm{B}(\mathbf{R}_\mathrm{A}-\vec{r}_l)]\cdot\dfrac{\vec{r}_l}{|\vec{r}_l|}\dfrac{r_l^\mu}{|\vec{r}_l|}, \\ \vec{r}_l r_l^\mu/|\vec{r}_l|^2, \\ M\ddot{u}^\mu_{\mathbf{R}_\mathrm{B}} = -K\sum_l[\mathbf{u}_\mathrm{A}(\mathbf{R}_\mathrm{B}+\vec{r}_l)-\mathbf{u}_\mathrm{B}(\mathbf{R}_\mathrm{B})]\cdot\dfrac{\vec{r}_l}{|\vec{r}_l|}\dfrac{-r_l^\mu}{|\vec{r}_l|}. \end{cases} \tag{D3}$$

Substituting $u_i^\mu(\mathbf{R}_i,t) = u_i^\mu(\mathbf{k})\exp(\mathrm{i}\mathbf{k}\cdot\mathbf{R}_i - \mathrm{i}\omega t)$ into (D3), we get the dynamical matrix

$$a\sqrt{\frac{K}{M}}\begin{array}{c} \\ \\ \\ \\ \end{array}\begin{array}{c} \begin{array}{cccc} u_\mathrm{A}^x & u_\mathrm{A}^y & u_\mathrm{B}^x & u_\mathrm{B}^y \end{array} \\ \begin{pmatrix} 3/2 & 0 & D_1 & D_2 \\ 0 & 3/2 & D_2 & D_3 \\ D_1^* & D_2^* & 3/2 & 0 \\ D_2^* & D_3^* & 0 & 3/2 \end{pmatrix} \end{array}, \tag{D4}$$

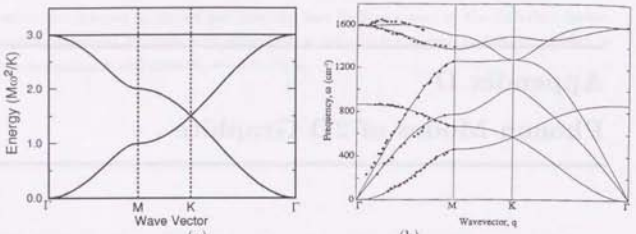


**Fig. 68** (a) Calculated phonon dispersions of in-plane modes given by using only one force constant for bond stretching between nearest-neighbor atoms. (b) Calculated phonon dispersions of in-plane and out-of-plane modes given by using four bond stretching and four bond bending force constants. Dots denotes an experimental data.

with

$$D_1 = -\frac{3}{2}\exp\left[\mathrm{i}\frac{a}{2\sqrt{3}}k_y\right]\cos\left(\frac{a}{2}k_x\right),$$
$$D_2 = -\mathrm{i}\frac{\sqrt{3}}{2}\exp\left[\mathrm{i}\frac{a}{2\sqrt{3}}k_y\right]\sin\left(\frac{a}{2}k_x\right), \qquad \text{(D5)}$$
$$D_3 = -\exp\left[-\mathrm{i}\frac{a}{\sqrt{3}}k_y\right] - \frac{1}{2}\exp\left[\mathrm{i}\frac{a}{2\sqrt{3}}k_y\right]\cos\left(\frac{a}{2}k_x\right).$$

The dispersions of the four in-plane modes given by eq. (D4) are shown in Fig. 68 (a). Since the force constants for bond bending are neglected, two branches with $\omega = 0$ and $\sqrt{3}a\sqrt{K/M}$ are independent of the wave vector. Figure 68 (b) exhibits calculated phonon dispersion curves of a 2D graphite using four bond stretching and four bond bending force constants.[81] Two dispersions crossing in the lowest energy at the K point are the branches of out-of-plane mode. The dots denote experimental data.

The eigen vectors $(\mathbf{e}_\mathrm{A}, \mathbf{e}_\mathrm{B})$ at $\mathrm{K}' = (4\pi/3a, 0)$ are obtained as

$$\begin{pmatrix} e^x_\mathrm{A} \\ e^y_\mathrm{A} \\ e^x_\mathrm{B} \\ e^y_\mathrm{B} \end{pmatrix} = \frac{1}{2}\begin{pmatrix} -\mathrm{i} \\ -1 \\ -\mathrm{i} \\ 1 \end{pmatrix}, \quad \frac{1}{2}\begin{pmatrix} -\mathrm{i} \\ 1 \\ \mathrm{i} \\ 1 \end{pmatrix}, \quad \frac{1}{2}\begin{pmatrix} 1 \\ \mathrm{i} \\ 1 \\ -\mathrm{i} \end{pmatrix}, \quad \frac{1}{2}\begin{pmatrix} 1 \\ \mathrm{i} \\ -1 \\ -\mathrm{i} \end{pmatrix}. \qquad \text{(D6)}$$
$$\omega/a\sqrt{K/M} = \quad \sqrt{3}, \qquad \sqrt{3/2}, \qquad \sqrt{3/2}, \qquad 0$$

Displacement of carbon atoms are given by taking the real part of $\mathbf{u}_i(\mathbf{R}_i)$ and that of each mode at K' point are shown in Fig. 69. The pattern for $\omega = \sqrt{3}a\sqrt{K/M}$ in Fig. 69 (a) is so-called the Kekulé structure which consists of a network of hexagons with the alternating short and long bonds like in the classical benzene molecule. The modes with $\omega = \sqrt{3/2}a\sqrt{K/M}$ are two-fold degenerate. The corresponding lattice distortion for the



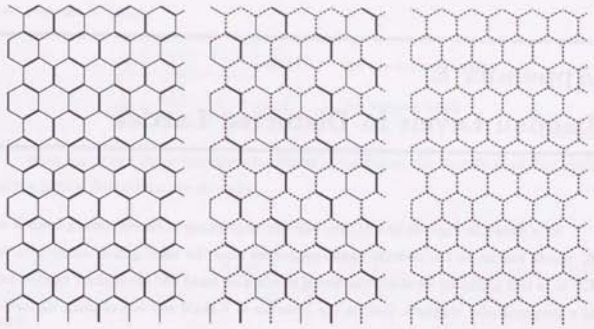


**Fig. 69** Displacement patterns of atoms for in-plane phonon modes having wave vector $\mathbf{K}$ and $\mathbf{K}'$ with $\omega = \sqrt{3}a\sqrt{K/M}$ (a), $\omega = \sqrt{3/2}a\sqrt{K/M}$ (b) and $\omega = 0$ (c). Thick and normal lines show larger and smaller distorted bonds, respectively, and dotted lines show undistorted bonds. Distortion (a) corresponds to the Kekulé pattern.

eigen vector $(-\mathrm{i}/2, 1/2, \mathrm{i}/1, 1/2)$ is shown in Fig. 69 (b). The distortion for another eigen vector is obtained by rotating each vector by $\pi/2$ clockwise. For the phonon mode of $\omega = 0$ there is no bond length change as is shown in Fig. 69 (c).

# Appendix E
# Landau Levels in Distorted Lattice

As is shown in Figs. 50 and 51, the two-fold degeneracy of bands coming from K and K' points remain in the Kekulé distortion except near the band gap of semiconducting CN's. In this appendix we study the lowest conduction band and the highest valence band in a perpendicular magnetic field in the presence of Kekulé and out-of-plane distortions analytically.

From eqs. (3.38) and (3.39), the wave functions of the lowest Landau level near the K point are given by

$$\begin{pmatrix} 0 \\ h_0(x-X_+) \end{pmatrix} \quad \text{and} \quad \begin{pmatrix} h_0(x-X_-) \\ 0 \end{pmatrix}, \tag{E1}$$

and the wave functions near the K' point

$$\begin{pmatrix} h_0(x-X_+) \\ 0 \end{pmatrix} \quad \text{and} \quad \begin{pmatrix} 0 \\ h_0(x-X_-) \end{pmatrix}. \tag{E2}$$

The next order term in Hamiltonian eqs. (3.38) and (3.39) around $X_+$ is written as

$$\mathcal{H}' = \begin{pmatrix} 0 & \mp\frac{i}{2}\left(\frac{2\pi}{L}\right)^2 (x-X_+)^2 k \\ \pm\frac{i}{2}\left(\frac{2\pi}{L}\right)^2 (x-X_+)^2 k & 0 \end{pmatrix}, \tag{E3}$$

with upper and lower signs corresponding to near the K and the K' points, respectively. For the term around $X_-$ is given by the replacement of $X_+$ by $X_-$. The wave functions near the K point under this perturbation is given by

$$\begin{aligned} &\frac{1}{\sqrt{2}}\begin{pmatrix} -ih_0(x-X_-) \\ h_0(x-X_+) \end{pmatrix} \mathrm{sgn}(k) && \text{for conduction band,} \\ &\frac{1}{\sqrt{2}}\begin{pmatrix} ih_0(x-X_-) \\ h_0(x-X_+) \end{pmatrix} \mathrm{sgn}(k) && \text{for valence band,} \end{aligned} \tag{E4}$$





and near the K' point

$$\begin{aligned} &\frac{1}{\sqrt{2}}\begin{pmatrix} h_0(x-X_+) \\ -ih_0(x-X_-) \end{pmatrix} \mathrm{sgn}(k) && \text{for conduction band,} \\ &\frac{1}{\sqrt{2}}\begin{pmatrix} h_0(x-X_+) \\ ih_0(x-X_-) \end{pmatrix} \mathrm{sgn}(k) && \text{for valence band.} \end{aligned} \tag{E5}$$

With use of the above four wave functions as the bases, the Hamiltonian $\mathcal{H}_\Delta$ related to the lattice distortions are given by

$$\mathcal{H}_\Delta = \begin{matrix} \\ \mathrm{K} \\ \mathrm{K}' \end{matrix} \begin{matrix} \begin{matrix} \mathrm{K} & \mathrm{K}' \end{matrix} \\ \begin{pmatrix} \mathcal{H}_{\Delta_2} & \mathcal{H}_{\Delta_1} \\ \mathcal{H}^*_{\Delta_1} & \mathcal{H}_{\Delta_2} \end{pmatrix} \end{matrix}, \tag{E6}$$

with

$$\mathcal{H}_{\Delta_1} = \begin{matrix} \\ \mathrm{K}^{(c)} \\ \mathrm{K}^{(v)} \end{matrix} \begin{matrix} \begin{matrix} \mathrm{K}'^{(c)} & \mathrm{K}'^{(v)} \end{matrix} \\ \begin{pmatrix} -D_1(X_-)+D_1(X_+) & D_1(X_-)+D_1(X_+) \\ D_1(X_-)+D_1(X_+) & -D_1(X_-)+D_1(X_+) \end{pmatrix} \end{matrix}, \tag{E7}$$

and

$$\mathcal{H}_{\Delta_2} = \begin{matrix} \\ \mathrm{K}^{(c)} \\ \mathrm{K}^{(v)} \end{matrix} \begin{matrix} \begin{matrix} \mathrm{K}^{(c)} & \mathrm{K}^{(v)} \end{matrix} \\ \begin{pmatrix} D_2(X_-)-D_2(X_+) & -D_2(X_-)-D_2(X_+) \\ -D_2(X_-)-D_2(X_+) & D_2(X_-)-D_2(X_+) \end{pmatrix} \end{matrix}, \tag{E8}$$

where + and − represent conduction and valence bands, respectively, and $D_{1,2}(X_\pm)$ are given by

$$D_{1,2}(X_\pm) = \frac{1}{2}\int_0^L \mathrm{d}x h_0^2(x-X_\pm)\Delta_{1,2}(x). \tag{E9}$$

The Hamiltonian in the absence of distortions are written as

$$\mathcal{H}_0 = \begin{matrix} \\ \mathrm{K} \\ \mathrm{K}' \end{matrix} \begin{matrix} \begin{matrix} \mathrm{K} & \mathrm{K}' \end{matrix} \\ \begin{pmatrix} \varepsilon_0\sigma_z & 0 \\ 0 & \varepsilon_0\sigma_z \end{pmatrix} \end{matrix}, \tag{E10}$$

where $\varepsilon_0$ becomes zero when a well-defined Landau level corresponding to that in a 2D graphite plane is formed.

Let us consider only the Kekulé distortion. For metallic CN's there is no phase of $\Delta_1$ and its absolute values at $X_+$ and $X_-$ are the same with each other as is shown in Figs. 48 and 49. Thus $D_1(X_\pm)$ has the relation of

$$D_1(X_+) = D_1(X_-) \equiv D_1(X), \tag{E11}$$

and energy levels are obtained as

$$\varepsilon = \pm\sqrt{\varepsilon_0^2 + |2D_1(X)|^2}, \tag{E12}$$

where each level is two-fold degenerate. It is noted that the degeneracy is not lifted even for $\varepsilon_0 \neq 0$.

From Figs. 48 and 49 it is found that $D_1(X_\pm)$ for semiconducting CN's has the relation of

$$D_1(X_+) = |D_1(X)| \exp(\mathrm{i}\theta) \quad \text{and} \quad D_1(X_-) = |D_1(X)| \exp\left(\mathrm{i}\frac{\nu\pi}{3} - \mathrm{i}\theta\right), \tag{E13}$$

where $\theta$ is the phase of $\Delta_1(X_+)$ and we approximate that the phase is constant over the width of wave function $h_0(x - X_\pm)$. In the range of $\varepsilon_0 = 0$ the energy levels are obtained as

$$\varepsilon = \pm|2D_1(X)|, \tag{E14}$$

where each level is two-fold degenerate. For $\varepsilon_0 \neq 0$, however, there are four different energy levels are obtained. This corresponds to the lifting of degeneracy for semiconducting CN's near the band gap as is exhibited in Fig. 50 (b) and Fig. 51.

For out-of-plane distortion, there is no phase of $\Delta_2$ for both metallic and semiconducting CN's because of the absence of extra phase in the boundary condition given in eq. (5.58). Thus, the relation of $D_2(X_\pm)$ is given by

$$D_2(X_+) = D_2(X_-) \equiv D_2(X), \tag{E15}$$

and energy levels are obtained as

$$\varepsilon = \pm\sqrt{\varepsilon_0^2 + |2D_2(X)|^2}, \tag{E16}$$

where each level is two-fold degenerate.

Since the spatial extent of the Landau wave function $h_0$ decreases with magnetic field, in high magnetic field $D_{1,2}$ is approximated as

$$D_{1,2}(X_\pm) \approx \frac{1}{2}\Delta_{1,2}(X_\pm). \tag{E17}$$

Therefore the energy level is determined by the value of the gap parameter at the center of the cyclotron motion.

# Appendix F
# Infinite Cutoff on Magnetic Properties

It is possible to eliminate the cutoff function $g_1$ for both magnetic moment in a parallel magnetic field and susceptibility in a perpendicular magnetic field. Let us first consider the magnetic moment in a magnetic field parallel to the tube axis. Equation (6.11) can be rewritten as

$$W_1(\varphi) = \frac{1}{2\pi}\sum_{n=-\infty}^{+\infty}\frac{1}{h}f[h(n+\varphi)], \tag{F1}$$

with $h = 2\pi\gamma/L\varepsilon_c$ and

$$f(x) = \int_0^\infty \mathrm{d}y\, \frac{x}{\sqrt{x^2+y^2}}\, g_1(\sqrt{x^2+y^2}). \tag{F2}$$

We note that $f(x)$ is an odd function of $x$ and decays rapidly but smoothly for $|x| \gg 1$. For small $x$, the leading contribution comes from the region $0 < y < \delta$ with $\delta \lesssim 1$ and is given by

$$f(x) \approx \int_0^\delta \mathrm{d}y\, \frac{x}{\sqrt{x^2+y^2}} \approx -x \ln\frac{|x|}{2\delta} \approx -x\ln|x|. \tag{F3}$$

This logarithmic singularity of $f(x)$ at the origin dominates the magnetic moment in the limit $\varepsilon_c \to \infty$ or $h \to 0$ as is shown below.

We separate the summation over $n$ into three regions: $n \leq n_1$, $n_1+1 \leq n \leq n_2-1$, and $n \geq n_2$, with

$$n_1 < -\varphi, \quad -\varphi < n_2, \quad |n_1+\varphi| \ll \frac{1}{h}, \quad \text{and} \quad |n_2+\varphi| \ll \frac{1}{h}. \tag{F4}$$

Noting the antisymmetry of $f(x)$ around $x = 0$, we have

$$2\pi W_1(\varphi) = \sum_{n=n_1+1}^{n_2-1}\frac{1}{h}f[h(n+\varphi)] + \sum_{n=0}^{\infty}\frac{1}{h}\Big(f[h(n+n_2+\varphi)] - f[h(n-n_1-\varphi)]\Big). \tag{F5}$$

In the first term we can use Eq. (F3). For the second term, we shall use the following

Euler-Maclaurin formula which can easily be proved by a partial integration:

$$\sum_{n=0}^{\infty} g(a+nh) = \frac{1}{h}\int_a^{\infty} \mathrm{d}x\, g(x) + \frac{1}{2}g(a) + \frac{h^2}{2}\int_0^1 \mathrm{d}t\, t(1-t)\sum_{n=0}^{\infty} g^{(2)}[a+h(n+t)], \tag{F6}$$

where $g^{(2)}$ is the second derivative of $g$. We then have

$$\begin{aligned} 2\pi W_1(\varphi) = &-\sum_{n=n_1+1}^{n_2-1}(n+\varphi)\ln|n+\varphi| - \sum_{n=n_1+1}^{n_2-1}(n+\varphi)\ln h \\ &+ \frac{1}{h^2}\int_{h(n_2+\varphi)}^{h(-n_1-\varphi)} \mathrm{d}x\, f(x) + \frac{1}{2h}\Big(f[h(n_2+\varphi)] - f[h(-n_1-\varphi)]\Big) \\ &+ \frac{h}{2}\int_0^1 \mathrm{d}t\, t(1-t)\sum_{n=0}^{\infty}\Big(f^{(2)}[h(n+n_2+\varphi+t)] - f^{(2)}[h(n-n_1-\varphi+t)]\Big). \end{aligned} \tag{F7}$$

For small $h$, we can substitute the approximate expression (F3) except in the last term. All terms proportional to $\ln h$ cancel out with each other. In the last term containing the summation over $n$ from 0 to $\infty$, we introduce a cutoff $n_c \sim \beta/h$ with $\beta$ being a parameter of the order of unity and replace the summation over $n$ for $n > n_c$ by an integration. It turns out that the contribution coming from the integral can be safely neglected for small $h$. In the summation $0 \le n \le n_c$, on the other hand, we can use Eq. (F3). Then, the cutoff $n_c$ can be extended to infinity in the final expression, because the series converges very rapidly. In this way, the expression without the cutoff parameters $\varepsilon_c$ and $\alpha$ becomes

$$\begin{aligned} 2\pi W_1(\varphi) = &-\sum_{n=n_1+1}^{n_2-1}(n+\varphi)\ln|n+\varphi| \\ &-\frac{1}{2}\Big[(n_1+\varphi)(n_1+1+\varphi)\ln|n_1+\varphi| - \frac{1}{2}(n_1+\varphi)^2 \\ &\quad -(n_2+\varphi)(n_2-1+\varphi)\ln|n_2+\varphi| + \frac{1}{2}(n_2+\varphi)^2\Big] \\ &+\frac{1}{2}(n_1+n_2+2\varphi)\sum_{n=0}^{\infty}\int_0^1 \mathrm{d}t\,\frac{t(1-t)}{(n-n_1-\varphi+t)(n+n_2+\varphi+t)}. \end{aligned} \tag{F8}$$

It should be noted that the moment given by the above equation is independent of the choice of $n_1$ and $n_2$. In the vicinity of $\varphi = j$, we have immediately

$$W_1(\varphi) \approx -\frac{1}{2\pi}(\varphi-j)\ln|\varphi-j| \quad (|\varphi-j| \ll 1). \tag{F9}$$

Therefore, the moment itself vanishes but its derivative diverges logarithmically (positive infinite) at $\varphi = j$.

For the susceptibility corresponding to a perpendicular magnetic field, the cutoff



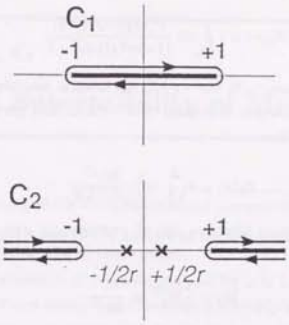


**Fig. 70** Contours $C_1$ and $C_2$ in the complex $z$ plane. The contribution from the pole at $z = \pm 1/2r$ is pure imaginary and can be neglected.

function can be eliminated easily by the use of a Fourier-series expansion. We have

$$W_2(\varphi) = \frac{1}{2}W_2^{(0)} + \sum_{p=1}^{\infty} W_2^{(p)}\cos(2\pi p\varphi), \tag{F10}$$

with

$$W_2^{(p)} = 2\int_0^1 \mathrm{d}\varphi\, W_2(\varphi)\,\cos(2\pi p\varphi). \tag{F11}$$

Then, the summation over $n$ in $W_2(\varphi)$ and the integration over $\varphi$ in the above can be converted into a single integration and

$$\begin{aligned} W_2^{(p)} &= \frac{1}{\pi^4}\iint_{-\infty}^{+\infty} \mathrm{d}x\mathrm{d}y\,\frac{\sqrt{x^2+y^2}}{1-4x^2}\cos(2\pi px)\, g_1\big(h\sqrt{x^2+y^2}\big) \\ &= \frac{1}{\pi^4}\int_0^{\infty} \mathrm{d}r\; R_p(r)\, g_1(hr), \end{aligned} \tag{F12}$$

with

$$R_p(r) = \int_0^{2\pi} \mathrm{d}\theta\;\frac{r^2\cos(2\pi pr\cos\theta)}{1-4r^2\cos^2\theta}. \tag{F13}$$

A principal value should be taken at singularities.

The $\theta$ integration is converted into a contour integral along $C_1$ shown in Fig. 70.

$$R_p(r) = \mathrm{i} \oint_{C_1} \mathrm{d}z \, \frac{r^2 \exp(-2\pi \mathrm{i} p r z)}{(1-4r^2z^2)\sqrt{z^2-1}}. \tag{F14}$$

Let us first consider the case $p=0$. For $r>1/2$ the integral vanishes identically, because $C_1$ is converted into the integral at infinity. For $r<1/2$, it is given by the residues at $z=\pm 1/2r$. Therefore, we have

$$R_0(r) = \theta\Big(\frac{1}{2}-r\Big)\frac{2\pi r^2}{\sqrt{1-4r^2}}, \tag{F15}$$

where $\theta(t)$ is the step function defined as $\theta(t)=1$ $(t>0)$ and $\theta(t)=0$ $(t<0)$. Replacing $g_1(hr)$ by unity, we have

$$\tilde{W}_2 = \frac{1}{2}W_2^{(0)} = \frac{1}{32\pi^2}. \tag{F16}$$

Let us next consider the case $p>0$. We first transform the contour $C_1$ into $C_2$ shown in Fig. 70 for $r>1/2$. Note that the poles at $z=\pm 1/2r$ give a pure imaginary and can be neglected. Then, we have

$$R_p(r) = \mathrm{i} \oint_{C_2} \mathrm{d}z \, \frac{r^2 \exp(-2\pi \mathrm{i} p r z)}{(1-4r^2z^2)\sqrt{z^2-1}} = -4\int_1^\infty \mathrm{d}t \, \frac{r^2 \sin(2\pi p r t)}{(4r^2t^2-1)\sqrt{t^2-1}}. \tag{F17}$$

For $r \gg 1/2$, the integrand oscillates rapidly and the main contribution comes from the region $|t| \sim 1$. After replacing $4r^2t^2-1$ by $4r^2-1 \approx 4r^2$ and then converting the contour back to $C_1$ and then to the integration over $\theta$, we have

$$R_p(r) \approx -\frac{1}{4}\int_0^{2\pi} \mathrm{d}\theta \, \cos(2\pi p r \cos\theta) = -\frac{\pi}{2} J_0(2\pi p r), \tag{F18}$$

where $J_0(t)$ is the Bessel function. Because the Bessel function oscillates rapidly for large $r$ and its integral for large $r$ converges fast, we can safely replace $g_1(hr)$ by unity. For small $r$, we can immediately obtain $R_p(r) \approx 2\pi r^2 J_0(2\pi p r)$. It is expected, therefore, that the resulting integral $W_2^{(p)}$ decays rapidly for $p \gg 1$ and the Fourier series converges.

# Appendix G
# Divergent Susceptibility of Metallic CN's

The metallic undoped CN's exhibit divergent susceptibility in the parallel direction to the tube axis at zero temperature. In this appendix we will study the susceptibility of metallic CN's as a function of temperature.

The leading contribution of magnetic moment for $\varphi \ll 1$ at zero temperature comes from the vicinity of Fermi energy[63] and the the susceptibility at zero temperature is given by

$$\chi_{\mathrm{M}}^{\parallel}(\mu) \sim -\chi^* \frac{L}{a}\cdot\frac{1}{2\pi^4}\ln\Big|\frac{\mu}{\gamma k_{\mathrm{c}}}\Big|. \tag{G1}$$

The susceptibility is logarithmically divergent with respect to the chemical potential. The susceptibility of metallic CN's of $\mu=0$ at low temperature is obtained as

$$\begin{aligned}\chi_{\mathrm{M}}^{\parallel}(T) &= \int_{-\infty}^{\infty} \mathrm{d}\varepsilon \chi_{\mathrm{M}}^{\parallel}(\varepsilon)\Big(-\frac{\partial}{\partial\varepsilon}\theta(\varepsilon)\Big) \\ &\sim -\chi^* \frac{L}{a}\frac{1}{2\pi^4}\ln\frac{k_{\mathrm{B}}T}{\gamma k_{\mathrm{c}}}.\end{aligned} \tag{G2}$$

Thus eq. (6.26) is valid for finite temperature, because the susceptibility is not infinite.

The critical temperature where the susceptibility of realistic samples becomes negative, is given from eq. (6.28). For $\rho(L)$ being the delta function, we get the critical temperature as

$$\begin{aligned}k_{\mathrm{B}}T &= \frac{1}{2}\gamma k_{\mathrm{c}} \exp\Big[-4\pi^4 \frac{\chi_{\mathrm{M}}^{\perp}+\chi_{\mathrm{S}}^{\parallel}+2\chi_{\mathrm{S}}^{\perp}}{\chi^*(L/a)}\Big] \\ &\sim 6.0\times 10^{-8}\gamma k_{\mathrm{c}},\end{aligned} \tag{G3}$$

The critical temperature is inverse proportional to $L$ because of $k_{\mathrm{c}} \sim 2\pi/L$. Even for CN's with the smallest circumference so far reported, the band gap is a few eV and the critical temperature is less than 10 mK.

# References


1 S. Iijima: Nature (London) **354**, 56 (1991).
2 T.W. Ebbesen, P.M. Ajayan, H. Hiura, and K. Tanigaki: Nature (London) **367**, 519 (1994).
3 F.Ikazaki, S. Ohshima, K. Uchida, Y. Kuriki, H. Hayakawa, M. Yumura, K. Takahashi, and K. Tojima: Carbon **32**, 1539 (1994).
4 M. Yumura, K. Ushida, H. Nino, S. Ohshima, Y. Kuriki, K. Yase, and F. Ikazaki: Mat. Res. Soc. Symp. Proc. Vol.349, p231
5 S. Iijima and T. Ichihashi: Nature (London) **363**, 603 (1993).
6 D.S. Bethune, C.H. Kiang, M.S. de Vries, G. Gorman, R. Savoy, J. Vazquez, and R. Beyers: Nature (London) **363**, 605 (1993).
7 N. Hamada, S. Sawada, and A. Oshiyama: Phys. Rev. Lett. **68**, 1579 (1992).
8 J.W. Mintmire, B.I. Dunlap, and C.T. White, Phys. Rev. Lett. **68**, 631 (1992).
9 R. Saito, M. Fujita, G. Dresselhaus, and M.S. Dresselhaus: Phys. Rev. B **46**, 1804 (1992).
10 R. Saito, M. Fujita, G. Dresselhaus, and M.S. Dresselhaus: Appl. Phys. Lett. **60**, 2204 (1992).
11 M.S. Dresselhaus, G. Dresselhaus, and R. Saito: Phys. Rev. B **45**, 6234 (1992).
12 M.S. Dresselhaus, G. Dresselhaus, R. Saito, and P.C. Eklund: *Elementary Excitations in Solids*, ed. J.L. Birman, C. Sebenne, and R.F. Wallis (Elsevier Science Publishers B.V., Amsterdam, 1992) p. 387.
13 K. Tanaka, K. Okahara, M. Okada, and T. Yamabe: Chem. Phys. Lett. **191**, 469 (1992).
14 Y.D. Gao and W.C. Herndon: Mol. Phys. **77**, 585 (1992).
15 D.H. Robertson, D.W. Berenner, and J.W. Mintmire: Phys. Rev. B **45**, 12592 (1992).
16 R.A. Jishi, M.S. Dresselhaus, and G. Dresselhaus: Phys. Rev. B **47**, 16671 (1993).
17 C.T. White, D.C. Robertson, and J.W. Mintmire: Phys. Rev. B **47**, 5485 (1993).
18 R. Saito, G. Dresselhaus, and M.S. Dresselhaus: J. Appl. Phys. **73**, 494 (1993).
19 X. Blase, L.X. Benedict, E.L. Shirley, and S.G. Louie: Phys. Rev. Lett. **72**, 1878 (1994).
20 T.W. Ebbesen and P.M. Ajayan: Nature (London) **358**, 220 (1992).
21 S. Iijima, P.M. Ajayan, and T. Ichihashi: Phys. Rev. Lett. **69**, 3100 (1992)
22 A. Maiti, C.J. Brabec, C.M. Roland, and J. Bernholc: Phys. Rev. Lett. **73**, 2468 (1994).
23 R. Saito, G. Dresselhaus, and M.S. Dresselhaus: Chem. Phys. Lett. **195**, 537 (1992).
24 M. Ge and K. Satler: Science **260**, 515 (1993).
25 M. Ge and K. Sattler: J. Phys. Chm. Solids. **54**, 1871 (1993).
26 M. Endo, K. Takeuchi, S. Igarashi, K. Kobori, M. Shiraishi, and W. Kroto: J. Phys. Chm. Solids. **54**, 1841 (1993).
27 S. Iijima, T. Ichihashi, and Y. Ando: Nature (London) **356**, 776 (1992).







28 P.M. Ajayan, T. Ichihashi, and S. Iijima: Chem. Phys. Lett. **202**, 384 (1993).
29 S.C. Tsang, P.F.J. Harris, and M.L.H. Green: Nature (London) **362**, 520 (1993).
30 P.M. Ajayan, T.W. Ebbesen, T. Ichihashi, S. Iijima, K. Tanigaki, and H. Hiura: Nature (London) **362**, 522 (1993).
31 R. Tamura and M. Tsukada: Phys. Rev. B **49**, 7697 (1994).
32 R. Tamura and M. Tsukada: Phys. Rev. B **52**, 6015 (1994).
33 Z. Zhang and C.M. Lieber: Appl. Phys. Lett. **62**, 2792 (1993).
34 C.H. Olk and J.P. Heremans: J. Mat. Res. **9**, 259 (1994).
35 J.P. Issi, L. Langer, J. Heremans, and C.H. Olk: Carbon **33**, 941 (1995).
36 K. Tanaka, T. Sato, T. Yamabe, K. Okahara, K. Uchida, M.Yumura, H. Niino, S. Ohshima, Y. Kuriki, K. Yase, and F. Ikazaki: Chem. Phys. Lett. **223**, 65 (1994).
37 M. Kosaka, T.W. Ebbesen, H. Hiura, and K. Tanigaki: Chem. Phys. Lett. **225**, 161 (1994).
38 L. Langer, L. Stockman, J.P. Heremans, V. Bayot, C.H. Olk, C.V. Haesendonck, Y. Bruynseraede, and J.p. Issi: J. Mat. Res. **9**, 927 (1994).
39 S.N. Song, X.K. Wang, R.P.H. Chang, and J.B. Ketterson: Phys. Rev. Lett. **72**, 697 (1994).
40 Z. Wang, M. Luo, D. Yan, H. Ying, and W. Li: Phys. Rev. B **51**, 13833 (1995).
41 L. Langer, V. Bayot, E. Grivei, J.p. Issi, J.P. Heremans, C.H. Olk, L. Stockman, C.V. Haesendonck, and Y. Bruynseraede: Phys. Rev. Lett. submitted.
42 H. Ajiki and T. Ando: J. Phys. Soc. Jpn. **62**, 1255 (1993).
43 H. Ajiki and T. Ando: J. Phys. Soc. Jpn. **65**, 505 (1996).
44 G.S. Painter and D.E. Ellis: Phys. Rev. B **1**, 4747 (1970).
45 J.C. Slonczewski and P.R. Weiss: Phys. Rev. **109**, 272 (1958).
46 J.M. Luttinger and W. Kohn: Phys. Rev. **97**, 869 (1955).
47 R. Saito, G. Dresselhaus, and M.S. Dresselhaus: Phys. Rev. B **50**, 14698 (1994).
48 There seem to be errors in numerical calculations in ref. 47 (R. Saito: private communication).
49 J.M. Luttinger: Phys. Rev. **102**, 1030 (1956).
50 H. Yorikawa and S.Muramatsu: Phys. Rev. B **50**, 12203 (1994).
51 H. Yorikawa and S.Muramatsu: Phys. Rev. B **52**, 2723 (1995).
52 H. Ajiki and T. Ando: Physica B **201**, 349 (1994).
53 H. Ajiki and T. Ando: it Proc. 22nd Int. Conf. on the Physics of Semiconductours, 1994 (World Scientific, Singapore, 1995) Vol.3, p2061.
54 H. Ajiki and T. Ando: Jpn.J.Appl.Phys.Suppl. **34**, 107 (1995).
55 W.P. Su, J.R. Schrieffer, and A.J. Heeger: Phys. Rev. B **22**, 2099 (1980).
56 A.J. Heeger, S. Kivelson, J.R. Schrieffer, and W.P. Su: Rev. Mod. Phys. **60**, 781 (1988).
57 K. Harigaya: Phys. Rev. B **45**, 12071 (1992).
58 K. Harigaya and M. Fujita: Phys. Rev. B **47**, 16563 (1993).
59 N.A. Viet, H. Ajiki, and T. Ando: J. Phys. Soc. Jpn. **63**, 3036 (1994).
60 H. Ajiki and T. Ando: J. Phys. Soc. Jpn. **64**, 260 (1995).
61 H. Ajiki and T. Ando: to be accepted in Physica B.
62 K. Harigaya: J. Phys. Soc. Jpn. **60**, 4001 (1991).
63 H. Ajiki and T. Ando: J. Phys. Soc. Jpn. **62**, 2470 (1993).
64 H. Ajiki and T. Ando: J. Phys. Soc. Jpn. **63**, 4267 (1994).
65 H. Ajiki and T. Ando: J. Phys. Soc. Jpn. **64**, 4382 (1995).

66 H. Ajiki and T. Ando: Physica B **216**, 358 (1996).
67 L.P. Levy, G. Dolan, J. Dunsmuir, and H. Bouchiat: Phys. Rev. Lett. **64**, 2074 (1990).
68 V. Chandrasekhar, R.A. Webb, M.J. Braddy, M.B. Ketchen, W.J. Gallagher, and A. Kainsasser: Phys. Rev. Lett. **67**, 3578 (1991).
69 M. Büttiker, Y. Imry, and R. Landauer: Phys. Lett. **96A**, 365 (1983).
70 H.-F. Cheung and E.K. Riedel: Phys. Rev. B **40**, 9498 (1989).
71 J.W. McClure: Phys. Rev. **104**, 666 (1956).
72 R.P. Haering and P.R. Wallace: J. Phys. Chem. Solids. **3**, 253 (1957).
73 J.W. McClure: Phys. Rev. **119**, 606 (1960).
74 N. Ganguli and K.S. Krishnan: Proc. Roy. Soc. (London) **A177**, 168 (1941).
75 The calculated susceptibility for a parallel magnetic field given in ref. 63 was about $10^{-3}$ smaller than correct one because of an error in numerical calculation and the perpendicular susceptibility was also incorrect by factor of two. See ref. 64.
76 J.P. Lu: Phys. Rev. Lett. **74**, 1123 (1995).
77 J. Heremans, C.H. Olk, and D.T. Morelli: Phys. Rev. B **49**, 15122 (1994).
78 M.Yumura: in preparation for publication.
79 A.P. Ramirez, R.C. Haddon, O. Zhou, R.M. Fleming, J. Zhang, S.M. McClure, and R.E. Smalley: Science **265**, 84 (1994).
80 X.K. Wang, R.P.H. Chang, A. Patashinski, and J.B. Ketterson: J. Mater. Res. **9**, 1578 (1994).
81 R.A. Jishi, L. Venkataraman, and G. Dresselhaus: Chem. Phys. Lett. **209**, 77 (1993).